5th International Natural Science, Engineering and Material Technologies Conference
Sep 18-20, 2025, İğneada-Kırklareli / TÜRKİYE

ISBN: 978-605-68918-2-3

NEM 2025

FULL TEXT BOOK

5 th International Natural Science, Engineering and Material Technologies Conference

Sep 18-20, 2025 – İğneada-Kırklareli/ TÜRKİYE

FOREWORD

It is a pleasure for us to offer you this Book of Abstract for the 5 th International Natural Science, Engineering and Material Technologies Conference (NEM 2025). Our goal was to create a platform that introduces the newest results on internationally recognized experts to local students and colleagues and simultaneously displays relevant Turkish achievements to the world. The positive feedback of the community encouraged us to proceed and transform a single event into a conference series. Now, NEM 2025 is honored by the presence of over 65 colleagues from various countries. We stayed true to the original NEM 2025 concept and accepted contributions from all fields of materials science and technology to promote multidisciplinary discussions. The focal points of the conference emerged spontaneously from the submitted abstracts: energy applications, advanced materials, electronic and optoelectronic devices, organic electronic materials, chemistry, physics, environmental science, medical science, applied and engineering science, computer simulation of organic structures, biomedical applications and advanced characterization techniques of nanostructured materials. Further fields of interest include e.g. new advanced and functional materials, advanced-functional composites, biomaterials, smart materials, dielectric materials, optical materials, magnetic materials, organic semiconductors, inorganic semiconductors, electronic materials, graphene, and more.

Therefore, we hope that getting first-hand access to so many new results, establishing new connections and enjoying the İğneada-Kırklareli/ TÜRKİYE ambience will make you feel that your resources were spent well in NEM 2025.

Our warmest thanks go to all invited speakers, authors, and contributors of NEM 2025 for accepting our invitation, visiting Kırklareli and using NEM 2025 as a medium for communicating your research results.

We hope that you will enjoy the conference and look forward to meeting you again in one of the forthcoming **NEM 2026** event.

Best regards,
Chairmen's of Conference

Assoc. Prof. Burhan COŞKUN **Prof. Dr. Serpil AKÖZCAN PEHLİVANOĞLU**

Editors:

Assoc. Prof. Burhan COŞKUN

Prof. Dr. Serpil AKÖZCAN PEHLİVANOĞLU

Published, September-2025

This work is subject to copyright. All rights are reserved, whether the whole or part of the material is concerned. Nothing from this publication may be translated, reproduced, stored in a computerized system or published in any form or in any manner, including, but not limited to electronic, mechanical, reprographic or photographic, without prior written permission from the publisher.

nem2025.klu.edu.tr

nem@klu.edu.tr

The individual contributions in this publication and any liabilities arising from them remain the responsibility of the authors.

The publisher is not responsible for possible damages, which could be a result of content derived from this publication.

COMMITTEE

HONORARY PRESIDENT

Prof. Dr. Rengin AK (Rector of Kırklareli University)

CONFERENCE PRESIDENT

Prof. Dr. Serpil AKÖZCAN PEHLİVANOĞLU (Kırklareli University)

Assoc. Prof. Dr. Burhan COŞKUN (Kırklareli University)

ORGANIZING COMMITTEE

Prof. Dr. İlke TAŞÇIOĞLU / İstanbul Topkapı University

Prof. Dr. Ömer Suat TAŞKIN / İstanbul University

Prof. Dr. Sermet KOYUNCU / Çanakkale Onsekiz Mart University

Assoc. Prof. Dr. Ayşegül DERE / Fırat University

Assoc. Prof. Dr. Berna Akgenç HANEDAR / Kırklareli University

Assoc. Prof. Dr. Hale KARAYER / Kırklareli University

Assoc. Prof. Dr. Mehmet Mümin KOÇ / Kırklareli University

Assoc. Prof. Dr. Mustafa KURBAN / Ankara University

Assoc. Prof. Dr. Özge Kılıçoğlu MEHMETCİK / Marmara University

Assoc. Prof. Dr. Selin ÖZDEN / Kırklareli University

Assoc. Prof. Dr. Taner DAŞTAN / Cumhuriyet University

Dr. Öğr. Üyesi Bahadır BEKÂR / Trakya University

Dr. Öğr. Üyesi Ufuk PAKSU / Kırklareli University

Dr. Çiğdem Ş. GÜÇLÜ / Gazi University

SCIENTIFIC COMMITTEE

Prof. Dr. Abdel Salam Hamdy MAKHLOUF / University of Texas / UNITED STATES

Prof. Dr. Abdullah G. AL-SEHEMI / King Khalid University / SAUDI ARABIA

Prof. Dr. Adem TATAROĞLU / Gazi University / TÜRKİYE

Prof. Dr. Ahmed A. ALGHAMDI / King Abdulaziz University / SAUDI ARABIA

Prof. Dr. Asa H. BARBER / London South Bank University / UNITED KINGDOM

Asst. Prof. Bahadır BEKAR / Trakya University / TÜRKİYE

Assoc. Prof. Dr. Bayram ÇETİN / Kırklareli University / TÜRKİYE

Dr. Instructor Burhan CEYLAN / Harran University / TÜRKIYE

Prof. Dr. Burç MISIRLIOĞLU / Sabancı University / TÜRKİYE

Prof. Dr. Chung GWIY-SANG / Ulsan University / KOREA

Dr. Instructor Demet TOPAL KOÇ / Kırklareli University / TÜRKİYE

Prof. Dr. Denis NIKA / Moldova University / MOLDOVA

Asst. Prof. Dr. Devrim ÖZDAL / European University of Lefke, NORTH CYPRUS

Prof. Dr. Dilek NARTOP / Düzce University / TÜRKİYE

Prof. Dr. Elias STATHATOS / Tecnological-Educational Institute of Patras / GREECE

Prof. Dr. Elizabeth BLACKBURN / University of Birmingham / UNITED KINGDOM

Prof. Dr. Hatice ÖĞÜTCÜ / Kirsehir Ahi Evran University/TÜRKIYE

Assoc.Prof. Elvan HASANOĞLU ÖZKAN / Gazi University / TÜRKİYE

Asst. Prof. Erdinç KESKİN / Kırklareli University / TÜRKİYE

Asst. Prof. İsmail KILIÇ / Kırklareli University / TÜRKİYE

Asst. Prof. Macide CANTÜRK RODOP / Yıldız Technical University / TÜRKİYE

Prof. Dr. Müjdat ÇAĞLAR / Eskişehir Anadolu University / TÜRKİYE

Prof. Dr. Mustafa ERKOVAN / Beykoz University / TÜRKİYE

Assoc. Prof. Mustafa KURBAN / Ahi Evran Gazi University / TÜRKİYE

Assoc. Prof. Naim ASLAN / Munzur University / TÜRKİYE

Prof. Dr. Niyazi ÖZDEMİR / Fırat University / TÜRKİYE

Prof. Dr. Numan AKDOĞAN / Gebze Technical University / TÜRKİYE

Assoc. Prof. Dr. Nur P. AYDINLIK / Cyprus International University, NORTH CYPRUS

Prof. Dr. Ömer Suat TAŞKIN / Istanbul University / TÜRKİYE

Assoc. Prof. Özge Kılıçoğlu MEHMETCİK / Marmara University / TÜRKİYE

Prof. Dr. Ram K. GUPTA / Pittsburg State University / UNITED STATES

Prof. Dr. Raşit TURAN / Middle East Technical University / TÜRKİYE

Prof. Dr. S. MANSOURI / University of Gabès / TUNUSIA

Asst. Prof. Sena Esen BAYER KESKİN / Kırklareli University / TÜRKİYE

Prof. Dr. Serap ŞENTÜRK DALGIÇ / Trakya University / TÜRKİYE

Assoc. Prof. Dr. Süleyman AŞIR / Near East University, NORTH CYPRUS

Dr. Şükrü Can Demirtaş / Yıldız Teknik University / TÜRKİYE

Assoc. Prof. Taner DAŞTAN / Cumhuriyet University / TÜRKİYE

Assoc. Prof. Tarık ASAR / Gazi University / TÜRKİYE

Prof. Dr. W. Aslam FAROOQ / King Saud University / SAUDI ARABIA

Prof. Dr. Yasin ÜNLÜTÜRK / Kırklareli University / TÜRKİYE

FULL TEXT PRESENTATIONS

FULL TEXT PRESENTATIONS

NAME	TITLE	PAGE NO
B. BEKAR	EFFECT OF PRESSURE AND TEMPERATURE ON OPTICAL PROPERTIES IN A TRIPLE QUANTUM WELL	1-10
B. BEKAR	INVESTIGATION OF OPTICAL TRANSITIONS IN H-SHAPED QUANTUM WIRE UNDER ELECTRIC AND LASER FIELDS	11-28
F. BAYÇA	REMOVAL OF CATIONIC METHYLENE BLUE DYE FROM WASTEWATER WITH COLEMANITE	39-48
M. BAYRAM	HIDDEN HAZARDS: IMPURITIES IN TEXTILE DYES AND AUXILIARIES, THEIR IMPACT ON HUMAN AND ENVIRONMENTAL HEALTH	59-71
N. TOPÇU	COMPARISON OF POLYESTER RESIN AND SILICONE RESIN IN COMPOSITE STONE PRODUCTION	90-98
N. TUTKUN	IMPROVED ENERGY HARVESTING FOR SOLAR PV SYSTEMS UNDER LOW IRRADDIANCE CONDITIONS	49-58
O. Ü. KORCAN	EXTENDING THE SERVICE LIFE OF RUBBER MOLDS USED IN COMPOSITE STONE PRODUCTION PROCESS	99-102
Ö. AYTAŞ	COMPARING SAFETY: RESPONSES OF LARGE LANGUAGE MODELS TO ADVERSARIAL PROMPTS	72-80
S. BİLEN	EFFECTS of POLYPHENOLS and/or BORON ENRICHED DERIVATIVES on GERMINATION of CORN SEEDS UNDER COLD STRESS	81-89
Ş. Y. KARABULUT	AN ALTERNATIVE NATURAL PRESERVATIVE FOR FOOD INDUSTRY: BEE BREAD	29-38

5th International Natural Science, Engineering and Material Technologies Conference
Sep 18-20, 2025, İğneada-Kırklareli / TÜRKİYE

EFFECT OF PRESSURE AND TEMPERATURE ON OPTICAL PROPERTIES IN A TRIPLE QUANTUM WELL

B. Bekar

[1]*Department of Electricity and Energy, Trakya University, Vocational of Kesan, 22800 Edirne, Turkey*

E-mail: bahadirbekar@trakya.edu.tr

Abstract

In this study, we investigated a one-dimensional AlGaAs/GaAs quantum well (QW) and calculated its eigenvalues and eigenvectors as functions of hydrostatic pressure (P) and temperature (T). The calculations were performed within the effective mass approximation using the finite difference method. The effects of P and T on the total absorption, total refractive index, and second-harmonic generation (SHG) coefficient were obtained and presented as the main results.

Keywords: AlGaAs/GaAs quantum well, hydrostatic pressure, temperature, optical absorption, refractive index, second-harmonic generation

1. INTRODUCTION

GaAs/AlGaAs quantum wells, owing to their well-defined subband structures and high carrier mobilities, serve as model platforms for tunable optoelectronic devices. The control of linear and nonlinear optical responses through well shape and external fields has been extensively investigated. For instance, Ungan et al. theoretically demonstrated that in GaAs-based QWs with Kratzer-type potentials, both linear and nonlinear optical properties vary sensitively with well parameters [1]. The combined effects of hydrostatic pressure (P) and temperature (T) have also been reported for various geometries.

Zhang et al. (Morse QW, with a magnetic field) examined the influence of P–T on third-order optical terms; Tüzemen et al. (asymmetric δ-doped GaAs QW) studied how P–T, together with position-dependent effective mass, affect nonlinear optical (NLO) coefficients. More recently, Chang et al. and Shaer et al. reported in detail how P–T modulates both linear and NLO responses through variations in effective mass ($m*$) and bandgap energy (Eg) [2–4].

In addition, numerous works have shown that external electric and magnetic fields (applied parallel or perpendicular to the layers) strongly modulate changes in absorption and refractive index [5]. From a materials parameterization perspective, the compilation by Vurgaftman–Meyer–Ram-Mohan remains a standard reference for GaAs/AlGaAs. It also reports that the conduction-band offset ratio (Γ-valley) at the GaAs/AlGaAs interface is approximately Qc ≈ 0.60, as determined by direct measurements [6–8].

2. MATERIAL AND METHODS

We considered a one-dimensional quantum well along the z-direction, as illustrated in Figure 1.

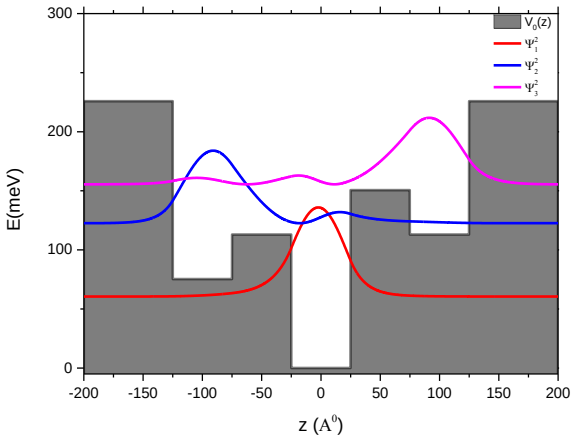

Figure 1. Probability distributions of the ground state and the first and second excited states confined within the quantum well.

The Hamiltonian for an electron is given by

$$H = \frac{P_\perp^2}{2m^*(p,T)} + \frac{P_z^2}{2m^*(p,T)} + V(z,p,T) \quad (1)$$

Here, P denotes the applied hydrostatic pressure (in kbar), and T is the applied temperature (in Kelvin). The term $\frac{P_\perp^2}{2m^*(p,T)}$ represents the kinetic energy operator in the xy-plane, while $V(z,P,T)$ corresponds to the quantum well potential. The parameter $m*$ denotes the effective mass of the electron.

$$m^* = \frac{m_0}{1+7.51\left[\left(\frac{2}{E_g^\Gamma(p,T)}\right)+\left(\frac{1}{E_g^\Gamma(p,T)+0.341}\right)\right]} \quad (2)$$

is expressed as [9–11]. Here, m_0 is the free electron mass, and $E_g^\Gamma(p,T)$ denotes the Γ-point band gap of GaAs as a function of pressure and temperature.

$$E_g^\Gamma(p,T)=E_g^\Gamma(0,T) + \mathrm{bp} + \mathrm{cp2} \quad (3)$$

Here, $E_g^\Gamma = [1.519 - (5.405 \times 10^{-4}T^2)/(T+204)]$eV, with $b = 1.26 \times 10^{-2}$ eV/kbar, $c = -3.77 \times 10^{-5}$ eV/kbar^2 [9-11].

The quantum well potential is given by, $V_0 = Q_c\left[\Delta E_g^\Gamma(x) + pD(x) + G(x)T\right]$ where x=0.3x = 0.3x=0.3 is the molar fraction of aluminum in $Al_xGa_{1-x}As$ Here, the conduction-band offset ratio is taken as Qc=0.6. The bandgap difference is expressed as. $\Delta E_g^\Gamma(x) = (1.155x + 0.37x^2)eV$, with the pressure- and temperature-dependent terms $D(x) = [(-1.3 \times 10^{-3})x]$ eV/kbar, $G(x) = [(-1.15 \times 10^{-4})x]$ eV/K .

Since the static dielectric constant varies with hydrostatic pressure and temperature in both the barrier and well regions, it is taken as [9-11]

$$\varepsilon(p,T) = \begin{cases} 12.74exp[-1.67 \times 10^{-3}p]exp[9.4 \times 10^{-5}(T-75.6)], T \le 200K \\ 13.18exp[-1.73 \times 10^{-3}p]exp[20.4 \times 10^{-5}(T-300)], T > 200K \end{cases} \quad (4)$$

The quantum well width as a function of hydrostatic pressure given by

$$L_w(p) = L_w[1 - (S_{11} + 2S_{12})p] \quad (5)$$

Here, L_w denotes the well width at zero pressure [9–11]. S_{11} and S_{12} are the elasticity constants for GaAs, with values of 1.16×10^{-3}kbar^{-1} and -3.7×10^{-4}kbar, respectively [9–11]. Under this choice, V_0 decreases with increasing pressure, and the finite-well effect suppresses geometric confinement, resulting in a net reduction of the eigenenergies.

$$\beta_1(\omega)= \frac{\sigma}{c\varepsilon_0 n_s}\frac{\hbar\omega|M_{if}|^2/\tau_{in}}{(E_{if}-\hbar\omega)^2+(\hbar/\tau_{in})^2} \tag{6}$$

$$\beta_3(\omega) = -\frac{2\sigma}{(c\varepsilon_0 n_s)^2}\frac{\frac{\hbar\omega I|M_{if}|^4}{\tau_{in}}}{[(E_{if}-\hbar\omega)^2+\left(\frac{\hbar}{\tau_{in}}\right)^2]^2}\cdot\left[1-\left|\frac{M_{ff}-M_{ii}}{2M_{if}}\right|^2\frac{(E_{if}-\hbar\omega)^2-\left(\frac{\hbar}{\tau_{in}}\right)^2+2E_{if}(E_{if}-\hbar\omega)}{E_{if}^2+\left(\frac{\hbar}{\tau_{in}}\right)^2}\right] \tag{7}$$

Total absorption coefficient β_t (ħω,I) given by

$$\beta_t(\omega,I) = \beta_1(\hbar\omega)+\beta_3(\hbar\omega,I) \tag{8}$$

[12]. The first-order and third-order linear and nonlinear refractive indices are given as follows:

$$\frac{\Delta n_1(\omega)}{n_s} = \frac{\sigma}{2\varepsilon_0 n_s^2}\frac{|M_{if}|^2(E_{if}-\hbar\omega)}{(E_{if}-\hbar\omega)^2+(\hbar/\tau_{in})^2} \tag{9}$$

$$\frac{\Delta n_3(\omega,I)}{n_s} = -\frac{\sigma}{c\varepsilon_0^2 n_s^3}\frac{I|M_{if}|^4(E_{if}-\hbar\omega)}{[(E_{if}-\hbar\omega)^2+(\hbar/\tau_{in})^2]^2}\cdot\left\{1-\left|\frac{M_{ff}-M_{ii}}{2M_{if}}\right|^2\frac{E_{if}(E_{if}-\hbar\omega)^2-\left(\frac{\hbar}{\tau_{in}}\right)^2(3E_{if}-2\hbar\omega)}{\left[E_{if}^2+\left(\frac{\hbar}{\tau_{in}}\right)^2\right](E_{if}-\hbar\omega)}\right\} \tag{10}$$

Total refractive index

$$\frac{\Delta n_t(\hbar\omega,I)}{n_s} = \frac{\Delta n_1(\hbar\omega)}{n_s}+\frac{\Delta n_3(\hbar\omega,I)}{n_s} \tag{11}$$

The second-harmonic generation (SHG) is expressed as follows:

$$\chi_{2w}^{(2)} = \frac{e^3\sigma}{\varepsilon_0\hbar^2}\frac{M_{12}M_{21}(M_{11}-M_{22})}{(w-w_{21}-i\Gamma_{12})(2w-w_{21}-i\Gamma_{12})} \tag{12}$$

[9-11]. $w_{ij} = (E_i - E_f)/\hbar$ corresponds to the transition frequency, where E_f and Ei enote the final and initial energy states, respectively. E_{if}, he energy difference between these two levels is defined as

$$E_{if} = E_f - E_i \tag{13}$$

M_{if} and the dipole matrix element is calculated as

$$M_{if} = |< \psi_i | e.x | \psi_f >| \tag{14}$$

3. RESULTS AND DISCUSSION

In our calculations, m_0 is the free electron mass, the electron charge is $e = 1.602 \times 10^{-19} C$, the carrier concentration in the material is taken as σ =3×10^{22} m^{-3}, the intraband relaxation time is τ_{in} =0.14ps and the refractive index is defined as n_s =$\sqrt{\varepsilon}$ 'dir. The optical intensity of the incident light is assumed to be I =0.1MW/cm$^{2.}$

Figure 1. In addition to showing how the QW potential varies along the z-axis, the figure illustrates the probability distributions of the ground, first, and second excited states. The ground state is localized at the center of the well, while the first and second excited states are localized in the left and right wells, respectively.

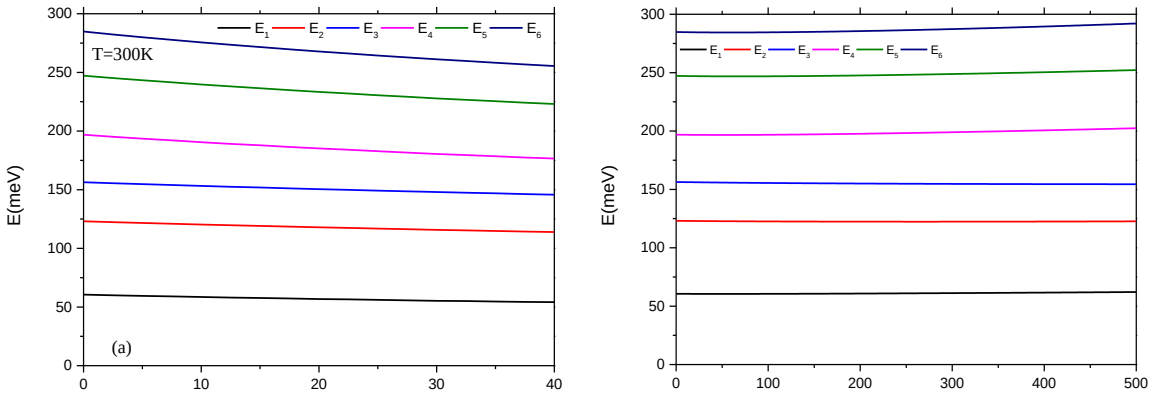

Figure 2. Variation of the energy eigenvalues of the ground and excited states as a function of (a) hydrostatic pressure and (b) temperature.

In Figure 2(a), it is observed that when hydrostatic pressure is applied to the system, all energy levels decrease with increasing pressure. In Figure 2(b), however, when temperature is applied, the energies of the ground and higher states decrease, while the first and second excited states exhibit an increase. This behavior

may be attributed to the fact that, in triple quantum wells, the wavefunctions are localized at different regions within the structure.

Table 1. Variations of the quantum well barrier potential (V_0), band gap energy (ΔE_g^{Γ}), effective mass (m*) and dielectric constant (ε) as functions of hydrostatic pressure and temperature.

	T=0, P=0	T=100K, P=0	T=300K, P=0	T=500K, P=0	T=0, P=10kbar	T=0, P=20kbar	T=0, P=30kbar
V_0(meV)	227.8	225.8	221.67	217.53	225.54	223.2	220.86
ΔE_g^{Γ} (meV)	379.8	376.3	369.4	362.5	375.9	372.0	368.1
m*(m_0)	0.067	0.0663	0.0632	0.0595	0.0717	0.0761	0.0802
$\varepsilon(\varepsilon_0)$	12.64	12.76	13.18	13.72	12.43	12.21	12.01

When the temperature is increased under constant pressure, the quantum well barrier potential (V_0), the band gap energy (ΔE_g^{Γ}) and the effective mass (m* decrease, while the dielectric constant ($\boldsymbol{\varepsilon}$) increases. Conversely, when the temperature is kept constant and the pressure is increased, (V_0), (ΔE_g^{Γ}) and ($\boldsymbol{\varepsilon}$) decrease, whereas (m*) increases.

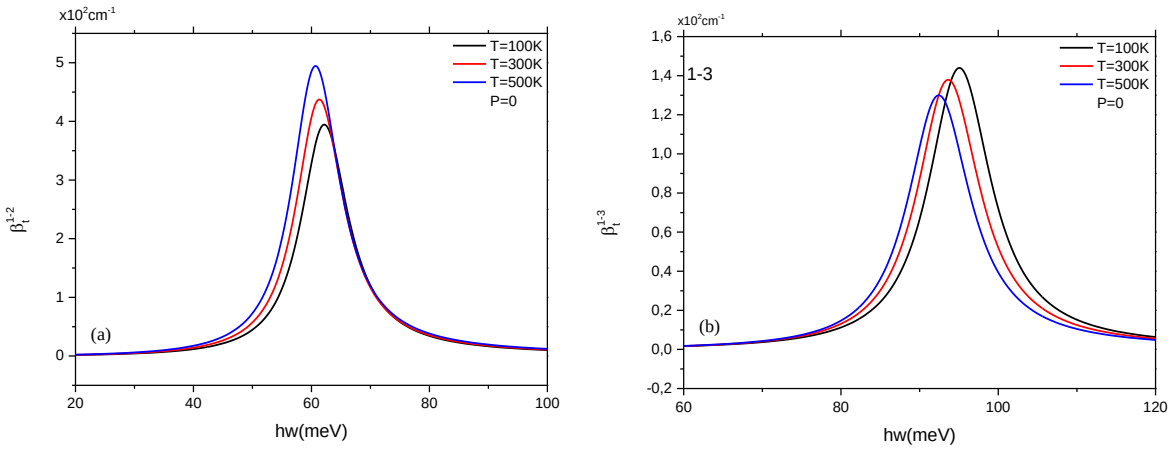

Figure 3. (a) Total absorption coefficient for the 1–2 transitions at different temperatures; (b) total absorption coefficient for the 1–3 transitions at different temperatures.

In Figure 3(a), the variation of the total absorption coefficient with temperature is shown. As the temperature increases, the peak value of the absorption coefficient increases and exhibits a red shift. In Figure 3(b), for the 1–3 transition, a similar red-shift tendency with increasing temperature is observed; however, the overall absorption coefficients decrease.

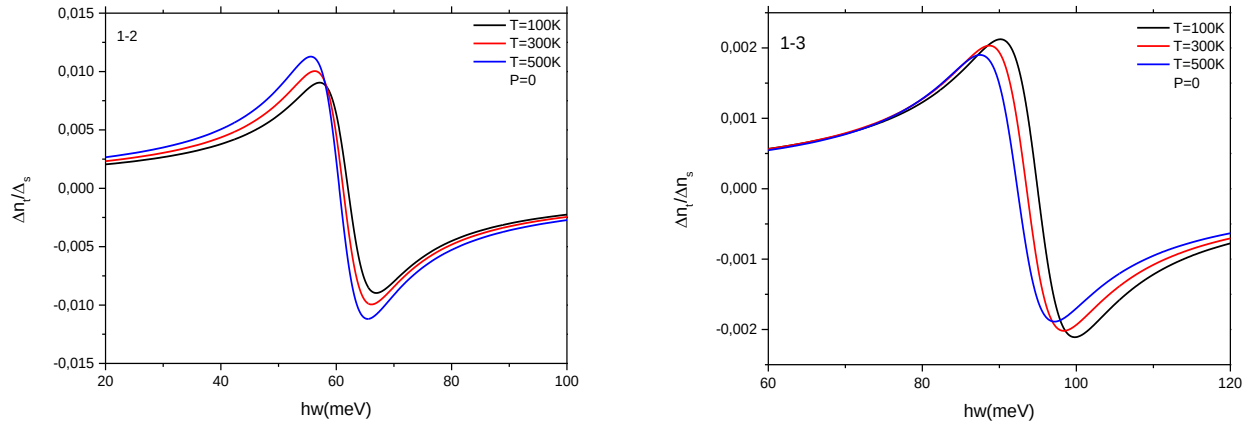

Figure 4. (a) Variation of the total refractive index for the 1–2 transition as a function of different temperatures; (b) variation of the total refractive index for the 1–3 transition as a function of different temperatures.

In Figure 4(a), the total refractive index exhibits a red shift with increasing temperature, and the magnitude of the refractive index also increases. In Figure 4(b), however, for the 1–3 transition, the refractive index decreases as the temperature rises. The refractive index peak appears at a photon energy of approximately 60 meV for the 1–2 transition, whereas it occurs at around 95 meV for the 1–3 transition.

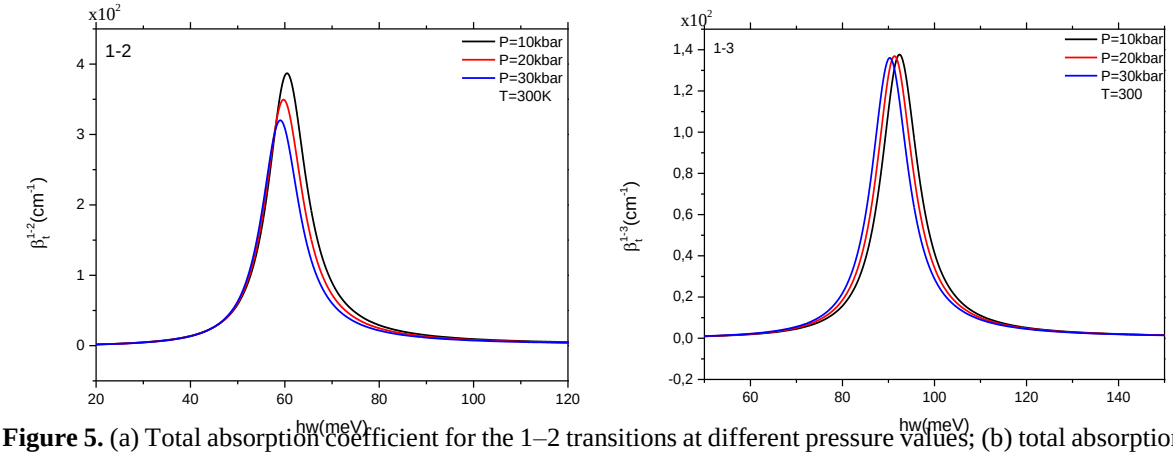

Figure 5. (a) Total absorption coefficient for the 1–2 transitions at different pressure values; (b) total absorption coefficient for the 1–3 transitions at different pressure values.

In Figure 5(a), the effect of different pressures on the quantum well is illustrated. As the pressure increases, the total absorption coefficients corresponding to the 1–2 transitions decrease and exhibit a red shift. In Figure 5(b), however, while the amplitudes show no significant decrease with increasing pressure, a slight red shift can still be observed.

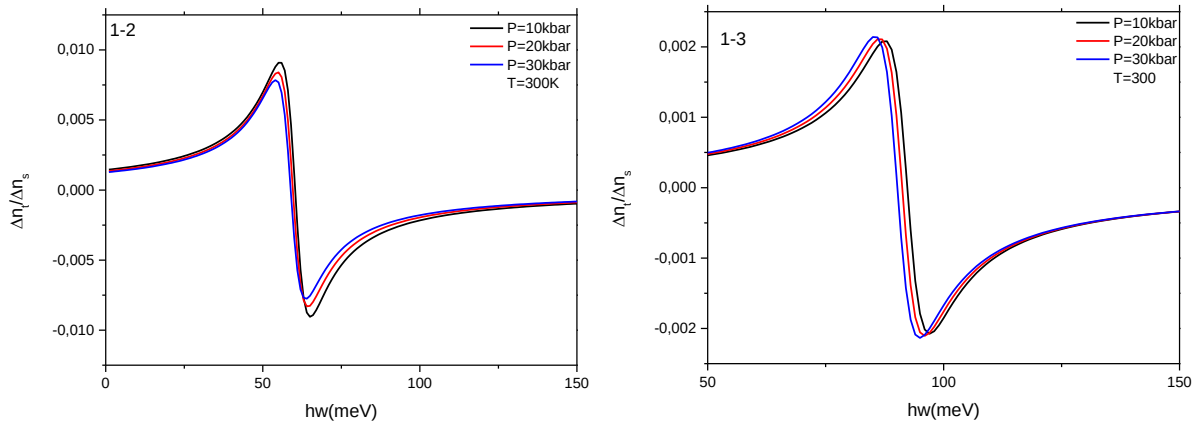

Figure 6. (a) Variation of the total refractive index for the 1–2 transition as a function of different pressure values; (b) variation of the total refractive index for the 1–3 transition as a function of different pressure values.

In Figure 6(a), the total refractive index shows a decreasing trend with increasing pressure, accompanied by a slight reduction in photon energy. In Figure 6(b), a small increase in the total refractive index is observed, while the photon energy decreases.

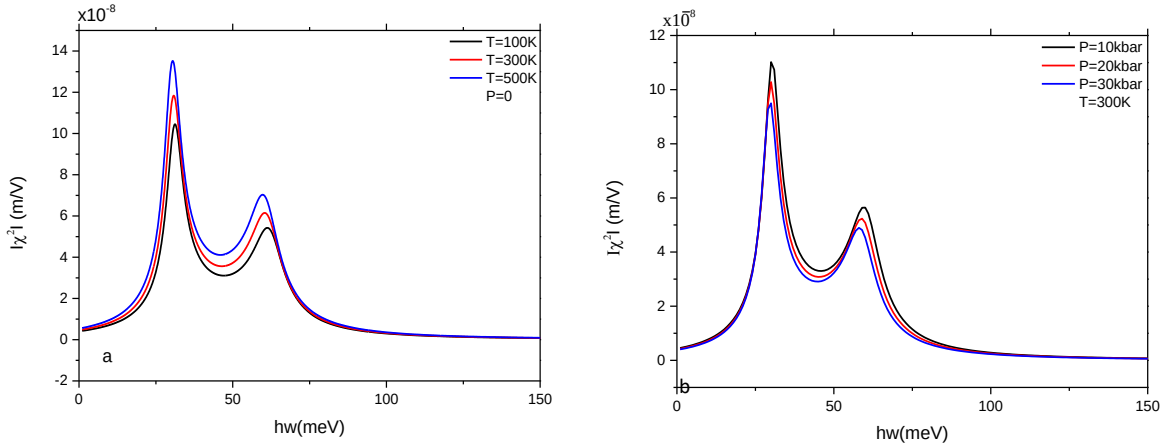

Figure 7. (a) Variation of the SHG coefficient with different temperatures; (b) variation of the SHG coefficient with different pressure values.

In Figure 7, it is observed that the SHG coefficient increases in amplitude and exhibits a blue shift with rising temperature, whereas with increasing pressure the amplitudes decrease and a red-shift tendency is observed.

3. CONCLUSION

In this work, we investigated the effects of hydrostatic pressure and temperature on the optical properties of GaAs/AlGaAs quantum wells within the effective mass approximation using the finite difference method. Since the quantum structure parameters—such as the effective mass (m^*), the band gap energy (ΔE_g^{Γ}), the barrier potential (V_0), and the dielectric constant (ε)—are strongly dependent on both temperature and pressure, variations in these external factors induce significant changes in these parameters. As a result, notable modifications were observed in the system's energy eigenvalues, total absorption, total refractive index, and second-harmonic generation (SHG) response.

The findings indicate that increasing temperature generally leads to a red shift in the optical spectra, accompanied by enhanced absorption and refractive index for certain transitions, while hydrostatic pressure causes a reduction in absorption amplitudes and refractive index, along with red-shift tendencies in transition energies. Furthermore, the SHG coefficient exhibits an enhancement and blue shift with increasing temperature, whereas pressure suppresses its amplitude and induces a red shift.

Overall, the results demonstrate that the interplay between pressure and temperature can be effectively employed to tailor the optical responses of GaAs/AlGaAs quantum wells. This tunability opens pathways for the design and optimization of advanced optoelectronic and nonlinear optical devices operating under variable external conditions.

REFERENCES

[1] Ungan, F., The nonlinear optical properties of GaAs-based quantum wells with Kratzer-type potential, *Opt. Laser Technol.*, 116, 198–205, 2019. https://doi.org/10.1016/j.optlastec.2019.03.021

[2] Zhang, Z.-H., Li, S.-S., Peeters, F. M., Xu, W., Combined influence of hydrostatic pressure and temperature on the optical properties of Morse quantum wells, *Materials*, 11, 668, 2018. https://doi.org/10.3390/ma11050668

[3] Tüzemen, A. T., Dakhlaoui, H., Ungan, F., Effects of hydrostatic pressure, temperature, and position-dependent mass on the nonlinear optical properties of asymmetric δ-doped GaAs quantum wells, *Eur. Phys. J. Plus*, 139, 690, 2024. https://doi.org/10.1140/epjp/s13360-024-05490-8

[4] Chang, C., Li, J., Wu, Y., Tunability of the nonlinear optical absorption in a GaAs quantum well under pressure and temperature dependent effective mass, *Opt. Laser Technol.*, 174, 110982, 2024. https://doi.org/10.1016/j.optlastec.2024.110982

[5] Shaer, A., Al-Saidi, H., Mezher, R., Hydrostatic pressure and temperature dependent optical properties of GaAs quantum wells under magnetic field, *Opt. Laser Technol.*, 176, 111034, 2024. https://doi.org/10.1016/j.optlastec.2024.111034

[6] Vurgaftman, I., Meyer, J. R., Ram-Mohan, L. R., Band parameters for III–V compound semiconductors and their alloys, *J. Appl. Phys.*, 89, 5815–5875, 2001. https://doi.org/10.1063/1.1368156

[7] Yi, W., Yang, W., Xu, W., Bandgap and band offsets determination in GaAs/AlGaAs quantum wells, *arXiv preprint*, arXiv:0904.2364, 2009. https://arxiv.org/abs/0904.2364

[8] Cheong, H. M., McCluskey, M. D., Haller, E. E., Becla, P., Hydrostatic-pressure coefficient of the direct band gap in GaAs, *Phys. Rev. B*, 53, 10916–10919, 1996. https://doi.org/10.1103/PhysRevB.53.10916

[9] Tüzemen, A. T., Dakhlaoui, H., Ungan, F., Effects of hydrostatic pressure and temperature on the nonlinear optical properties of GaAs/GaAlAs zigzag quantum well, *Philos. Mag.*, 102, 2428–2443, 2022. https://doi.org/10.1080/14786435.2022.2111028

[10] Ehrenreich, H., Band structure and transport properties of some III–V compounds, *J. Appl. Phys.*, 32, 2155–2166, 1961. https://doi.org/10.1063/1.1728416

[11] Durmuslar, A. S., Dakhlaoui, H., Al, E. B., et al., Influence of hydrostatic pressure and temperature on the optical responses of asymmetric triple quantum wells, *Eur. Phys. J. Plus*, 139, 3, 2024. https://doi.org/10.1140/epjp/s13360-023-04782-9

[12] Bekar, B., Boz, F. K., Aktas, S., Okan, S. E., The effect on the optical absorption coefficients due to the positions in the plane of square GaAs/Al(GaAs) quantum well wire under the laser field, *Acta Phys. Pol. A*, 136(6), 2019. https://doi.org/10.12693/APhysPolA.136.971

5th International Natural Science, Engineering and Material Technologies Conference
Sep 18-20, 2025, İğneada-Kırklareli / TÜRKİYE

INVESTIGATION OF OPTICAL TRANSITIONS IN H-SHAPED QUANTUM WIRE UNDER ELECTRIC AND LASER FIELDS

B. Bekar

[1]Keşan Vocational School, Trakya University, Keşan, Edirne, Turkey

E-mail: bahadirbekar@gmail.com

Abstract

In this study, we investigate an H-shaped AlGaAs/GaAs quantum wire. Within the framework of the effective mass approximation, the Schrödinger equation was solved using the finite difference method to obtain the eigenvalues and eigenvectors of the system. External electric and laser fields were applied along both the x- and y-axes. The effects of the variations in energy eigenvalues on the total absorption and refractive index were analyzed, and the corresponding results are presented.

Keywords: Quantum wire, optic absorpsition, refractive index

1. INTRODUCTION

In recent years, numerous optoelectronic devices have been developed using semiconductor materials [1–4[. Examples include transistors, solar cells, and light-emitting diodes (LEDs) [5–15[. In particular, significant attention has been devoted to optical absorption and optical refraction [16–19[. Alongside the study of first- and third-order optical absorption and refractive indices, second-harmonic generation (SHG) has also emerged as a prominent research topic [20–24].

H. Sarac *et al.* analyzed the variations in both linear and nonlinear optical properties of a one-dimensional GaAs/GaAlAs quantum well with a modified Lennard–Jones potential. By employing the diagonalization method, the effective mass approximation, and the parabolic band model, they solved the Schrödinger equation to determine subband energy levels and wave functions. Their results demonstrated that changes in external fields and structural parameters strongly affect the total optical absorption coefficients and the relative refractive index changes. Moreover, they showed that the optical response undergoes a redshift with increasing electric, magnetic, and intense laser fields as well as quantum well width, while it exhibits a blueshift with increasing well depth [25].

Altun investigated the electron probability distributions, energy levels, nonlinear optical rectification (NOR), and second-harmonic generation (SHG) coefficients of double-square, double-triangular, and double-parabolic quantum wells as functions of variable well width under the influence of electric and magnetic fields. It was found that the application of such fields induces both redshifts and blueshifts in the optical spectra across all quantum well structures. Furthermore, the NOR and SHG coefficients were shown to be widely tunable over a broad energy range for all well geometries. These findings suggest that the application of electric and magnetic fields provides an effective means to manipulate the optical and electronic properties of semiconductors, thus offering new opportunities in the design of optoelectronic devices [26].

M. G. Barseghyan *et al.* studied the influence of a laser field on intersubband optical absorption and refractive index changes in a GaAs/AlGaAs quantum wire with an equilateral triangular cross-section. The wire was subjected to a linearly polarized laser beam, assumed to be non-resonant with the semiconductor structure and perpendicular to one side of the triangular cross-section. The linear, nonlinear, and total absorption coefficients, as well as the refractive index changes, were calculated as functions of the laser field for the allowed intersubband transitions [27].

In this work, we consider an H-shaped quantum wire. By solving the time-independent Schrödinger equation within the effective mass approximation using the finite difference method, we determined the

eigenvalues and eigenfunctions of the system. While most studies focus primarily on the 1–2 and 1–3 transitions, here we include all possible transitions among the first ten energy levels, thereby analyzing the total absorption and refractive index changes under the influence of external electric and laser fields.

2. MATERIAL AND METHODS

Using AlGaAs/GaAs semiconductor materials, we constructed an H-shaped quantum wire (HQW). For this structure, the potential profile was defined as illustrated in the following figure.

The time-dependent Schrödinger equation for the HQW in the *xy*-plane can be written as

$$\frac{1}{2m^*}[p_\perp + eA(t)]^2 + V(x,y) + |e|.F.x\,\}\,\psi(x,y,t) = i\hbar\frac{\partial}{\partial t}\psi(x,y,t) \qquad (1)$$

Here, $p_\perp$ denotes the momentum of an electron in the plane, m^* is the effective mass of the electron, e is the electron charge in the absence of a laser field, and F is the electric field strength. The laser vector potential is given as $A(t) = \hat{x}A_0\cos(wt)$, where $\hat{x}$ is the unit vector along the *x*-axis. To eliminate the time dependence, the Kramers–Henneberger transformation $x \rightarrow x+\alpha_0\sin(wt)$ is applied, and the equation can be rewritten accordingly [27]

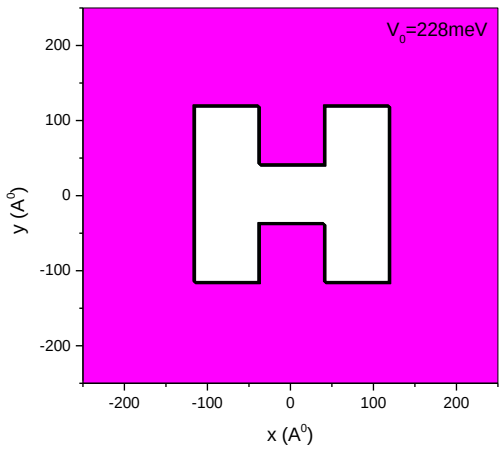

Figure 1. Potential profile of the H-shaped quantum wire

$$\left[-\frac{\hbar^2}{2m^*}\left(\frac{\partial^2}{\partial x^2}+\frac{\partial^2}{\partial y^2}\right) + \widetilde{V_{dr}}(x,y) + |e|.F.x\right]\tilde{\psi}(x,y) = E\tilde{\psi}(x,y) \qquad (2)$$

Here, $\tilde{V}_{dr}$ is referred to as the laser-dressed potential and is expressed as

$$\tilde{V}_{dr}(x,y) = \frac{w_D}{2\pi}\int_0^{2\pi/w_D} V(x,y,t)\,.\,dt = \frac{1}{2\pi}\int_0^{2\pi} V(x+\alpha_0 sin\theta, y)\,.\,d\theta \quad (3)$$

Here, $\alpha_0 = \frac{e.A_0}{m^*.w_D}$ is the laser-dressing parameter, and $\frac{2\pi}{w_D}$ denotes the period of the laser field. The first-order linear and third-order nonlinear absorption coefficients are given as follows:

$$\beta_1(\omega) = \frac{\sigma}{c\varepsilon_0 n_s}\frac{\hbar\omega|M_{if}|^2/\tau_{in}}{(E_{if}-\hbar\omega)^2+(\hbar/\tau_{in})^2} \quad (4)$$

$$\beta_3(\omega) = -\frac{2\sigma}{(c\varepsilon_0 n_s)^2}\frac{\frac{\hbar\omega I|M_{if}|^4}{\tau_{in}}}{[(E_{if}-\hbar\omega)^2+\left(\frac{\hbar}{\tau_{in}}\right)^2]^2}.\left[1-\left|\frac{M_{ff}-M_{ii}}{2M_{if}}\right|^2\frac{(E_{if}-\hbar\omega)^2-\left(\frac{\hbar}{\tau_{in}}\right)^2+2E_{if}(E_{if}-\hbar\omega)}{E_{if}^2+\left(\frac{\hbar}{\tau_{in}}\right)^2}\right] \quad (5)$$

The total absorption coefficient, β_t (ħω,I), is given by

$$\beta_t(\omega,I) = \beta_1(\hbar\omega) + \beta_3(\hbar\omega,I) \quad (6)$$

The first-order linear and third-order nonlinear refractive indices are given as follows:

$$\frac{\Delta n_1(\omega)}{n_s} = \frac{\sigma}{2\varepsilon_0 n_s^2}\frac{|M_{if}|^2(E_{if}-\hbar\omega)}{(E_{if}-\hbar\omega)^2+(\hbar/\tau_{in})^2} \quad (7)$$

$$\frac{\Delta n_3(\omega,I)}{n_s} = -\frac{\sigma}{c\varepsilon_0^2 n_s^3}\frac{I|M_{if}|^4(E_{if}-\hbar\omega)}{[(E_{if}-\hbar\omega)^2+(\hbar/\tau_{in})^2]^2}.\left\{1-\left|\frac{M_{ff}-M_{ii}}{2M_{if}}\right|^2\frac{E_{if}(E_{if}-\hbar\omega)^2-\left(\frac{\hbar}{\tau_{in}}\right)^2(3E_{if}-2\hbar\omega)}{\left[E_{if}^2+\left(\frac{\hbar}{\tau_{in}}\right)^2\right](E_{if}-\hbar\omega)}\right\} \quad (8)$$

The total refractive index is expressed as

$$\frac{\Delta n_t(\hbar\omega,I)}{n_s} = \frac{\Delta n_1(\hbar\omega)}{n_s} + \frac{\Delta n_3(\hbar\omega,I)}{n_s} \quad (9)$$

Here, E_f and E_i are defined as the final and initial energy states, respectively. E_{if} is defined as the energy difference between these two levels and is calculated using the following expression.

$$E_{if} = E_f - E_i \quad (10)$$

The dipole matrix element, M_{if}, is calculated from the following expression.

$$M_{if} = |<\psi_i|e.x|\psi_f>| \quad (11)$$

Here, ħω is the required photon energy, ε_0 is the permittivity of free space, σ is the carrier density in the system, ns=3.2 is the refractive index of the system, ε is the dielectric constant of the material, c is the speed of light in vacuum, τ_{in} is the relaxation time, and I is the optical intensity of the externally applied light. $\psi_i$and ψ_f denote the initial and final state wave functions, respectively.

3. RESULTS AND DISCUSSION

In the calculations, the aluminum concentration was taken as x=0.3. The dielectric constant of the material was assumed to be $\varepsilon_s=12.58\varepsilon_0$ in the static case and $\varepsilon_\infty=10.9\varepsilon_0$ at high frequencies. Throughout the entire structure, the effective mass was taken as $m^*=0.0665m_0$ and the step potential of AlGaAs was set to V_0=228 meV. The carrier electron density in the system was chosen as $\sigma=3\times10^{22}$ m^{-3}, with an intersubband relaxation time of τ_{in}=5 ps and the refractive index defined as ns=3.2. The optical intensity of the externally applied light was taken to be I=0.06 MW/cm^2.

In Figure 2, an external electric field was applied along the *x*-direction of the HQW structure, ranging from 0 to 100 kV/cm. The variations of the first ten energy states with respect to the electric field strength are presented. It is observed that the energy levels E_1 and E_2 decrease to zero at approximately 55 and 85 kV/cm, respectively. While the ground-state energy E_1 exhibits a direct monotonic behavior, the E_2 level first increases up to around 25 kV/cm and then decreases after crossing with E_3. The energy levels E_3 and E_4 are seen to separate from each other as the electric field strength increases. For the other states, although anticrossing points appear at certain field strengths, the overall trend of the energy levels exhibits a decreasing characteristic with increasing electric field strength.

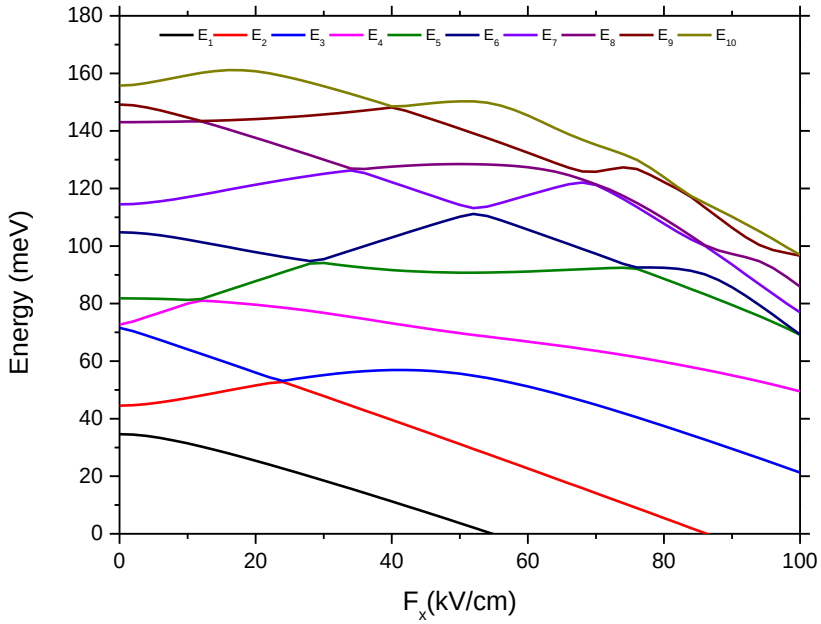

Figure 2. Variation of energy states as a function of the applied electric field along the *x*-direction.

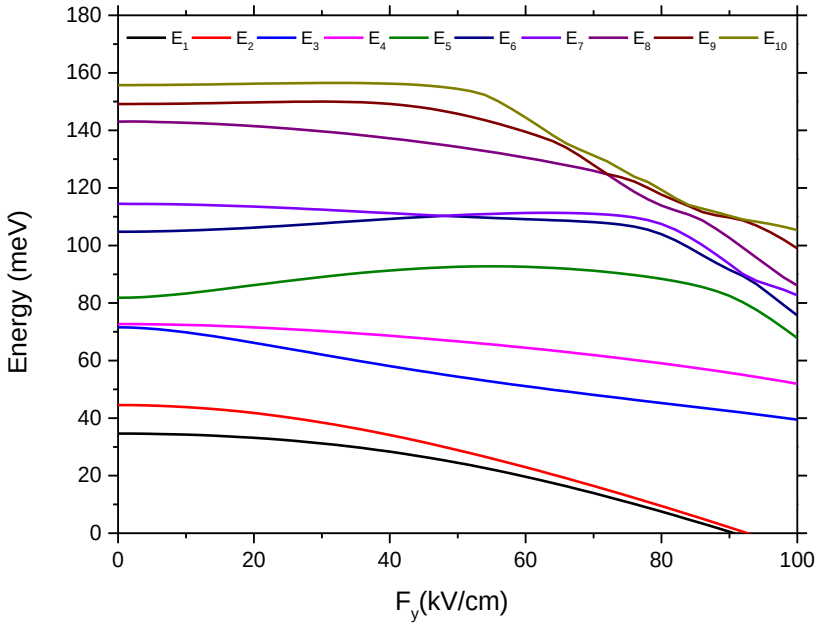

Figure 3. Variation of energy states as a function of the applied electric field along the *y*-direction

In Figure 3, the electric field was applied along the *y*-direction, and the dependence of the first ten energy levels on the field strength was analyzed. In contrast to Figure 2, no anticrossing points were observed.

Unlike the behavior in Figure 2, the first two energy levels, E_1 and E_2 both decrease with increasing field strength and eventually reach zero at higher field values, converging to nearly the same energy. The remaining energy levels generally exhibit a decreasing trend as the electric field increases, except for E_5 and E_6, which initially increase with the field strength before showing a decline beyond a certain point.

Allowed transitions	Photon peak energy ≈ (meV)	Absorption coefficient (x10^{2}cm^{-1})
9-10	9	3,78
7-8	29	11.63
6-7	11	5.36
5-8	62	14,73
5-7	32	0,12
5-6	23	8,18
4-10	85	0,23
4-9	79	1,53
3-9	81	0,92
3-4	7	0,58
2-7	71	4.68
2-5	39	12,98
1-8	113	3.95
1-2	12	5.47

Table 1. Absorption coefficients under *x*-polarization (absorption coefficients below 0.1×10^2 cm^{-1} were neglected)

In Figure 4, the total absorption and the third-order nonlinear optical absorption are shown for *x*-polarized excitation. We computed all allowed transitions among the first ten energy levels. These levels are strictly below the well barrier height V_0=228 meV, and thus all states remain bound. Among the transitions, the 5–8 transition exhibits the largest total absorption, followed by the 2–5 and 7–8 transitions. The absorption peak labeled **a** (corresponding to a photon energy of 10 meV) with a magnitude of 27×10^2 cm^{-1} arises from the combined contributions of the 9–10, 3–4, 1–2, and 6–7 transitions. Peak **b** is dominated by the 5–6 transition, peak **c** by the 7–8 and 5–7 transitions, peak **d** by the 2–5 transition, peak **e** by the 5–8 transition, peak **f** by the 2–7 transition, peaks near **g** by the 4–10 and 3–9 transitions, and peak **h** by the 1–8 transition.

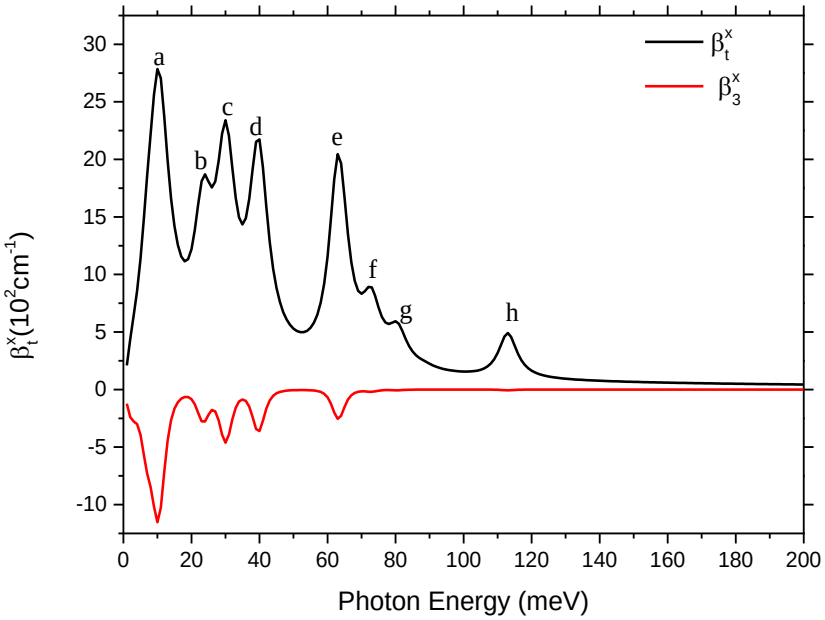

Figure 4. Total absorption as a function of photon energy with no external fields applied (under x-polarized excitation)

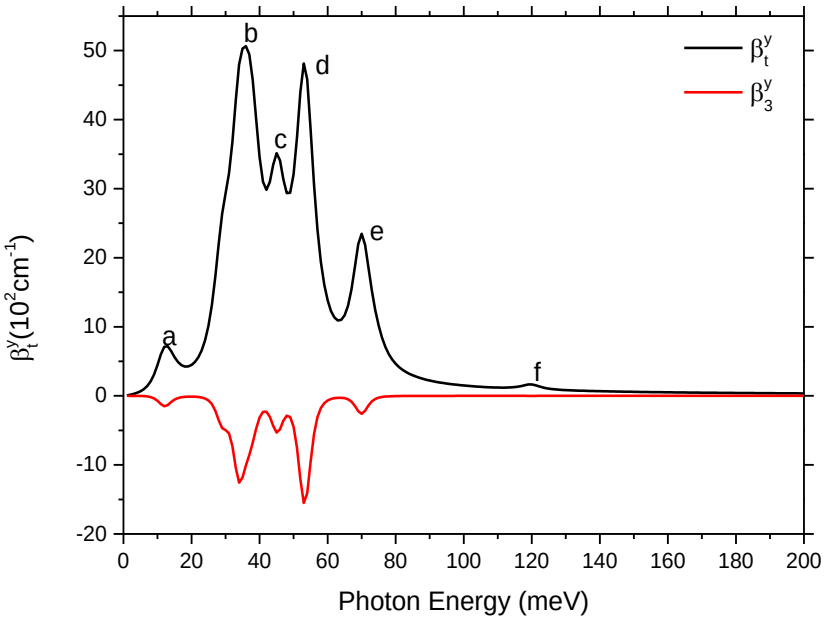

Figure 5. Total absorption as a function of photon energy with no external fields applied (under y-polarized excitation)

In Figure 5 (under *y*-polarized excitation), the lowest-photon-energy feature (a) arises from the 3–5 and 8–10 transitions; feature b results from the combined contributions of the 1–3, 7–9, and 2–4 transitions; feature c from 3–7; feature d from 6–10; feature e from 5–9 and 4–8; and, finally, feature f from 1–10. Compared with Figure 4, where the maximum total absorption is 27.5×10^2 cm^{-1}, the *y*-polarized case in Figure 5 reaches 50×10^2 cm^{-1}. While 13 allowed transitions are observed for *x*-polarization, 10 allowed transitions are identified for *y*-polarization (values below 0.1×10^2 cm^{-1} were not counted, though their effects are shown in the plot). The allowed transitions predominantly occur within the photon-energy range of 0–80 meV.

Investigating Figures 6–7, we observe that under x-polarized excitation the (total) refractive-index change is larger, with its principal feature appearing around a photon energy of ~10 meV, whereas under y-polarization the corresponding feature occurs near ~30 meV. Overall, y-polarization yields stronger absorption but smaller refractive-index changes.

In Figure 8, an *x*-polarized laser field is applied to the HQW. We plot the evolution of the energy levels as the laser amplitude increases. In general, all levels exhibit an upward shift. The E_2 and E_3 levels track each other up to approximately $50A^0$; beyond this value, E_3 decreases while E_4 continues to increase. A similar behavior is observed for E_5, E_6, and E_7 around 60 A^0 the three levels come very close to one another, after which only E_5 shows a decrease.

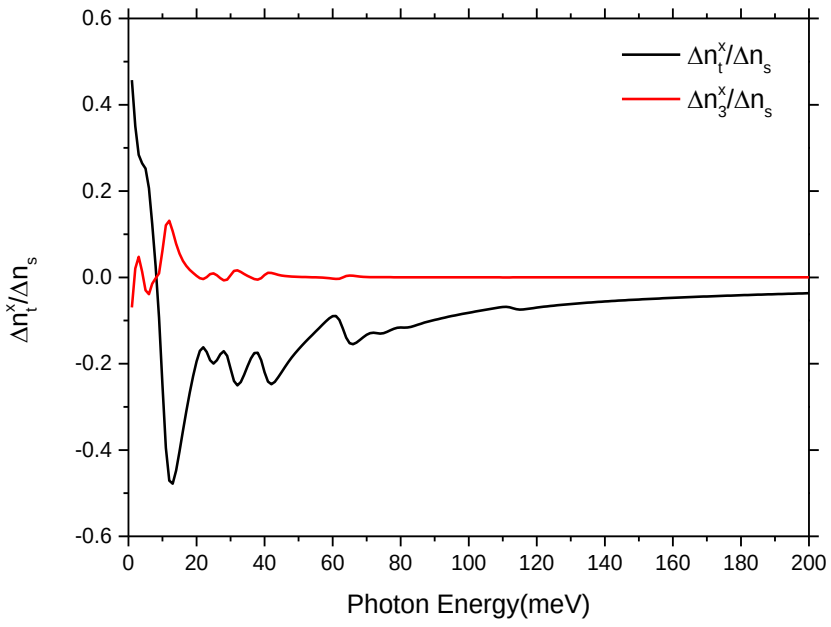

Figure 6. Total refractive-index change as a function of photon energy with no external fields applied (under x-polarized excitation)

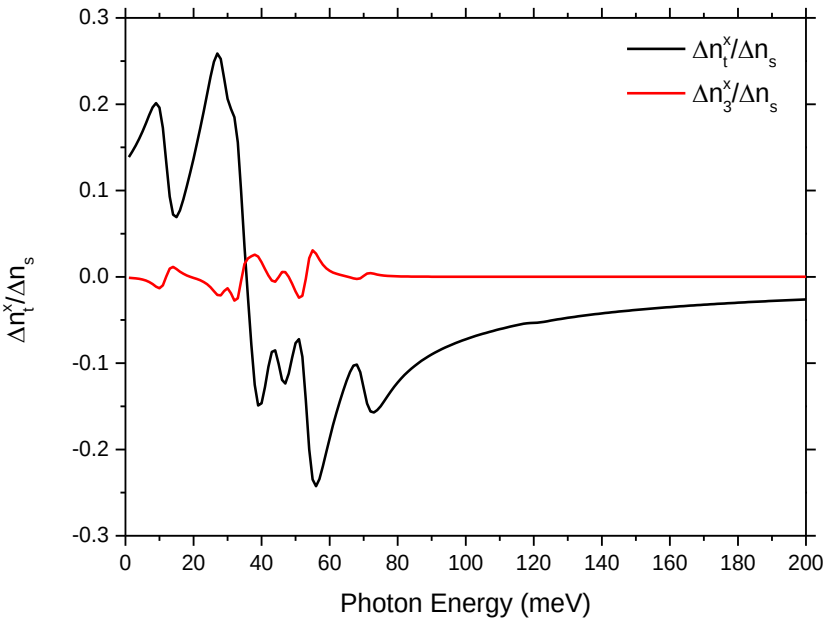

Figure 7. Total absorption as a function of photon energy with no external fields applied (under y-polarized excitation)

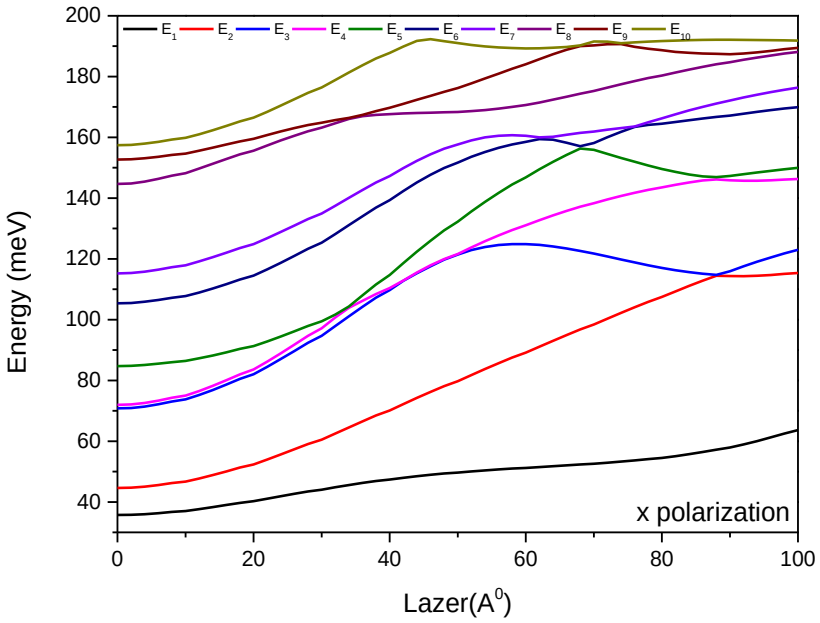

Figure 8. Evolution of energy levels under x-polarized laser excitation

In Figure 9, as the laser amplitude increases, the separation between E_1 and E_2 progressively narrows and the two levels approach near-degeneracy. A comparable trend is observed for E_6 and E_7. By contrast, E_3 and E_4 start nearly degenerate but their separation grows with increasing amplitude. Overall, increasing the laser amplitude leads to an upward shift in the energy spectrum.

In Figure 10, we first apply an *x*-polarized laser and evaluate the *x*-polarized optical response. Two laser amplitudes, α_x=40$A^0$and 80$A^0$are considered (solid curves). As the laser amplitude increases, the total absorption coefficient rises. At α_x=40A^0, the largest absorption occurs at a photon energy of ~23 meV and originates from the 8–10, 7–9, and 1–2 transitions; among the allowed transitions, 3–9 provides the strongest contribution. For α_x=40A^0 there are 12 allowed transitions (excluding those with absorption <0.1×10^2 cm^{-1}). When α_x=80A^0, ten allowed transitions remain, dominated by 6–10 and 2–4. All resonances lie within 0 −80 meV, with the largest peak associated with the 2–4 transition. When a *y*-polarized laser is applied to the HQW, the total absorption decreases. For α_y=40A^0, 13 allowed transitions are identified, with the strongest peak arising from 5–8; the total absorption spans 0−120 meV.

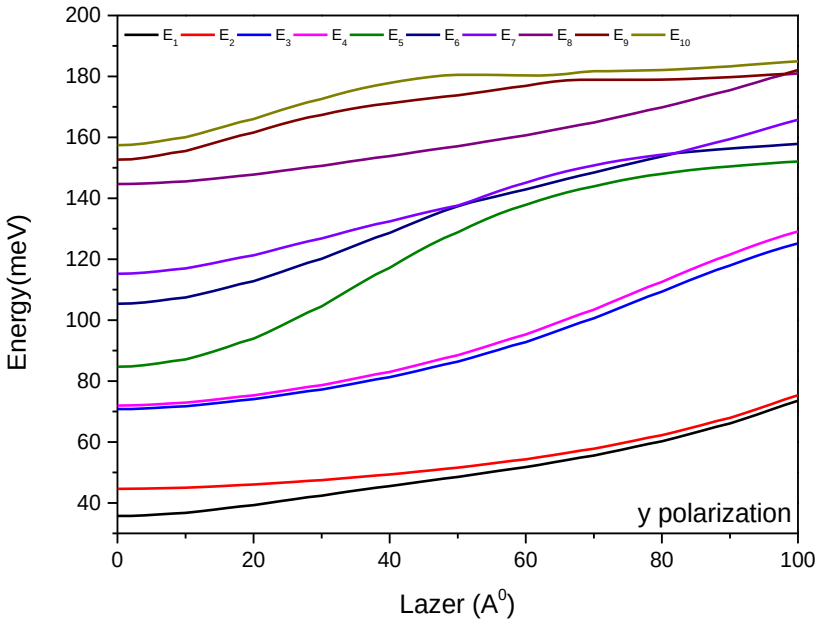

Figure 9. Evolution of energy levels under y-polarized laser excitation

For α_y=80A^0, the absorption in the 0–40 meV range is composed of the 9–10, 7–8, 6–7, 5–8, 5–6, 3–4, and 1–2 transitions, whereas the 60−120 meV range is dominated by 1–8, 2–5, 2–7, and 4–9.

In Figure 11, we evaluate the *y*-polarized optical response of the HQW. Two laser amplitudes, α_x=40A^0 and α_x=80A^0 are considered. For $\alpha = 0$ the total absorption exhibits two prominent peaks at photon

energies of approximately 34 meV and 51 meV. At α_x=40A^0 a clear peak appears near 48 meV, arising from the 2–5 and 6–10 transitions; among these, the 6–10 transition provides the strongest contribution. At higher photon energy (around 120 meV), the spectrum is formed by the 1–8 and 2–10 transitions. In total, twelve allowed transitions are identified. When the amplitude is increased to α_x=80A^0, there are again twelve allowed transitions; the dominant peak is due to the 5–9 transition. The 5–9, 4–8, and 3–5 transitions overlap, producing a feature around 38 meV. For a *y*-polarized laser, nine allowed transitions are observed at α_y=40A^0. Among these, the 6–10 transition exhibits the largest absorption. At α_x=80A^0, the principal feature occurs at a photon energy of ~30 meV its magnitude is lower than the total absorption obtained at α_y=40A^0. Contrary to the usual trend—namely, that increasing the laser amplitude enhances the total absorption—no increase is observed here.

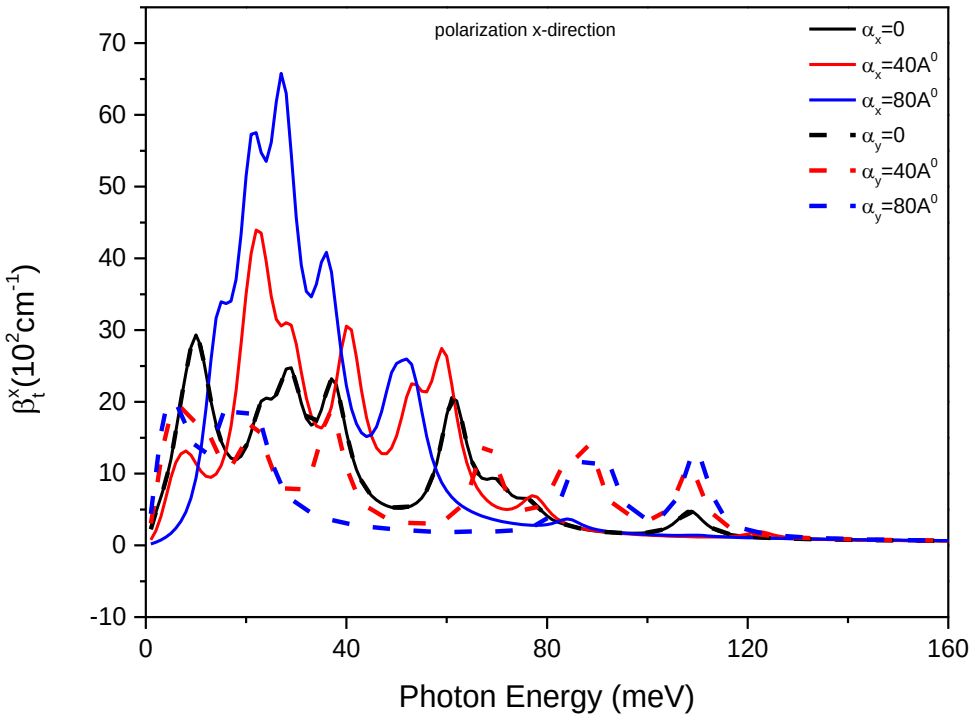

Figure 10. Total absorption as a function of laser amplitude (under x-polarized excitation)

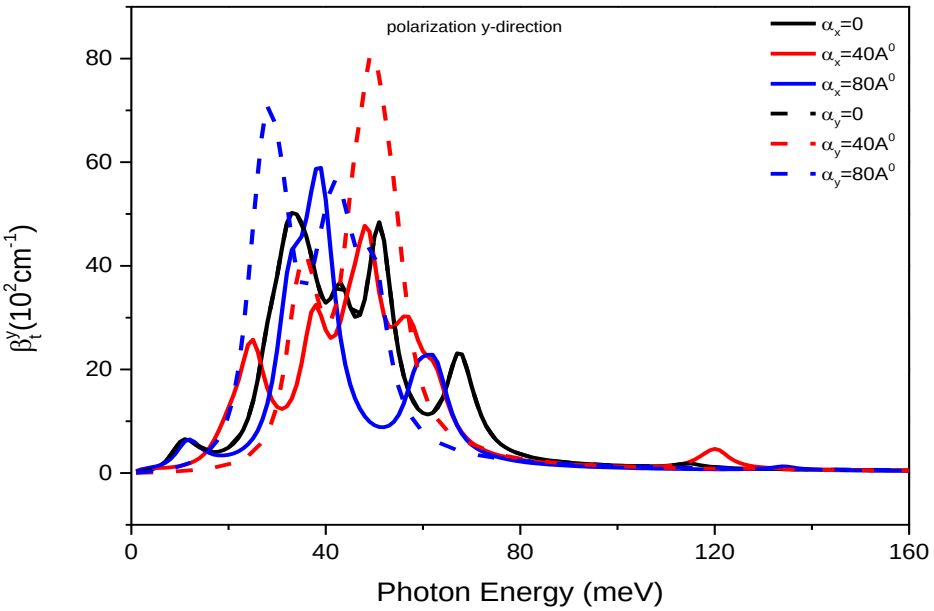

Figure 11. Total absorption as a function of laser amplitude (under y-polarized excitation)

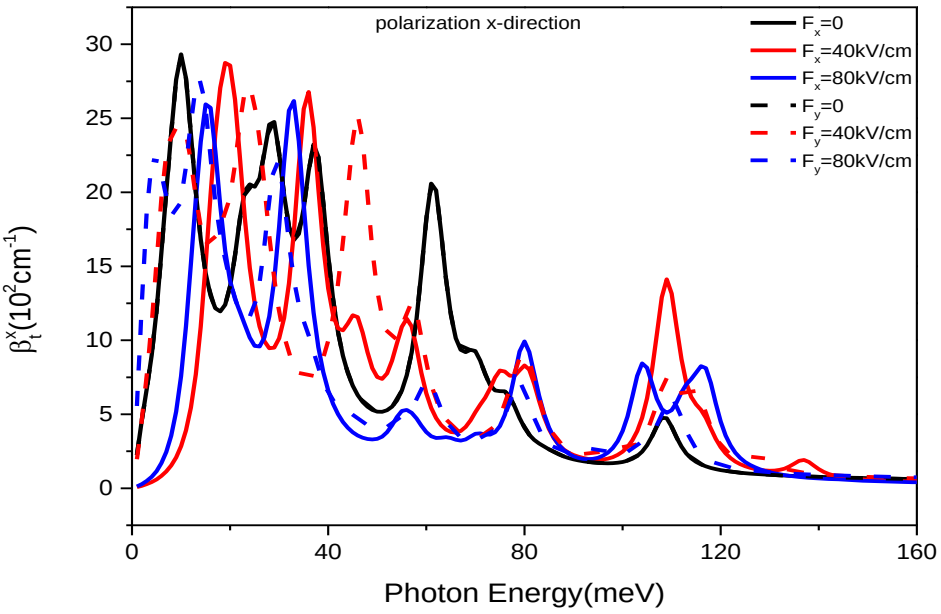

Figure 12. Total absorption as a function of electric field strength in the absence of laser excitation (under x-polarized excitation)

This behavior can be attributed to a reduction in the number of allowed transitions (down to seven). Overall, when the laser polarization is aligned with the material's optical polarization, the total absorption is enhanced.

In Figure 12, we compare the total absorption for F_x=40 kV/cm with the zero-field case F=0 (discussed in Figure 4). The feature labeled a appears shifted to higher photon energy; moreover, whereas a at F=0 was formed by the 6–7 and 1–2 transitions, at F_x=40 kV/ it arises from the 3–4, 4–6, and 8–9 transitions. Under F_x=40 kV/cm there are ten more allowed transitions than at F=0. The second peak from the left is composed of the 3–5 and 5–8 transitions. Another prominent feature appears at a photon energy of ∼109 meV, originating from the 2–9 and 2–10 transitions; its amplitude is larger than in the F=0F=0F=0 spectrum. For F_x=80 kV/cm the overall behavior is similar to the F_x=40 kV/cm case, but the peak near 57 meV increases in magnitude, and the ∼109 meV feature splits into two peaks.

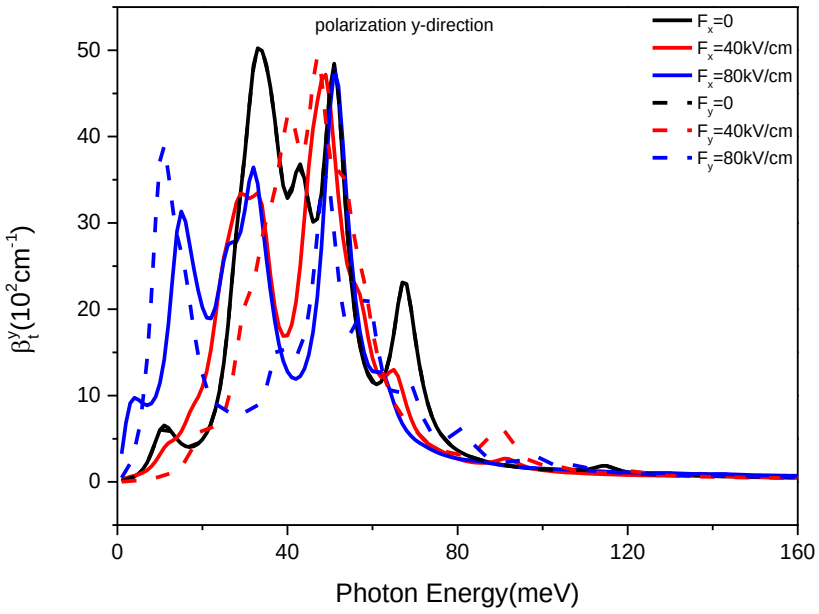

Figure 13. Total absorption as a function of electric field strength in the absence of laser excitation (under y-polarized excitation)

When the field is applied along *y*, F_y=40 kV/cm, the spectral characteristics change. The leftmost peak is formed by the 9–10, 6–7, and 1–2 transitions, while the next peak is due to 2–3, 4–6, 5–7, and 7–8. Another absorption feature near ∼46 meV results from the 5–8, 4–7, and 3–6 transitions. The peak around ∼50 meV vanishes and, instead, a new feature appears near ∼80 meV. For F_y=80 kV/cm, the peaks at ∼80 and

~110 meV have nearly equal amplitudes, and two additional peaks emerge in the 0−40 meV range; the leftmost of these is composed of many transitions, including 9–10, 8–10, and 8–9. In total, 33 of the 45 possible transitions are observed.

In Figure 13, we repeat the analysis of Figure 12, except that we evaluate the *y*-polarized optical response. The zero-field case (F=0) was discussed in Figure 5. For F_x=40 kV/cm, the total absorption magnitudes at photon energies of approximately 33 meV and 67 meV decrease relative to F=0. The spectra for F_x=80 kV/cm are nearly identical to those for F_x=40 kV/cm, although a new feature emerges near 15 meV. For F_y=40 kV/cm, the ~33 meV peak appears to shift toward ~41 meV compared with F=0F=0F=0. When the field is increased to F_y=80 kV/cm, a new absorption feature arises around 10 meV, while the peak near 49 meV is reduced. Overall, when the polarization of the optical probe (laser) is aligned with the material's optical polarization, the total absorption is enhanced. Beyond polarization, the total absorption also depends on the device geometry; the distinct responses for fields applied along the x and y directions indicate opportunities to engineer detectors and sensors by leveraging these anisotropies.

4. CONCLUSION

Beyond polarization, the total absorption also depends on the device geometry; the distinct responses for fields applied along the x and y directions indicate opportunities to engineer detectors and sensors by leveraging these anisotropies.

ACKNOWLEDGMENTS

This article was supported *by Trakya University Scientific Research Project (BAP) Center as within the scope of "Incentive Projects" project no. 2024/117*

REFERENCES

[1]. Bhattacharya, P., & Mi, Z. (2007). Quantum-dot optoelectronic devices. *Proceedings of the IEEE*, *95*(9), 1723–1740. doi:10.1109/JPROC.2007.900897

[2]. Yablonovitch, E., Jiang, H. W., Kosaka, H., Robinson, H. D., Rao, D. S., & Szkopek, T. (2003). Optoelectronic quantum telecommunications based on spins in semiconductors. *Proceedings of the IEEE*, *91*(5), 761–780. doi:10.1109/JPROC.2003.811799

[3]. Miller, D. A. B. (1990). Quantum well optoelectronic switching devices. *International Journal of High Speed Electronics and Systems, 1*(1), 19–46. doi:10.1142/S0129156490000034

[4]. Bhattacharya, P., Ghosh, S., & Stiff-Roberts, A. D. (2004). Quantum dot opto-electronic devices. *Annual Review of Materials Research, 34*, 1–40. doi:10.1146/annurev.matsci.34.040203.111535

[5]. Joulain, K., Drevillon, J., Ezzahri, Y., & Ordonez-Miranda, J. (2016). Quantum thermal transistor. *Physical Review Letters, 116*(20), 200601. doi:10.1103/PhysRevLett.116.200601

[6]. Simmons, J. A., Blount, M. A., Moon, J. S., Lyo, S. K., Baca, W. E., Wendt, J. R., Reno, J. L., & Hafich, M. J. (1998). Planar quantum transistor based on 2D–2D tunneling in double quantum well heterostructures. *Journal of Applied Physics, 84*(10), 5626–5634. doi:10.1063/1.368610

[7]. Wang, B., Wang, J., & Guo, H. (2003). Quantum spin field effect transistor. *Physical Review B, 67*(9), 092408. *(doi bilgisi verilmemiş)*

[8]. Marti, A., Cuadra, L., & Luque, A. (2000). Quantum dot intermediate band solar cell. In *Conference Record of the Twenty-Eighth IEEE Photovoltaic Specialists Conference* (pp. 940–943). doi:10.1109/PVSC.2000.916039

[9]. Kumar, S., Nehra, M., Deep, A., Kedia, D., Dilbaghi, N., & Kim, K.-H. (2017). Quantum-sized nanomaterials for solar cell applications. *Renewable and Sustainable Energy Reviews, 73*, 821–839. doi:10.1016/j.rser.2017.01.172

[10]. Sharma, D., Jha, R., & Kumar, S. (2016). Quantum dot sensitized solar cell: Recent advances and future perspectives in photoanode. *Solar Energy Materials and Solar Cells, 155*, 294–322. doi:10.1016/j.solmat.2016.05.062

[11]. Zhang, X., Eperon, G. E., Liu, J., & Johansson, E. M. J. (2016). Semitransparent quantum dot solar cell. *Nano Energy, 22*, 70–78. doi:10.1016/j.nanoen.2016.01.006

[12]. Kim, H., Han, J. Y., Kang, D. S., Kim, S. W., Jang, D. S., Suh, M., Kirakosyan, A., & Jeon, D. Y. (2011). Characteristics of $CuInS_2$/ZnS quantum dots and its application on LED. *Journal of Crystal Growth, 326*(1), 90–93. doi:10.1016/j.jcrysgro.2011.01.059

[13]. Yang, W., Li, J., Zhang, Y., et al. (2014). High density GaN/AlN quantum dots for deep UV LED with high quantum efficiency and temperature stability. *Scientific Reports, 4*, 5166. doi:10.1038/srep05166

[14]. Bai, H., Jin, X., Ma, X., Zhao, Y., Wang, H., Yu, J., Ding, L., Wei, C., Zhou, H., & Chen, W. (2024). Efficient preparation strategy of high quantum yield multicolor CDs for warm white LED. *Chemical Engineering Journal, 488*, 150980. doi:10.1016/j.cej.2024.150980

[15]. Çakır, B., Yakar, Y., & Özmen, A. (2012). Refractive index changes and absorption coefficients in a spherical quantum dot with parabolic potential. *Journal of Luminescence, 132*(10), 2659–2664. doi:10.1016/j.jlumin.2012.03.065

[16]. Lu, L., Xie, W., & Hassanabadi, H. (2011). Linear and nonlinear optical absorption coefficients and refractive index changes in a two-electron quantum dot. *Journal of Applied Physics, 109*(6), 063108. doi:10.1063/1.3560541

[17]. Vahdani, M. R. K., & Rezaei, G. (2010). Intersubband optical absorption coefficients and refractive index changes in a parabolic cylinder quantum dot. *Physics Letters A, 374*(4), 637–643. doi:10.1016/j.physleta.2009.11.038

[18]. Karabulut, İ., & Baskoutas, S. (2008). Linear and nonlinear optical absorption coefficients and refractive index changes in spherical quantum dots: Effects of impurities, electric field, size, and optical intensity. *Journal of Applied Physics, 103*(7), 073512.

[19]. Rezaei, G., Vaseghi, B., Taghizadeh, F., Vahdani, M. R. K., & Karimi, M. J. (2010). Intersubband optical absorption coefficient changes and refractive index changes in a two-dimensional quantum pseudodot system. *Superlattices and Microstructures, 48*(5), 450–457. doi:10.1016/j.spmi.2010.08.009

[20]. Bahar, M. K., & Başer, P. (2023). The second, third harmonic generations and nonlinear optical rectification of the Mathieu quantum dot with the external electric, magnetic and laser field. *Physica B: Condensed Matter, 665*, 415042. doi:10.1016/j.physb.2023.415042

[21]. Sayrac, M. (2022). Effects of applied external fields on the nonlinear optical rectification, second, and third-harmonic generation in an asymmetrical semi exponential quantum well. *Optical and Quantum Electronics, 54*, 52. doi:10.1007/s11082-021-03425-6

[22]. Frigerio, J., Ciano, C., et al. (2021). Second-harmonic generation in germanium quantum wells for nonlinear silicon photonics. *ACS Photonics, 8*(12), 3573–3582. doi:10.1021/acsphotonics.1c01162

[23]. Sakıroglu, S. (2017). Electric-field-induced nonlinear optical rectification, second- and third-harmonic generation in asymmetrical quantum well. *Süleyman Demirel Üniversitesi Fen Bilimleri Enstitüsü Dergisi, 21*(2), 367–372. doi:10.19113/sdufbed.82549

[24]. Bekar, B., Boz, F. K., Aktas, S., & Okan, S. E. (2019). The effect on the optical absorption coefficients due to the positions in the plane of square GaAs/Al(GaAs) quantum well wire under the laser field. *Acta Physica Polonica A, 136*(6).

[25]. Sayrac, H., Tuzemen, A. T., Al, E. B., Sayrac, M., & Ungan, F. (2025). Examination of influences of external fields and structural parameters on the nonlinear optical properties of the GaAs/GaAlAs single quantum well with modified Lennard-Jones potential. *Physica Scripta*, *100*(7), 075934.

[26]. Altun, D. (2025). Optical rectification and second harmonic generation in different shape GaAs/AlGaAs double quantum wells under electric and magnetic fields. *International Journal of Modern Physics B*, *39*(22), 2550200. doi:10.1142/S0217979225502005

[27]. Barseghyan, M. G., Duque, C. A., Niculescu, E. C., & Radu, A. (2014). Intense laser field effects on the linear and nonlinear optical properties in a semiconductor quantum wire with triangle cross section. *Superlattices and Microstructures*, *66*, 10–22. doi:10.1016/j.spmi.2013.11.023.

AN ALTERNATIVE NATURAL PRESERVATIVE FOR FOOD INDUSTRY: BEE BREAD

Ş. Yanardağ Karabulut[1], *H.A. Güleç*[2], *H. Şanlıdere Aloğlu*[1]

[1]*Department of Food Engineering, Faculty of Engineering, Kırklareli University, Kırklareli, TÜRKİYE*
[2]*Department of Food Engineering, Faculty of Engineering, Trakya University, Edirne, TÜRKİYE*

E-mail: seydakarabulut@klu.edu.tr

Abstract

The increasing global population and enduring malnutrition alongside the accelerated depletion of natural resources, represent major challenges to global food security. Therefore, food products with extended shelf lives are crucial for food availability. Increasing consumer awareness has led the food industry to seek natural alternatives to synthetic food additives used to extend shelf life.

Beekeeping products offer a rich variety, including honey, bee bread, pollen, royal jelly, and propolis. Bee bread is a beekeeping product produced by honeybees, who add their saliva to the pollen they collect, provide an anaerobic environment with a small amount of honey, and then ferment and mature it in the hive. With its nutritious, antioxidant, and antimicrobial properties, as well as its natural microbial flora, bee bread plays a crucial role in the development of young bees. From past to present, many beekeeping products have found widespread use both as food sources and for apitherapy purposes. However, despite its high nutritional and bioactive compound content, bee bread has been limited in direct consumption due to its low sensory appeal. Hence, harnessing the nutritionally rich composition of bee bread as a functional food ingredient holds considerable importance.

This study provides a summary of research on the importance of bee bread, focusing on its antioxidant and antimicrobial properties, the extraction of its bioactive components, and its potential applications as a food ingredient. Additionally, studies on the use of natural materials in dairy products are summarized, emphasizing the oxidation problem in dairy products. This study aims to raise awareness for bee bread, provide perspectives for new studies, and underline its usability as a product input in many foods, including dairy products.

Keywords: bee bread, antioxidant, antimicrobial, bioactive components.

1. INTRODUCTION

Honey, bee bread, and propolis are nutritious beekeeping products that have many important health benefits. Bee bread is a product that bees ferment by adding their saliva to pollen collected from plants [1]. Honey and bee bread have antimicrobial properties due to their high sugar content, acidity, hydrogen peroxide, and phytochemicals [1]. Bee bread is claimed to have more nutritional value than honey as it is richer in phenolic compounds, vitamins and essential minerals such as magnesium, calcium, potassium and zinc [2].

While the nectar and pollen are important for colony sustainability, pollen also has a special significance for meeting bees' basic protein needs and for its essential amino acid content [3]. The conversion of nectar into honey meets bees' carbohydrate needs, while the conversion of pollen into bee bread meets their protein, lipid, vitamin, and mineral needs [4]. Bees initiate the fermentation process by adding special digestive enzymes (salivary enzymes) containing lactic acid bacteria to the pollen they collect from flowers [3,5,6]. Fermentation occurs at 35-36°C in approximately two weeks [7]. Anaerobic fermentation is achieved by adding honey to the hive cell [8]. Thus, pollen is converted into bee bread with much higher bioavailability and storage stability [3,9]. This resulting bee bread constitutes the primary food of both bee larvae and young bees [5].

Bee bread is a valuable antioxidant that eliminates free oxygen and its negative effects in the body [3]. It is also known to have antibacterial, anticancer, hepatoprotective, immunomodulatory, therapeutic, and tumor and inflammation-preventing properties [3,5,7,8]. It is also known to have positive effects on the liver, nervous, cardiovascular, and endocrine systems, supports tissue regeneration, and regulates metabolism, especially lipid metabolism [7,9]. It is also known to be good for depression, stress, attention deficit, and forgetfulness [9].

Bee bread contains significant amounts of proteins, essential amino acids, macro and microelements, reducing sugars, essential polyunsaturated fatty acids, tocopherols, phytosterols, carotenoid pigments, enzymes, coenzymes, B vitamins and vitamin K [3,9]. Due to all these nutritional properties, bee bread can be considered a food supplement or functional food [5]. However, bee bread is considered an idle product by some beekeepers, causing the product's availability in the market to be limited and its price to be high [5]. Until the last few years, bee bread was removed from the hive by damaging it, which prevented beekeepers from utilizing this product [4,10]. Recently developed special materials and tools have enabled bee bread to be collected from the hive without damaging it, removing the obstacles to production [4].

2. COMPOSITION AND ANTIOXIDANT PROPERTIES OF BEE BREAD

Bee bread is a beekeeping product containing 20% protein, 24-35% carbohydrates, 3% lipids, 3% minerals and vitamins (B1, B2, C, E, K, biotin, folic acid, nicotinic acid and pantothenic acid), polyphenols, sterols, enzymes (amylase, saccharase, phosphatases, glucose-oxidase and amylase) and carotenoids [11]. Bee bread contains significant amounts of amino acids (glutamic acid, proline, aspartic acid, arginine, histidine, valine, leucine, isoleucine, methionine, lysine, tryptophan, threonine, phenylalanine, cysteine, alanine, tyrosine, glycine and serine) [11]. Bee bread is also rich in polyphenols, which have antioxidant and antimicrobial properties.

The total phenolic substance content of bee bread was found to be 26.7-43.4 mg GAE/g, total flavonoid content was found to be 2.6-4.4 mg QE/g, total protein content was found to be 17.6-22.2%, and total fatty acid content was found to be 67.6-86.5% [3]. In Malaysia, protein content in bee bread was determined as 21.7–23.3%, carbohydrate content as 57.1–58.9%, and glucose (the predominant sugar) as 11.5 g/100 g. It has been determined that bee bread contains all the essential amino acids (arginine in the highest proportion). The most abundant minerals were potassium (6706 mg/kg), phosphorus and magnesium, respectively. Bee bread samples from Malaysia contained 17.2–18.4 g/100 g total protein, 32.7–59.6 g/100 g total carbohydrate, 2.2–4.8 g/100 g total fat, 1020.5–1478 kcal/100 g total energy, 14.2–15.4 mg GAE/g total phenolics, and 2.9–3.9 mg QE/g total flavonoids [8].

The % fructose, % glucose, fructose/glucose ratio, total polyphenol, and total flavonoid contents of bee bread were determined as 14.0–19.6; 6.4–15.1; 1.5–2.2; 5.7–12.8 mg GAE/g; and 23.6–36.2 mg QE/g, respectively [9]. Analysis of bee bread composition showed that the most abundant element was potassium (5515–7487 ppm), followed by calcium, magnesium, and chromium. The n-6/n-3 fatty acid ratio was high, ranging from 0.9 to 1.4, and the composition was rich in unsaturated fatty acids, indicating high nutritional value [12]. Moisture in bee bread was determined as 13.3–13.5%, ash as 3.8–4.2%, and the most abundant minerals were zinc (3.09–3.10 ppm), iron (1.74–1.83 ppm), manganese (1.11–1.20 ppm), and copper (0.59–0.65 ppm) [14]. Analysis of bee bread composition showed that the moisture content was 15.7% ± 3.6 g, and the ash, fat, and protein contents in the dry matter were 2.4% ± 0.2, 3.4% ± 1.1, and 23.1% ± 2.9 g, respectively [4]. In vitro bioavailability was determined to be 79 ± 16 g hydrolyzed protein/100 g total protein [4]. Total flavonoid and phenolic compositions were determined as 3.2 ± 1.0 mg quercetin/g and 8.9 ± 3.1 mg gallic acid/g, respectively [4]. According to FRAP and ABTS results, antioxidant activity was determined as 46.1 ± 13.0 and 61.5 ± 10.2 µmol TROLOX/g, respectively [4].

3. ANTIBACTERIAL PROPERTIES OF BEE BREAD

The resistance of microorganisms to antibiotics has made studies on the investigation of natural antibacterial compounds and the determination of their effectiveness levels popular [6]. Bee bread is a valuable beekeeping product that can be used both as and in the pharmaceutical industry with its antimicrobial properties [6]. Bee bread exhibits targeted antimicrobial activity against pathogens and, unlike synthetic antimicrobials, modulates the host microbiome in a prebiotic manner [14].

In the studies, the minimum inhibitory concentration (MIC) of bee bread (2 g/100 mL) was 0.04 for *B. cerus* [10], 0.01-0.25 for *E. coli* [10,11], *En. cloacae* 0.18 [10], *Klebsilla pneumonia* 0.1 [11], *L. monocytogenes* 0.18 [10], *Salmonella typhi* 0.008 [11], *S. typhimurium* 0.18 [10], *S. aureus* 0.18 [10], Shigella 0.1 [11], *A. fumigatus* 0.5 [10], *A. ochraceus* 0.35 [10], *A. niger* 1.0 [10], *P. funiculosum* 0.7 [10], and *P. ochrochloron* and *P. cyclopium* 1.0 mg/mL.

Investigation of the antimicrobial properties of aqueous extracts of bee bread at different concentrations (1.04–33%) on *Bacillus cereus*, *Staphylococcus aureus*, *Escherichia coli*, *Salmonella enterica*, and *Pseudomonas aeruginosa* revealed that extracts at 16.6% and 33% exhibited stronger antimicrobial effects, with the highest activity observed against *Staphylococcus aureus* within 8–12 hours [6]. The minimum inhibitory concentrations (MIC) of 70% ethanol extract of bee bread for *B. subtilis*, *S. aureus*, *E. coli*, and *Salmonella* were found to range from <6.67 to 33.33 µL/mL [15].

4. EXTRACTION OF BEE BREAD

Total phenolic content in bee bread was highest in methanol (22.72 mg GAE/g) and lowest in water (8.32 mg GAE/g). Flavonol and flavone contents were highest in methanol (0.696 mg QE). The highest flavanone contents were found in methanol and water extracts (7.86 and 6.04 mg NAE/g, respectively). Furthermore, methanol extracts exhibited the highest antioxidant activity [16]. Sequential extractions of bee bread were performed using n-hexane (non-polar), diethyl ether (slightly polar), and methanol (polar), resulting in the identification of more than 200 compounds. The components of honeycomb wax were separated with hexane, the more polar carboxylic acids and phenols with ether, and the polar carbohydrate compounds (mono- and disaccharides, carbohydrate acids) with methanol [17]. The ethanolic extract of bee bread exhibited the highest free radical scavenging activity, with values of 93.60% (DPPH) and 97.95% (ABTS). Unlike the DPPH test, the FRAP test results were higher in the hexane extract. Ethanol-extracted samples exhibited stronger antimicrobial activity compared to those extracted with hexane. [18].

For extraction, 1 g of bee bread was mixed with 30 mL of a methanol/water mixture (80:20 v/v) at 25 °C and 150 rpm for 60 minutes, followed by filtration. The residue was re-extracted with 30 mL of

hydromethanol mixture and the combined supernatants were evaporated under reduced pressure (rotary evaporator) to remove methanol [10]. In another study water and ethanol were used for extraction. Fifty grams of powdered bee bread was mixed with 10 volumes of distilled water or 70% ethanol and left to stand in the dark at room temperature for 72 hours. After maceration, each solution was stirred with a magnetic stirrer at 500 rpm for 10 minutes and then centrifuged at 4000 rpm for 10 minutes. Tests for flavonoids, phenols, resins, saponins, tannins, terpenoids, and xanthoproteins in the extracts gave positive results. Ethanol extracts showed higher total phenolic and flavonoid contents, as well as higher antioxidant activity [8]. For the extraction of bee bread, 70% ethyl alcohol was used. Specifically, 250 g of 70% ethanol was added to every 25 g of bee bread, and the mixture was boiled in a Soxhlet apparatus for 2 hours [19].

5. USE AS A FOOD INPUT

Increasing cases of cardiovascular diseases, diabetes, obesity and various cancers are increasing the need for quality, safe and nutritious foods [20]. To meet consumer demand, the food industry has developed specific technologies that enhance the natural quality of food by adding compounds such as ω-3 fatty acids, vitamins, minerals, probiotics and antioxidants [21,22].

However, despite the demonstrated potential of bee bread and its components in vitro, their effectiveness in food systems may be affected by factors such as concentration and solubility, extraction method, interaction with the food matrix, pH, temperature, contamination level, etc. [19]. Because the use of these active molecules in industrial processes shows high reactivity to environmental conditions such as light, moisture and oxygen, which cause degradation and loss of functional properties [21].

The proximate composition as well as the antioxidant and antibacterial activities of fish sausages enriched with ethanolic extract of bee bread (BBE) at concentrations of 0.25%, 0.5%, and 0.75% were analyzed [19]. Enrichment of fish sausages with 0.75% BBE increased the phenolic and flavonoid content from 8.05 ± 0.24 mg/g to 23.46 ± 1.60 mg GAE/g. Antioxidant activity for 0.75% BBE fish sausage showed the highest DPPH scavenging activity compared to the synthetic additive BHT. After 28 days of frozen storage, the lipid oxidation activity of fish sausages containing 0.75% BBE showed similar results to BHT, while having lower thiobarbituric acid reactive substances (TBARS) values than the negative control. Additionally, BBE was able to inhibit the foodborne pathogens tested, even being found to be more effective than tetracycline. It has been shown that the addition of BBE to fish sausage keeps the total viable count below 6 log CFU/g within 6 days after frozen storage.

6. OXIDATION PROBLEM IN DAIRY PRODUCTS

Lipid oxidation is one of the major causes of spoilage in foods containing high polyunsaturated fatty acids [19]. Oxidation leads to the development of off-odors, undesirable flavors, slimy texture, discoloration, formation of toxic compounds, and loss of nutrients [19].

Synthetic antioxidants and preservatives are frequently used in industrial processing to reduce harm to the human body and increase the storage stability of foods. However, it has been determined that synthetic additives can cause nutrient loss and even have toxic effects [23]. In recent years, natural antioxidants and preservatives obtained from edible materials, edible have become of interest because they can protect the human body from free radicals and delay the progression of many chronic diseases. Polyphenols exhibit various biological and pharmacological activities, including antioxidant, antibacterial and anticancer [23]. For this reason, there are many studies on the use of phenolic compounds as antioxidants.

It was reported that α-tocopherol added to butter exhibited activity equivalent to that of synthetic antioxidants [24]. Therefore, it is recommended to use α-tocopherol as a natural antioxidant to suppress the development of rancidity in butter. When 1–5% rosemary extract was added to soft cheese (1.5% fat), it was determined that increasing the concentration to 5% resulted in a product with more acceptable taste, texture, structure, and antioxidant activity for up to 30 days [25]. Gallic acid, caffeic acid, and catechin at 80 mg/L each inhibited butter oxidation at 50 °C as effectively as 200 mg/L BHA, while 80 mg/L gallic acid was found to be more effective than 200 mg/L BHA in preventing butter oxidation at 110 °C [26].

In recent years, foods containing bee pollen and propolis, such as baked goods, beverages, and meat, have attracted considerable attention. However, few studies have been conducted on products containing bee bread extract.

7. NATURAL ANTIOXIDANT AND ANTIMICROBIAL SOURCES USED IN DAIRY PRODUCTS

Despite its rich nutritional content and product diversity, milk and dairy products are a food group with a high risk of pathogens. According to the FDA, unpasteurized raw milk can carry dangerous foodborne pathogens such as *Campylobacter*, *Escherichia coli*, *Listeria*, and *Salmonella* [27]. Additionally, milk and dairy products are often associated with the presence of *Staphylococcus aureus*, which is considered a dangerous threat to the safety of the products [28]. *Cronobacter sakazakii*, *Salmonella enteritidis* and *Bacillus cereus* species are also common foodborne poisoning bacteria in dairy products [29].

Therefore, the prevention of various foodborne pathogens through the addition of natural substances and their extracts to various dairy products, including milk, is a current topic of study [27,29]. These extracts contain many bioactive compounds such as anthocyanins, carotenoids, fatty acids, flavonoids, phenolic

compounds and vitamins [29]. Combining dairy products with plant components allows regulating the content of vitamins, carbohydrates, minerals and dietary fiber and giving the product a plant taste, smell and an attractive appearance [30]. Aqueous extracts of thyme, marjoram, sage and licorice are widely used in the production of functional milk beverages [30]. Blueberry leaves, green tea, honeysuckle powder, *Aronia melanocarpa*, thyme extract, pomegranate, orange, lemon, apple, grapefruit, tangerine, date, scorzonera (a member of the Asteraceae family with purple-brown edible roots), and caltrop have been investigated as potential antimicrobial and antioxidant additives in milk and dairy products [30]. In addition to their antibacterial effect, plant additives can also prevent oxidative degradation of dairy products. They achieve this by directly absorbing light photons, eliminating radicals, and preventing photodegradation and oxidation [30]. The antioxidant properties of plant extracts not only protect the product from spoilage but also slow down the aging process by inhibiting the action of free radicals in the human body [29].

In the studies, *Hibiscus sabdariffa* L. (Roselle) extract was found to be effective against *Staphylococcus aureus* (complete inhibition), *Salmonella enteritidis* (partial inhibition), *Listeria monocytogenes* (partial inhibition), *Escherichia coli* (partial inhibition), *Cronobacter sakazakii* (partial inhibition) and *Bacillus cereus* (partial inhibition) [27], essential oils of the Lamiaceae family were found to be effective against *Staphylococcus aureus* (partial inhibition), [28], *K. parviflora* (black ginger) extract was found to be effective against *Cronobacter spp*. and enterohemorrhagic *Escherichia coli* (EHEC) [31] *Aronia melanocarpa* (black chokeberry) extract was determined to be effective against *Bacillus cereus* (complete inhibition) and *Staphylococcus aureus* (partial inhibition) [29].

8. CONCLUSION

Consumer awareness of synthetic additives has increased interest in natural food sources. While interest in beekeeping products is growing, the usability of these products as food inputs requires further research and studies on new product development and their use as natural additives. With its rich composition, bee bread has recently attracted attention as an alternative to synthetic additives. Compared to other bee products, bee bread stands out for its high acidity, low water activity, high lactic acid content, high bioavailability, and rich composition. Therefore, it is important to safely include bee bread as a food supplement in the daily human diet. However, few studies have been found on the use of bee bread in food formulations.

The studies summarized in this article demonstrate that bee bread possesses high antimicrobial and antioxidant properties, and can extend the shelf life of foods while also imparting functional properties. Milk and dairy products are among the food sectors most researched for natural additives due to their nutritional

importance and their susceptibility to microbial and oxidative spoilage. Therefore, we emphasize the potential use of bee bread extract as an additive in dairy products due to its antibacterial and antioxidant properties.

ACKNOWLEDGMENTS

This study was supported by the Scientific Research Project Units of Kırklareli University and Trakya University.

REFERENCES

[1] Ngalimat, M.S., Raja Abd. Rahman, R.N.Z., Yusof M.T., Syahir, A., Sabri, S., 2019. Characterisation of bacteria isolated from the stingless bee, Heterotrigona itama, honey, bee bread and propolis. PeerJ life and environment, 7:e7478 DOI 10.7717/peerj.7478.

[2] Khalifa, S. A. M., Elashal, M., Kieliszek, M., Ghazala, N. E., Farag, M. A., Saeed, A., Xiao, J., Zou, X., Khatib, A., Göransson, U., El-Seedi, H. R., 2020. Recent insights into chemical and pharmacological studies of bee bread. Trends in Food Science & Technology, 97, 300–316.

[3] Mayda, N., Özkök, A., Bayram, N. E., Gerçek, Y. C., Sorkun, K., 2020. Bee bread and bee pollen of different plant sources: determination of phenolic content, antioxidant activity, fatty acid and element profiles. Journal of Food Measurement and Characterization 14:1795–1809.

[4] Zuluaga, C. M., Serrato, J. C., Quicazan, M. C., 2015. Chemical, nutritional and bioactive characterization of Colombian bee-bread. Chemical Engineering Transactions, 43, 175-180 DOI: 10.3303/CET1543030.

[5] Mohammad, S. M., Rashid, K. M., Zawawi, N., 2020. Botanical origin and nutritional values of bee bread of stingless bee (Heterotrigona itama) from Malaysia. Journal of Food Quality, Article ID 2845757, 12 pages.

[6] Urcan, A. C., Criste, A., Dezmirean, D., Bobiş, O., Marghitaş, L., Margaoan, R., Hrinca, A., 2018b. Antimicrobial activity of bee bread extracts against different bacterial strains. Bulletin UASVM Animal Science and Biotechnologies 75(2): 85-92.

[7] Pavelkova, A., Hascik, P., Kalafova, A., Capcarova, M., Cubon, J., Bucko, O., Kacaniova, M., Hanusova, E., Tkacova, J., Bobko, M., 2020. chemical composition of muscle after bee bread application in the nutrition of Japanese quails. Journal of Microbiology, Biotechnology and Food Sciences 9 (4): 831-835.

[8] Othman, Z. A., Noordin, L., Ghazali W. S. W., Omar, N., Mohamed, M., 2019. Nutritional, phytochemical and antioxidant analysis of bee bread from different regions of Malaysia. Indian Journal of Pharmaceutical Sciences; 81(5):955-960.

[9] Urcan, A. C., Criste, A. D., Dezmirean D. S., Margaoan, R., Caeiro, A., Campos, M. G., 2018a. Similarity of data from bee bread with the same taxa collected in India and Romania. Molecules, 23, 2491; doi:10.3390/molecules23102491.

[10] Bakour, M., Fernandes, A., Barros, L., Sokovic, M., Ferreira, I. C. F. R., 2019. Bee bread as a functional product: Chemical composition and bioactive properties. LWT - Food Science and Technology, 109, 276–282.

[11] Suleiman, J.B., Mohamed, M., Abu Bakar, A.B., Nna, V.U., Zakaria, Z., Othman, Z.A., Aroyehun, A.B., 2021. Chemical profile, antioxidant properties and antimicrobial activities of Malaysian Heterotrigona itama bee bread. Molecules, 26, 4943. https://doi.org/10.3390/molecules26164943.

[12] Ciric, J., Spiric, D., Baltic, T., Janjic, J., Petronijevic, R., Simunovic, S., Djordjevic, v., 2019. Element concentration and fatty acid composition of Serbian bee bread. Earth and Environmental Science 333, 012050.

[13] Silvia, P., Jivan, A., Harmanescu, M., 2008. Bulletin UASVM Animal Science and Biotechnologies, 65: 1-2.

[14] Didaras, N. A., Karatasou, K., Dimitriou, T. G., Amoutzias, G. D., Mossialos, D., 2020. Antimicrobial activity of bee-collected pollen and beebread: state of the art and future perspectives. Antibiotics, 9, 811; doi:10.3390/antibiotics9110811.

[15] Akhir, R. A. M., Bakar, M. F. A., Sanusi, S. B., 2017. Antioxidant and Antimicrobial Activity of Stingless Bee Bread and Propolis Extracts. AIP Conference Proceedings 1891, 020090, https://doi.org/10.1063/1.5005423

[16] Oltica, S., Marghitaş, L. A., Dezmirean, D., 2007. Examination of antioxidant capacity of beebread extracts by different complementary assays. Bulletin USAMV-CN, 63–64.

[17] Isidorov, V. A., Isidorova, A. G., Sczczepaniak, L., Czyzewska, U., 2009. Gas chromatographic–mass spectrometric investigation of the chemical composition of beebread. Food Chemistry, 115, 1056–1063.

[18] Akhir, R. A. M., Bakar, M. F. A., Sanusi, S., B., 2018. Antioxidant and Antimicrobial Potential of Stingless Bee (Heterotrigona itama) By-Products. Journal of Advanced Research in Fluid Mechanics and Thermal Sciences, 42, 1, 72-79.

[19] Mohammad, S. M., Hisham, A. A. B., Mustapa, N. A., Chan, K. W., Zawawi, N., 2021. Proximate Analysis, Antioxidant Activity, and Antibacterial Activity of Fish Sausages Fortified with Bee Bread Extract. Journal of Food Quality, Article ID 6657553, 9 pages.

[20] Akbarbaglu, Z., Peighambardoust, S. H., Sarabandi, K., Jafari, S. M., 2021. Spray drying encapsulation of bioactive compounds within protein-based carriers; different options and applications. Food Chemistry, 359, 129965. https://doi.org/10.1016/j.foodchem.2021.129965.

[21] Piñón-Balderrama, C.I., Leyva-Porras, C., Terán-Figueroa, Y., Espinosa-Solís, V., Álvarez-Salas, C., Saavedra-Leos, M. Z., 2020. Encapsulation of Active Ingredients in Food Industry by Spray-Drying and Nano Spray-Drying Technologies. Processes, 8, 889; doi:10.3390/pr8080889.

[22] Pizzoferrato, L., Manzi, P., Marconi, S., Fedele, V., Claps, S., Rubino, R., 2007. Degree of antioxidant protection: a parameter to trace the origin and quality of goat's milk and cheese. J. Dairy Sci., 90, 4569–4574.

[23] Zhang, G., Hu, M., He, L., Fu, P., Wang, L., Zhou, J., 2013. Optimization of microwave-assisted enzymatic extraction of polyphenols from waste peanut shells and evaluation of its antioxidant and antibacterial activities in vitro. Food and Bioproducts Processing, 91, 158–168.

[24] Ozturk, S., Cakmakci, S., 2006. The effect of antioxidants on butter in relation to storage temperature and duration. Eur. J. Lipid Sci. Technol., 108, 951–959.

[25] El-Din, H. M. F., Ghita, E. I., Badran, S. M. A., Gad, A. S., El-Said, M. M., 2010. manufacture of low fat UF-soft cheese supplemented with rosemary extract (as natural antioxidant). Journal of American Science, 6, 10, 570–579.

[26] Soulti, K., Roussis, L. G., 2007. Inhibition of butter oxidation by some phenolics. Eur. J. Lipid Sci. Technol., 109, 706–709.

[27] Lim, H. W., Seo, K. H., Chon, J. W., Song, K. Y., 2020. Antimicrobial activity of Hibiscus sabdariffa L. (roselle) powder against food-borne pathogens present in dairy products: preliminary study. J. Dairy Sci. Biotechnol.;38(1):37-44.

[28] Abdolshahi, A., Naybandi-Atashi, S., Heydari-Majd, M., Salehi, B., Kobarfard, F., Ayatollahi S. A., Ata, A., Tabanelli, G., Sharifi-Rad, M., Montanari, C., Iriti, M., Sharifi-Rad, J., 2018. Antibacterial activity of some Lamiaceae species against Staphylococcus aureus in yoghurt-based drink (Doogh). Cellular and Molecular Biology, 71-77.

[29] Kim, D., H., Lim, H. W., Kim, S. H., Lee, J. M., Chon, J. W., Song, K. Y., Bae, D., Kim, J., Kim, H., Seo, K. H., 2018. Antibacterial activity of crude Aronia melanocarpa (black chokeberry) extracts against Bacillus cereus, Staphylococcus aureus, Cronobacter sakazakii, and Salmonella enteritidis in various dairy foods: preliminary study. J. Milk Sci. Biotechnol., 36(3),155-163.

[30] Sukhikh, S. A., Astakhova, L. A., Golubcova, Y. V., Lukin, A. A., Prosekova, E. A., Milent`eva, I. S., Kostina, N. G., Rasshchepkin, A. N., 2019. Functional dairy products enriched with plant ingredients. Foods and Raw Materials, 2019, 7, 2, 428-438.

[31] Jeong, D., Kim, D. H., Chon, J. W., Kim, H., Lee, S. K., Kim, H. S., Yim, J. H., Song, K. Y., Kang, I. B., Kim, Y. J., Park, J. H., Jang, H. S., Kang, S. H., Kim, S. K., Seo, K. H., 2016. Antibacterial effect of crude extracts of Kaempferia parviflora (krachaidam) against Cronobacter spp. and enterohemorrhagic Escherichia coli (EHEC) in various dairy foods: a preliminary study. J. Milk Sci. Biotechnol., 34, 2, 63-68.

REMOVAL OF CATIONIC METHYLENE BLUE DYE FROM WASTEWATER WITH COLEMANITE

Feray Bayça

Alanya Alaaddin Keykubat University, Rafet Kayis Engineering Faculty, Department of Engineering Basic Science, 07450 Alanya, Antalya, Türkiye.

E-mail:feray.bayca@alanya.edu.tr

Abstract

Methylene blue dye is most commonly used in the textile industry. Therefore, textile wastewater containing methylene blue is discharged into the environment. Methylene blue dye, which is harmful to the environment and human health, must be removed from wastewater before being discharged from the facility. This study investigated the removal of methylene blue (MB), a cationic dye, from aqueous solutions using colemanite as an adsorbent. The adsorption capacity, removal efficiency, adsorption isotherms and kinetic models of methylene blue on colemanite were investigated. The results showed that the adsorption of MB on colemanite was highly dependent on the initial MB concentration. The adsorption capacity was observed to increase significantly as the initial dye concentration increased. MB adsorption best fits the Dubinin-Radushkevich adsorption isotherm model. Among the kinetic model, the adsorption of MB on colemanite is consistent with the pseudo-second-order model due to the high correlation coefficient of the pseudo-second-order model. Colemanite may be a preferred adsorbent for MB because it is low-cost, effective, and environmentally friendly.

Keywords

Adsorption, Isotherm, Kinetics, Colemanite, Methylene blue

1 INTRODUCTION

Water pollution results in a significant environmental threat due to the contamination of groundwater and surface water resources. The leather, textile, and plastic industries, refineries, printing, and the petroleum and pharmaceutical industries use numerous dyes [1]. The textile industry is the main dye consumer, with a total consumption of 10,000 tons/year. These dyes are discharged into water resources as waste [2]. Dyes are divided into two categories based on their production method: natural and synthetic. Synthetic dyes such as benzene, naphthalene, anthracene, toluene, and xylene are used in textile production and are also widely used in many other industries [3]. Colemanite is a calcium borate compound with a monoclinic crystal structure, a density of 2.40 g/cm^3, and the chemical formula $Ca_2B_6O_{11}.5H_2O$.

Colemanite has lower solubility in water and higher solubility in acids. It is produced by open-pit mining by a company in the Bigadic district of Balikesir province, Türkiye. There, it is enriched through physical processes. The enriched product is sold as concentrated colemanite in various grain sizes and chemical compositions [4].

Various methods are used for the removal of dyes from wastewater, including sedimentation, filtration, chemical degradation with coagulation and flocculation agents, UV-assisted and chemical oxidation, electrochemical, aerobic and anaerobic biological degradation, advanced oxidation, ozonation, and membrane filtration [5]. However, these methods have some limitations. On the other hand, the adsorption method offers advantages such as ease of use, simplicity, low cost, high efficiency, short processing time, reusability of the adsorbent, and non-toxicity [6]. Important parameters affecting the adsorption process include the surface area of the adsorbent, the type of adsorbent and adsorbate, the particle size of the adsorbent, pH, and contact time [2]. There are studies in the literature on the removal of methylene blue from wastewater. Alshandoudi et al. [7] adsorbed methylene blue using zinc oxide nanocomposite with activated carbon synthesized from palm leaves. Munir et al. [8] adsorbed methylene blue using black clay modified with didocyldimethylammonium bromide. Bhattacharyya et al. [9] successfully adsorbed methylene blue using an adsorbent prepared from neem leaves.

The aim of this article was to investigate the adsorption of methyleneblue, a dye in wastewater that poses a threat to the health of all living things, on to colemanite using a batch adsorption process. The effects of contact time, adsorbent dosage, initial MB concentration and temperature on the adsorption capacity of colemanite were researched. Langmuir, Freundlich, and Dubinin-Radushkevich isotherm models were examined to determine the isotherm model of the adsorption process. Parameters of pseudo-first-order (PFO) and pseudo-second-order (PSO) kinetic models were found.

2 MATERIALS AND METHODS

Ground colemanite ($2CaO.3B_2O_3.5H_2O$), produced at the Eti Maden Balıkesir-Bigadiç facility, was selected as the adsorbent in the adsorption studies. Methylene blue ($C_{16}H_{18}N_3SCl$ and 319.85 g/mol) was supplied by Isolab Laborgerate GmbH. The homogeneous supernatant was collected, and absorbance values at 665 nm were found with a UV-VIS spectrophotometer.

The adsorption capacity (q_e), was found utilizing the following Equation 1:

$$q_e = \frac{(C_o - C_e)\,V}{m} \qquad (1)$$

Adsorption MB removal efficiency (*RE*) was found with Equation 2.

$$\text{Removal efficiency} = \frac{(C_o - C_e)\,100}{C_o} \qquad (2)$$

where, q_e is the adsorption capacity in mg/g, C_o is the initial concentration in mg/L, C_e is the equilibrium concentration, m is the adsorbent mass in g, V is the solution volume in L, and *RE* is the % removal efficiency.

3 Results and discussion

3.3 Effects of parameters

The findings of the XRD analysis of colemanite are given in Bayça [4]. The material consists primarily of colemanite and a small amount of calcite.

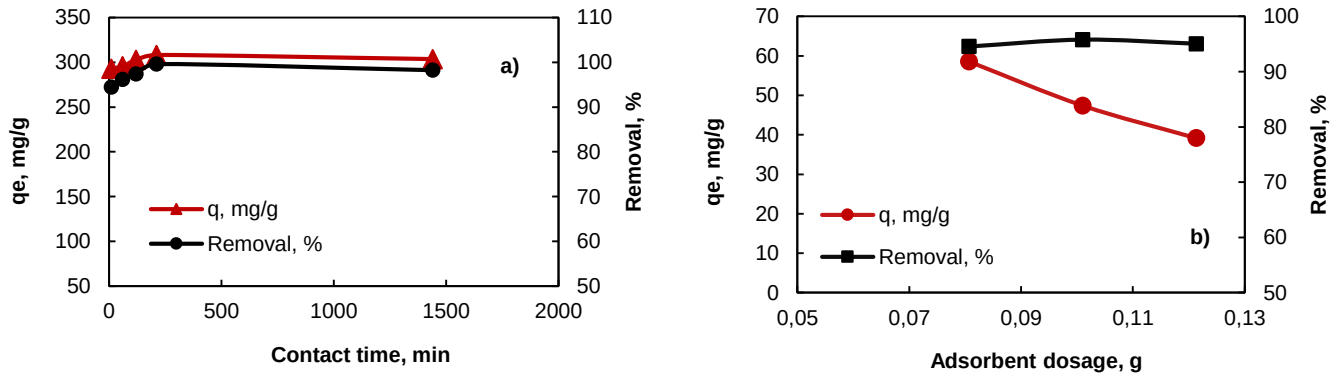

Figure 1. a) Effect of contact time on adsorption capacity and removal efficiency
b) Effect of adsorbent dosage on adsorption capacity and removal efficiency

The chemical analysis of the colemanite XRF (excluding B_2O_3) was peformed. In the XRF analysis, the colemanite included 42.69% B_2O_3, 34.44% CaO, 5.22% SiO_2, and 2.90% MgO.

The effect of contact time on adsorption was investigated, and the results are presented in Figure 1a. In this studies performed to find the optimum contact time, the initial MB concentration was kept fixed at 500 mg/L, the solution pH at 6.28, the stirring speed at 400 rpm, and the adsorbent dosage at 80 mg. While the contact time ranged from 10 to 1440 mg. This Figure shows that both the adsorption capacity (qe, mg/g) and removal efficiency (%) increased with increasing contact time, reaching a maximum value at 1440 min. The removal efficiency of methylene blue adsorbed on colemanite reached 99.62% in 210 minutes.

Figure 1b shows the results, including the effect of adsorbent dosage. In studies conducted to determine the optimal adsorbent dosage, the initial MB concentration was kept constant at 500 mg/L, the pH of the solution at 6.28, the agitation speed at 400 rpm, and the contact time at 60 minutes. While colemanite was used as an adsorbent dosage of between 80 and 120 mg. It was ascertained that as the colemanite dosage was raised, the adsorption capacity decreased, and the removal efficiency slightly increased.

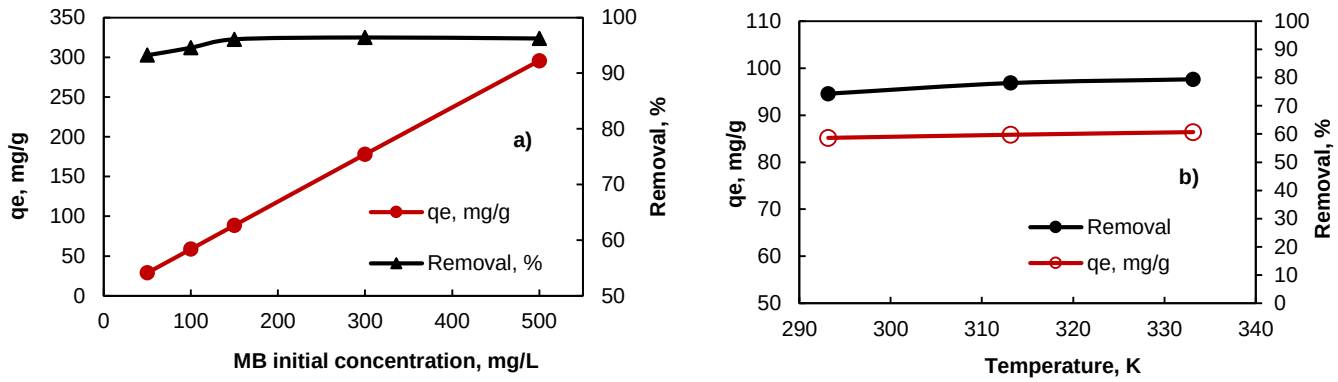

Figure 2. a) Effect of methylene blue initial concentration on adsorption capacity and removal efficiency, **b)** Effect of temperature on adsorption capacity and removal efficiency

A graphical representation of the experimental findings is presented in Figure 2a. Studies conducted to research the influence of initial MB concentration on adsorption were conducted. Five different MB concentrations were also examined at 50, 100, 150, 300, and 500 mg/L. Adsorption capacity and removal efficiency (%) were found to raise as the initial MB concentration raised from 50 mg/L to 500 mg/L. The mass transfer resistance between the solid and aqueous phases decreased with increasing initial MB concentration. Higher concentrations resulted in better adsorption [10,11].

The influence of temperature on MB colemanite was investigated at temperatures of 20, 40, and 60°C (Figure 2b). A small rise in adsorption capacity was found with a rising temperature). However, the small rise in adsorption capacity observed with rising temperature can be attributed to the higher kinetic energy of heated molecules and the reduced viscosity of the solution. There are articles in the literature on the acceleration of adsorption with increasing temperature [12 – 14].

3.2 Adsorption isotherms

Adsorption capacity can be determined experimentally and theoretically. Theoretical adsorption capacity is preferred in literature. Theoretical adsorption capacity is found using adsorption isotherm models. The most commonly used adsorption isotherm models are the Langmuir, Freundlich, and Dubinin-Radushkevich (DR) isotherm models. Bouchelkia et al. [15] and Han et al. [16] adsorption isotherms present information about the system's adsorption mechanism, maximum adsorption capacity, and the surface properties of the adsorbent.

Table 1. Parameters of adsorption isotherm models of methylene blue on colemanite

Isotherms	**Values**
Langmuir	
Q_m (mg/g)	121.95
K_L (L/mg)	0.09
R^2	0.4593
Freundlich	
Q (mg/g)	5.34
1/n	1.94
R^2	0.9119
Dubinin Radushkevich (DR)	
Q_m (mg/g)	425.09
β	4.95
E (kJ/mol)	0.32
R^2	0.9780

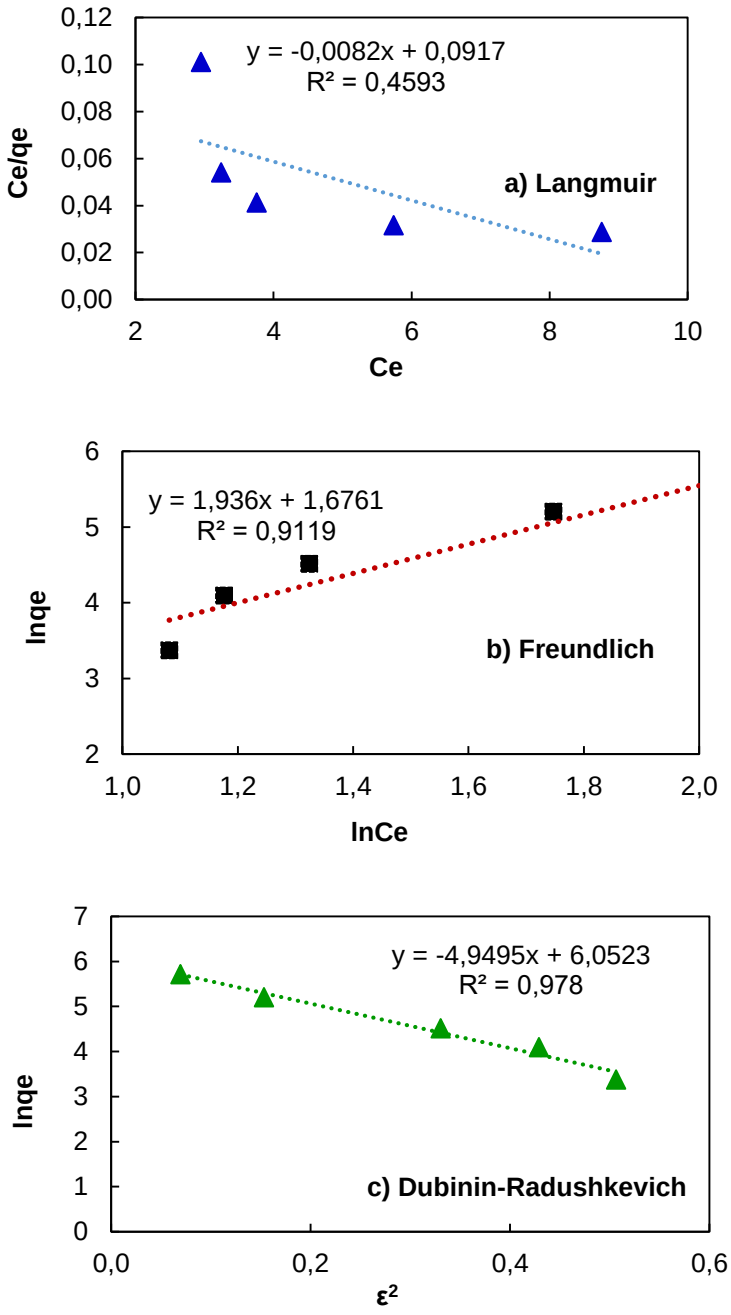

Figure 3. Adsorption isotherm model for adsorption of methylene blue on colemanite **a)** Langmuir, **b)** Freundlich and **c)** Dubinin-Radushkevich

In this work, the values of the isotherm models were found using the equations of the Langmuir, Freundlich and Dubinin-Radushkevich (DR) isotherm models reported in Bayça [4]. The results of the Langmuir, Freundlich, and DR isotherm models are presented in Figure 3 and Table 1. The findings revealed that the correlation coefficient acquired from the DR isotherm was found to be significantly higher than the

correlation coefficients acquired from the Langmuir and Freundlich adsorption isotherms. The adsorption capacity of MB on colemanite was calculated as 425 mg/g using the DR isotherm.

In the literature, it was found that the adsorption capacities varied between 8 and 588 mg/g. In this study, the adsorption capacity of MB on colemanite (425 mg/g) was quite high compared to literature. Table 2 presents the isotherms and adsorption capacities found in the literature for methylene blue using different adsorbents [9,10,14 – 19]. In the literature, it was found that the adsorption capacities varied between 8 and 588 mg/g. In this study, the adsorption capacity of MB on colemanite (425 mg/g) was quite high compared to literature.

Table 2. Adsorption isotherms of methylene blue on different adsorbents

Adsorbent	Adsorption isotherm	Q_m mg/g	References
Neem tree leaf powder	Langmuir	8	[9]
Coconut bunch waste	Langmuir	70	[10]
Rise husk	Langmuir	40	[14]
Activated carbon (Hazelnut shell)	Langmuir	8	[15]
Kaolinite clay	Langmuir	52	[16]
Activated carbon (coal)	Langmuir	588	[17]
Activated carbon (Bamboo)	Langmuir	454	[18]
Montmorillonite clay	Langmuir	289	[19]
Colemanite	Dubinin-Radushkevich	425	Present study

3.3 Adsorption Kinetics

In this study, kinetic calculations were performed using the equations of the pseudo-first-order (PFO) and pseudo-second-order (PSO) kinetic models reported in Bayça [4]. The results on MB adsorption on colemanite were investigated using these two kinetic models. The calculated parameters for the PFO and PSO kinetic models are presented in Table 3. The R^2 values of the PFO kinetic model are very small at each concentration point. Furthermore, the experimental q_e values calculated in this kinetic model are not consistent with the theoretical q_e values, so the PFO kinetic model is not suitable for this study. However, the correlation

coefficients of the PSO kinetic model ($R^2 = 1$) are very high, and the experimental q_e values are very close to theoretical q_e values. The PSO kinetic model was determined to be the most suitable kinetic model for this study.

Table 3. Parameters of adsorption kinetic models of methylene blue adsorption

C_o	qe Experimental	Pseudo First Order			Pseudo Second Order		
mg/L	mg/g	qe mg/g	K_1	R^2	qe mg/g	K_2	R^2
50	29.19	0.987	6.04×10^{-6}	0.9934	29.24	0.0632	1.0000
100	59.95	1.094	-3.47×10^{-8}	0.0279	59.17	0.0092	1.0000
150	91.06	4.770	4.86×10^{-6}	0.9471	90.91	0.0099	1.0000
300	181.86	6.062	1.67×10^{-6}	0.8791	181.82	0.0033	1.0000
500	303.61	10.625	-2.08×10^{-7}	0.4776	303.03	0.0272	1.0000

4 CONCLUSIONS

In this study, it was aimed to remove methylene blue (MB), a cationic dye, from aqueous solutions with high efficiency by using colemanite as adsorbent. Experiments revealed that the adsorption capacity decreased by raising colemanite dosage and increased with the initial methylene blue concentration. The optimum adsorbent dosage and adsorbate concentration were determined as 80 mg and 500 mg/L, respectively. The Dubinin-Radushkevich (DR) model was found to be the most suitable adsorption isotherm, and the maximum adsorption capacity and removal efficiency were calculated as 425.09 mg/g and 99.62% at 20°C. Adsorption kinetics were examined, revealing that methylene blue adsorption had a correlation of $R^2=1$ at all initial concentrations, and the adsorption followed a pseudo-second-order kinetic model. During the adsorption studies, the equilibrium was reached in 1440 minutes. Removing methyleneblue, which causes many health and environmental problems, from wastewater is crucial. Therefore, colemanite can be considered a useful and alternative adsorbent for the adsorption of methylene blue.

REFERENCES

[1] El-Sayed, G. O., Removal of methylene blue and crystal violet from aqueous solutions by palm kernel fiber. Desalination 272, 225–232, 2011.

[2] Yagub, M. T., Sen, T. K., Afroze, S., Ang, H. M., Dye and its removal from aqueous solution by adsorption: a review. Advances in Colloid and Interface Science 209, 172–184, 2014.

[3] Nigam, P., Armour, G., Banat, I. M., Singh, D., Marchant, R., Physical removal of textile dyes from effluents and solid-state fermentation of dye-adsorbed agricultural residues. Bioresource Technology 72, 219 – 226, 2000.

[4] Bayça, F., Effective removal of rhodamine B dyestuff using colemanite as an adsorbent: Isotherm, kinetic, thermodynamic analysis and mechanism. Heliyon 11, e40743, 2025.

[5] Gupta, V. K., Suhas, Application of low-cost adsorbents for dye removal – A review. Journal of Environmental Management 90, 2313–2342, 2009.

[6] Vimonses V., Lei, S., Jin, B., Chow, C. W. K. Saint, C. Kinetic study and equilibrium isotherm analysis of Congo Red adsorption by clay materials. Chemical Engineering Journal 148, 354–364, 2009.

[7] Alshandoudi, L. M., Alkindi, S. R., Alhatmi, T. Y., Hassan, A. F., Synthesis and characterization of nano zinc oxide/zinc chloride–activated carbon composite based on date palm fronds: adsorption of methylene blue. Biomass Conversion and Biorefinery 14, 1719 – 17233, 2024.

[8] Munir, M., Nazar, M. F., Zafar, M. N., Zubair, M., Ashfaq, M., Hosseini-Bandegharaei, A., Ud-Din Khan, S., Ahmad, A., Effective adsorptive removal of methylene blue from water by didodecyldimethylammonium bromide-modified Brown clay. ACS Omega 5, 16711 – 16721, 2020.

[9] Bhattacharyya, K. G., Sharma, A., Kinetics and thermodynamics of Methylene Blue adsorption on Neem (Azadirachta indica) leaf powder. Dyes and Pigments 65, 51 – 59, 2005.

[10] Hameed, B. H., Mahmoud, D. K., Ahmad, A. L., Equilibrium modeling and kinetic studies on the adsorption of basic dye by a low-cost adsorbent: Coconut (Cocos nucifera) bunch waste. Journal of Hazardous Materials 158, 65 – 72, 2008.

[11] Bulut, Y., Aydın, H., A kinetics and thermodynamics study of methylene blue adsorption on wheat shells. Desalination 194, 259–267, 2006.

[12] Hameed, B. H., Salman, J. M., Ahmad, A. L., Adsorption isotherm and kinetic modeling of 2, 4-D pesticide on activated carbon derived from date stones. Journal of Hazardous Materials 163, 121 – 126, 2009.

[13] Li, Z., Wang, G., Zhai, K., He, C., Li, Q., Guo, P., Methylene blue adsorption from aqueous solution by loofah sponge-based porous carbons. Colloids and Surfaces A 538, 28–35, 2018.

[14] Miao, S., Shi, M., Xia, H., Gao, H., Mao, X., Zhang, Y., Adsorption of Congo red and methylene blue from aqueous solution by magnetic cobalt nanoparticles embedded in hierarchical porous carbon prepared via a one-pot approach. Solid State Sciences 128, 106879, 2022.

[15] Bouchelkia, N., Tahraoui, H., Amrane, A., Belkacemi, H., Bollinger, J. C., Bouzaza, A., Zoukel, A., Zhang J., Mouni, L., Jujube stones based highly efficient activated carbon for methylene blue adsorption: Kinetics and isotherms modeling, thermodynamics and mechanism study, optimization via response surface methodology and machine learning approaches. Process Safety and Environmental Protection 170, 513–535, 2023.

[16] Han, R., Zhang, J., Han, P., Wang, Y., Zhao, Z., Tang, M., Study of equilibrium, kinetic and thermodynamic parameters about methylene blue adsorption onto natural zeolite, Chemical Engineering Journal 145, 496–504, 2009.

[14] Yadav SK, Dhakate SR, Singh BP. Carbon nanotube incorporated eucalyptus derived activated carbon-based novel adsorbent for efficient removal of methylene blue and eosin yellow dyes. Bioresource Technology 344, 126231, 2022.

[15] Hasanbarogh, A. F., Ghasemi, N., Ezzatzadeh, E., Equilibrium isotherms studies of methylene blue adsorption by MIL-101 (Cr) modified with zinc oxide nanoparticles. Nashrieh Shimi va Mohandesi Shimi Iran 42, 157 – 175, 2023.

[16] Loutfi, M., Mariouch, R., Mariouch, I., Belfaquir, M., ElYoubi, M. S., Adsorption of methylene blue dye from aqueous solutions onto natural clay: Equilibrium and kinetic studies. Materials Today: Proceedings 72, 3638 – 3643, 2023.

[17] Vadivelan, V., Vasanth Kumar, K., Equilibrium, kinetics, mechanism, and process design for the sorption of methylene blue onto rice husk. Journal of Colloid and Interface Science 286, 90–100, 2005.

[18] Aygun, A., Yenisoy-Karakas, S., Duman, I., Production of granular activated carbon from fruit stones and nutshells and evaluation of their physical, chemical and adsorption properties. Microporous and Mesoporous Materials 66, 189–195, 2003.

[19] Mouni, L., Belkhiri, L., Bollinger, J. C., Bouzaza, A., Assadi, A., Tirri, A., Dahmoune, F., Madani, K., Remini H., Removal of Methylene Blue from aqueous solutions by adsorption on Kaolin: Kinetic and equilibrium studies. Applied Clay Science 153, 38 – 45, 2018.

5th International Natural Science, Engineering and Material Technologies Conference
Sep 18-20, 2025, İğneada-Kırklareli / TÜRKİYE

IMPROVED ENERGY HARVESTING FOR SOLAR PV SYSTEMS UNDER LOW IRRADDIANCE CONDITIONS

N. Tutkun[1], M. Şimşir[2]

[1]*Department of Electrical & Electronics Engineering, Faculty of Engineering, İstanbul Ticaret University, Istanbul, TÜRKİYE*
[2]*Department of Electrical & Electronics Engineering, Faculty of Engineering and Natural Sciences, Karabük University, Karabük, TÜRKİYE*

E-mail: ntutkun@ticaret.edu.tr, msimsir@karabuk.edu.tr

Abstract

A solar photovoltaic (PV) system, widely used in homes, businesses, and utility-scale power plants, converts sunlight directly into electricity by means of solar panels. It accommodates many advantages such as clean energy source, low-cost electricity bills, low maintenance despite few disadvantages like high initial cost, weather and irradiance dependent, cost of energy storage etc. However, it exhibits poor power generation performance at low irradiance due to cloudy or rainy weather, early morning or late evening times, shading (trees, buildings, dirt), dynamic ambient conditions, efficiency constraints and so on particularly in low power applications. Maximum power point tracking (MPPT) is an efficient way to harvest maximum energy possible in which the proportional integral (PI) controller electronically adjusts the duty cycle of the boost converter. It receives measured voltage and current from the solar PV array to find the measured power and shifts operation voltage point to where change in power with respect to voltage is zero. The best MPPT performance requires high tracking efficiency, fast dynamic response, low steady-state oscillations and ease of implementation however conventional MPPT techniques suffer from meeting some of these criteria. In this study, an MPPT model is proposed by estimating open-circuit voltage with minimum error in order to find optimal MPP voltage faster and less oscillation even in low solar irradiances using the cubic spline interpolation (CSI) with piecewise polynomials through a set of data obtained from the manufacturer's data available in MATLAB/Simulink library. The results obtained by using the proposed approach are compared with those found by using the most used conventional MPPT techniques in the built MATLAB/Simulink models. It appears that the proposed CSI method for finding the MPP at varying irradiance in low power PV systems mostly exhibits better performance than the other methods under the reverse operation point perturbation (ROPP) test conditions.

Keywords: Solar PV system, Maximum power point tracking, Cubic spline interpolation, ROPP test.

1. INTRODUCTION

A solar PV system converts sunlight directly into electricity used in homes, businesses, and utility-scale power plants. It is usually composed of solar panels, a dc-dc converter with MPP tracker, charge controller, battery bank (optional), inverter, ac/dc loads, mounting structure, metering and monitoring devices and is broadly divided into grid-tied, off-grid and hybrid systems, providing many advantages such as renewable and clean energy source, low-cost electricity bills, less maintenance, scalable and modular structure and long lifespan etc. However, it has a few disadvantages as high initial cost, weather and irradiance dependent, cost of energy storage. Particularly it exhibits poor performance to yield maximum power available at low irradiances due to cloudy or rainy weather, early morning or late evening times, efficiency constraints, shading caused by trees, buildings, dirt, etc. The MPPT is essential mechanism to extract maximum power available under varying weather and load conditions. The MPPT controller simply monitors voltage and current from the PV system and shifts operation point to where change in the power with respect to voltage is almost zero. It keeps operation voltage at around the MPP by adapting to changes in irradiance and temperature, increasing PV system efficiency up to 40% thus it improves return on investment (ROI). In general, the best MPPT performance requires improving high tracking efficiency, fast dynamic response, low steady-state oscillations and ease of implementation. Numerous researchers have worked on MPPT performance, proposed a limited number of methods improving them from various aspects and some of their investigations are reviewed here.

The MPPT algorithms mostly fail to promptly detect the incremental changes in voltage and current at low irradiances though the optimal operation of MPPT is needed in real-time applications. In order to overcome this drawback, an improved hill-climbing MPPT algorithm with two distinct perturbation step-sizes are put forward to sense very small changes in voltage and current due to perturbation and it is reported that some improvements are made [1]. In another study, a robust modified perturb and observe (P&O) approach is proposed to increase the tracking efficiency at low irradiances and the obtained results are found to be meaningful [2]. A new approach to improve the incremental conductance (IC) algorithm with variable step size is proposed to extract maximum power in a solar PV system under varying irradiances and it is expressed that steady-state oscillation is reduced, and fast-tracking accuracy is increased [3]. In another study, a hybrid MPPT technique based on the combination of the Genetic Algorithm (GA) and the fractional open-circuit voltage (FOCV) is proposed to reduce convergence time to the MPP [4]. In this study, MATLAB/Simulink is used to test the robustness of the proposed technique under varying irradiances, and the results are compared to those obtained from using the P&O, the IC, and the other hybrid MPPT techniques. In another study, the

grey wolf optimizer (GWO) and the particle swarm optimization (PSO) optimization methods are employed to extract maximum power from the PV system through the MPPT and the obtained results are compared with the results obtained from using the P&O and IC algorithms and the findings indicate that the proposed approach worked well for the problem at hand [5]. Another study is suggested for maximum power extraction from a PV array with the MPPT using fuzzy gain scheduling with the proportional-integral-derivative (PID) controller and the preliminary outcomes show better performance on fast and accurate tracking compared to other methods [6]. A novel hybrid MPPT is introduced in another investigation to capture the maximum power from solar PV arrays under varying irradiance and temperature, and the designed approach exhibits faster tracking response and higher efficiency compared to the conventional methods [7]. A novel P&O algorithm with variable step size is suggested reducing steady-state oscillation during MPPT process to acceptable level and this approach exhibits improved results with respect to similar methods [8]. A new adaptive controller is presented to improve the performance of MPPT that efficiently manages uncertainties and disruptions in the PV system, and the results are found be encouraging and meaningful [9]. Another P&O algorithm is developed to balance the dynamic response and the steady-state oscillation in MPPT mechanism using the FOCV technique and the it shows a considerable improvement on the PV system under investigation [10]. It should be noted that although there are numerous studies on this subject, only a limited number of up-to-date studies are included here due to space constraints.

In this study, an improved MPPT approach based on CSI principle and manufacturer data is proposed for the solar PV system is proposed and is tested by the MATLAB/Simulink models under dynamic irradiance conditions. The application of the suggested approach to the problem at hand and the results found are explained in detail in the following section.

2. MATERIAL AND METHODS

In the proposed approach as shown in Figure 1, the ambient temperature is assumed to remain constant at 25°C, and the amount of solar radiation in the environment is measured using a pyranometer. Based on this measured solar radiation, the developed model computes the reference voltage and the difference from the measured voltage at the PV output is determined. This difference so-called error is routed to the PI controller, then pulse width modulation (PWM) signal to control the switching device is generated by comparing the signal obtained from the controller output with the triangular wave signal at the switching frequency of 20 kHz. The error reduces to an acceptable level by adjusting the electronic switch in the boost converter and this results in maximum power transfer from the PV system under the current conditions. Note that the PV output

voltage and the solar radiation are measured in this investigation but in traditional methods, the PV output voltage and output current are only measured. The key difference here is that in traditional methods the reference voltage is found by perturbing voltage with constant or variable step size, while in the proposed method, the reference voltage is calculated directly from the model. Therefore, the initial time until the MPP is reached, that is the response time, is shorter in the proposed method. The gain coefficients for the PI controller used were obtained using a GA optimization technique and were found to be relatively unchanged at various solar radiations. Therefore, the same value of $K_p = 0.5$ and $K_i = 100$ were used in the model implementation. In this study, Solartech STR215 PV array is employed and the manufacturer's data acquired at the standard test condition (STC) is given in Table 1. Besides the derived open-circuit voltage and maximum power point voltage using MATLAB/Simulink I-V curve models are shown in Table 2.

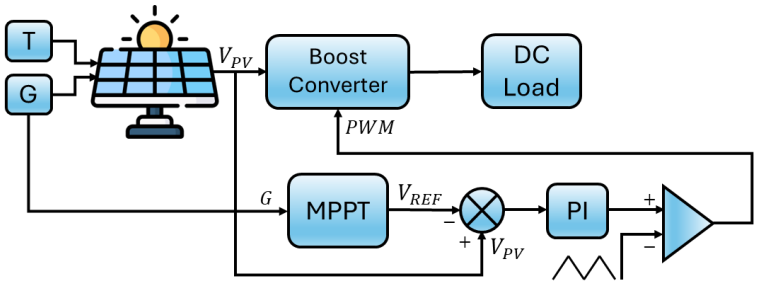

Figure 1. The typical solar PV system with the MPPT.

Table 1 The Solartech STR215 data at the STC

Parameter	Value
Short circuit current	7.73 A
Open circuit voltage	36.00 V
Voltage at MPP	28.70 V
Current at MPP	7.49 A
Power at and MPP	215 W
Fill factor	77.2%
Efficiency	14.3%

Table 2 V_{oc} and V_{mmp} at various irradiances at 25 °C.

G(kW/m^2)	V_{mmp} (V)	V_{oc} (V)
100	27.4458	32.2861
200	28.2510	33.4002
400	28.7808	34.5153
500	28.8662	37.8763
600	28.8792	35.1592
800	28.8392	35.6350
1000	28.7000	36.000

The model is based on piecewise cubic polynomials spline interpolation specific to each data range available in the MATLAB/Simulink environment. To make smooth transitions between adjacent points, the function continuity was ensured for the first and second derivatives. It should be emphasized that, due to the lack of

sufficient data, the least squares method was not preferred in building this model. The mathematical formulation of the model can be defined as

Given a set of $n+1$ data points (x_0, y_0), (x_1, y_1),...,(x_n, y_n), cubic polynomials $S_i(x)$ in each interval $[x_i, x_{i+1}]$ can be expressed as

$$S_i(x) = a_i + b_i(x - x_i) + c_i(x - x_i)^2 + d_i(x - x_i)^3, \qquad x \in [x_i,\ x_{i+1}] \qquad (1)$$

The coefficients a_i, b_i, c_i, d_i are determined by the following conditions:

$S_i(x_i) = y_i$ and $S_i(x_{i+1}) = y_{i+1}$

$S_i'(x_{i+1}) = S_{i+1}'(x_{i+1})$

$S_i''(x_{i+1}) = S_{i+1}''(x_{i+1})$

$S''(x_0) = 0$ and $S''(x_{n+1}) = 0$.

It is important to note that in a simulation-based application, model construction can be accomplished using MATLAB built-in functions for spline interpolation. In a real-world application, the model can be implemented by using an appropriate microprocessor architecture.

3. RESULTS AND DISCUSSION

The designed Simulink model run in the MATLAB R2023b environment on a computer with a 13th Generation Intel(R) Core (TM) i9-2.60 GHz processor, and simulation results are shown in Figs. 3-6. The simulation results obtained from using the designed model are based on the three scenarios and were compared with those found from the P&O, IC and FOCV techniques at 25°C.

In the first scenario, the irradiance gradually varied from 200 W/m^2 to 1000 W/m^2 and at each interval irradiance is unchanged. Under varying irradiances, the proposed approach was tested together with P&O, IC and FOCV methods so-called popular conventional techniques. For the conventional methods the standard Simulink test model as simply shown in Fig. 1 was employed. However, for the proposed model the load side of boost converter was modified to change output impedance at the constant output voltage. That is, a resistor was connected parallel in with the load resistor, and another switching element was connected in series with it. This switching element was controlled by a PI controller to maintain the output voltage at the desired value. The developed model as shown in Fig. 2 was applied to extract maximum power from the PV system in the

MATLAB/Simulink environment. The results were compared with those found in the same model using the P&O, IC, and FOCV techniques and the comparison results are illustrated in Figs 3-6. As seen in Fig. 3, the proposed approach exhibits a better performance at low irradiance compared with the results obtained by the other techniques. This may be explained by the output impedance of the boost converter that is very influential on power delivery to the load side from the PV array at low irradiances. One way to extract much more power from the PV array at low irradiance is required to make its output current larger. This requires controlling the switching element in the boost converter and adjusting the output resistance to the appropriate value at each irradiance. Doing so allows for higher output current at low irradiance ranging from 100 W/m^2 to 400 W/m^2, which in turn allows for the greater power output possible. It appears that this technique is applied more effectively with the proposed method on a simulation basis compared to other methods.

However, there are particular differences in applying these methods to a real-time system. For instance, accurate measurements of the output voltage and current at the PV array in short intervals for the P&O and IC methods are the main procedure to obtain maximum power extraction. But the FOCV method differs from the P&O and IC methods in that it requires a pilot system in addition to the main system to reach the maximum power point so that it is a slightly more complex system than the P&O and IC methods.

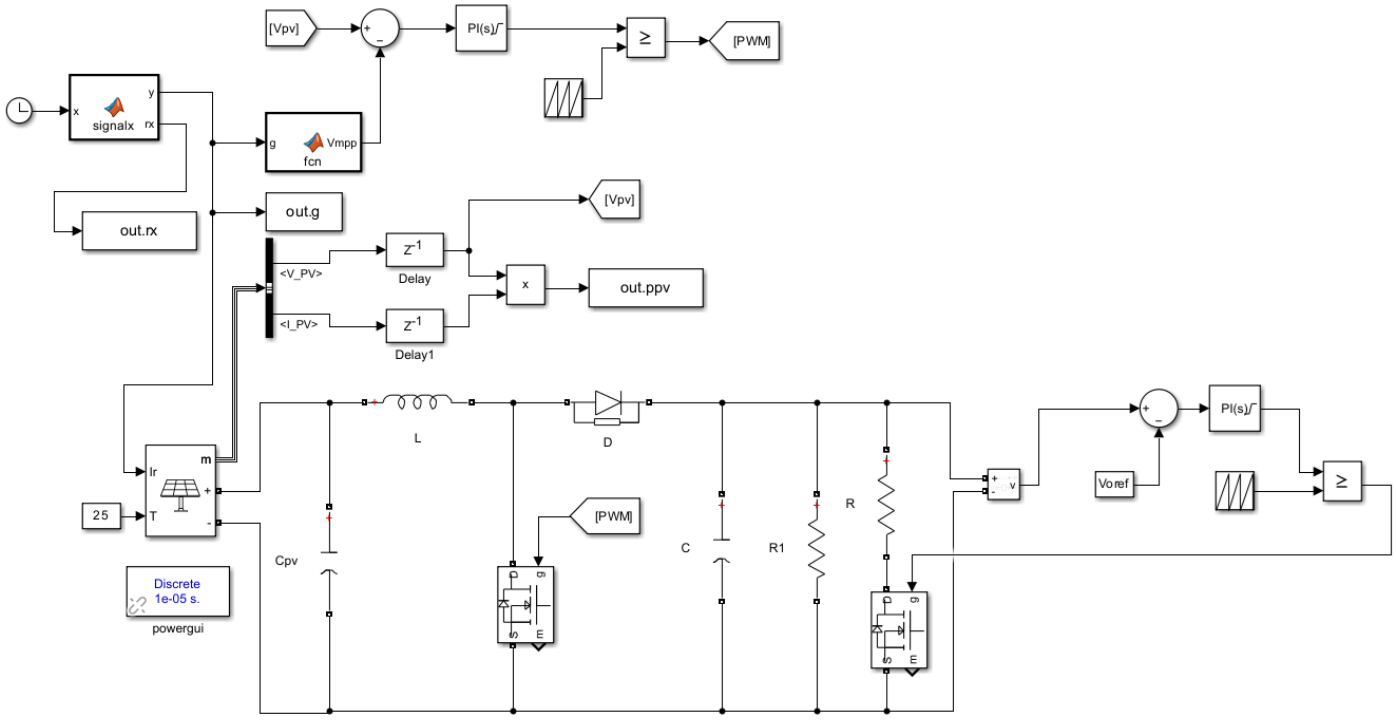

Figure 2. The MATLAB/Simulink model for the proposed approach.

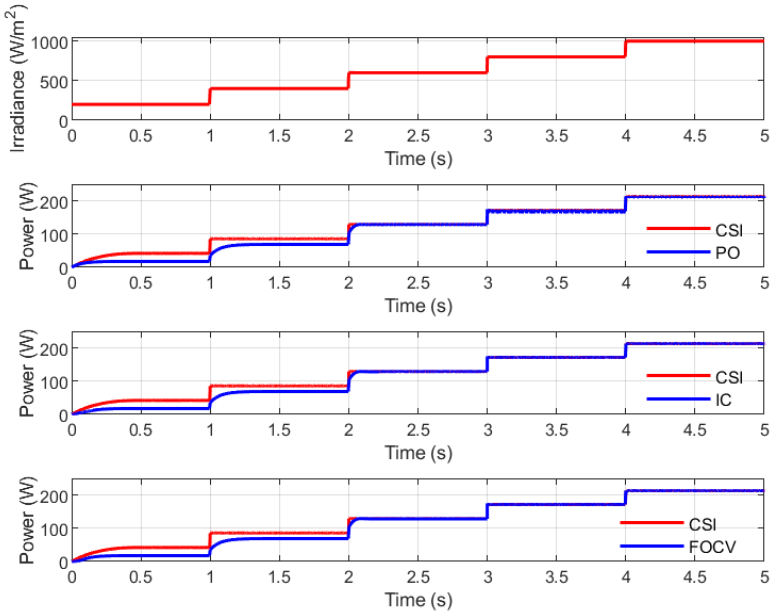

Figure 3. Comparison of the proposed approach with all three methods under increasing irradiances.

In the second scenario, the irradiance changed smoothly and steadily from 1000 W/m^2 to 200 W/m^2. The responses of the proposed approach and the conventional method to this variation is simulated, and the simulation results are presented in Figure 4. As seen from Figure 4, the results by the proposed method and the other methods have almost similar trends, except for the range from 400 W/m^2 to 100 W/m^2. In the first scenario, as the irradiance varies steadily and smoothly, conventional methods show similar responses except for the proposed method at low irradiances. Consequently, it appears that varying irradiance, whether increasing or decreasing, in the MATLAB/Simulink environment produces mostly similar results, even though the applied methods use different algorithms, regardless of some differences. In both scenarios, the use of a PI controller minimizes error throughout the process, and it makes PV output voltage almost equal to the voltage at MPP. Comparing the simulation results of the proposed approach with the theoretical results reveals that the conventional methods exhibit poor performance at low irradiance except for the proposed approach as shown in Figure 5, but there is a relative performance improvement as irradiance begins to increase. A similar case is encountered in almost all MPPT techniques known in the literature. It should be emphasized that there are of course considerable differences between the responses in simulation models and real-time systems as expected but this investigation is beyond the real-time implementation.

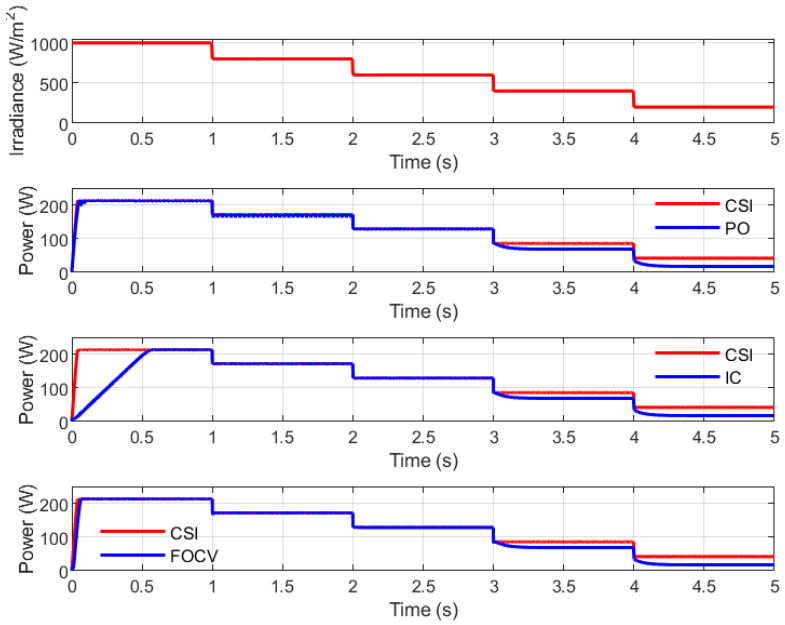

Figure 4. Comparison of the proposed approach with all three methods under decreasing irradiances.

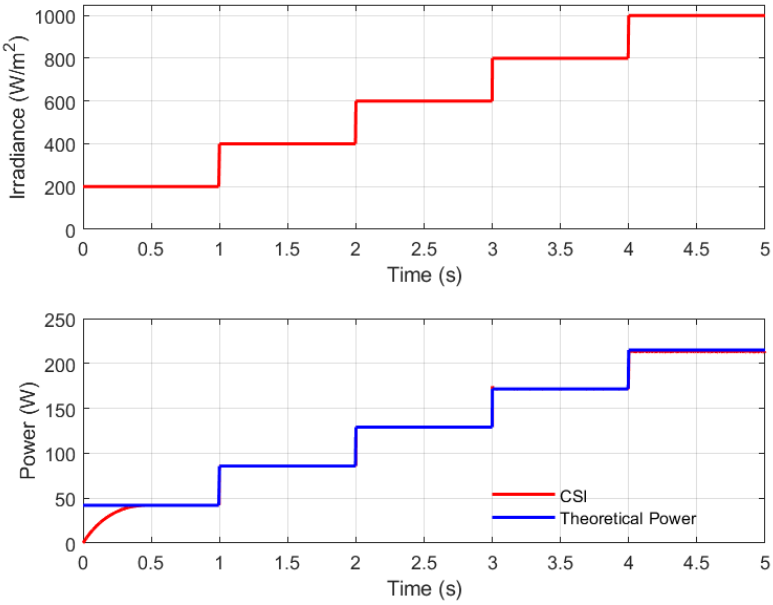

Figure 5. Comparison of the proposed approach with theoretical results under increasing irradiances.

In the third scenario, the proposed method was also tested under more dynamically changing irradiances, known as the ROPP test. The results were compared with those of conventional methods are shown in Figure 6. As seen from Figure 6, the proposed method is found to be more efficient than P&O and IC methods in finding the MPP at dynamically changing irradiance. When the results obtained by the proposed method were compared with those obtained from conventional methods, it seems that they are highly similar to those obtained from the FOCV method but are different from the results obtained by the P&O and IC methods at

low irradiances. Furthermore, the proposed method under dynamic irradiance conditions at different temperatures is tested and the results are shown in Figure 6. As depicted in Figure 6, the extracted power decreases at high temperatures and increases at low temperatures as expected.

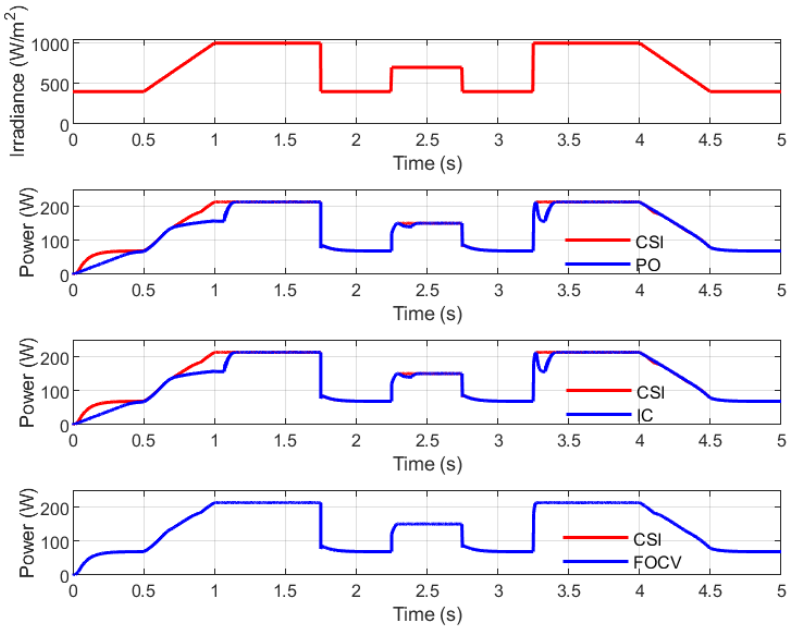

Figure 5. Comparison of the proposed approach with theoretical results under increasing irradiances.

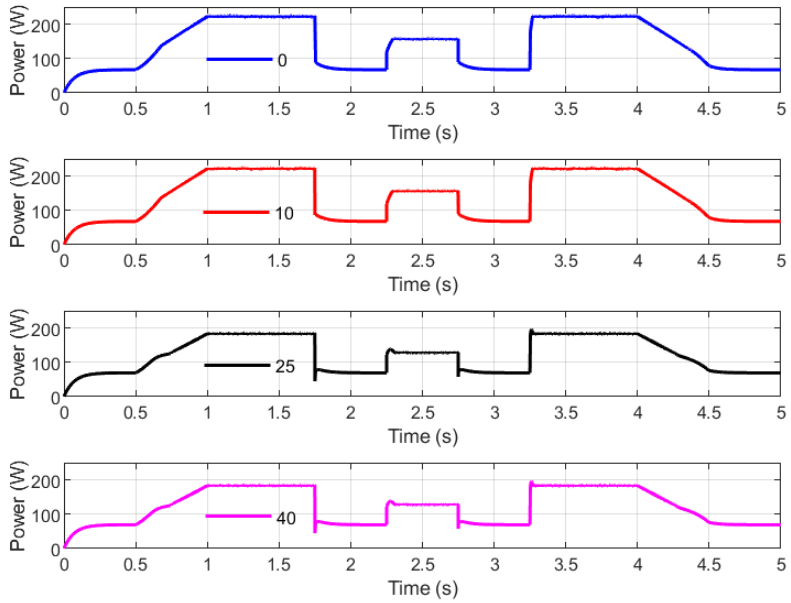

Figure 6. ROPP performance test of the proposed method at different temperatures.

In general, the proposed method appears to have better performance than conventional methods. When the proposed method is applied to a real-time system, it is believed that it can exhibit the same performance with

less measurements since measuring only the irradiance in the environment is sufficient. It should be emphasized that this study involves a simulation-based implementation of the proposed method, its operation performance in a real-time PV array system is beyond this investigation. However, as a continuation of this work, the proposed method is to be tested on, a low-power real-time system in the future work.

4. CONCLUSION

The proposed method exhibits better performance than the P&O, IC, and FOCV methods according to the three scenarios in particular at low irradiances. Likewise, it produces higher tracking speed and less oscillation compared to those produced by the P&O, IC, and FOCV methods due to a smaller number of measurements. Furthermore, it yields reasonable responses at various temperatures under ROPP test in terms of maximum energy harvesting, high tracking efficiency and less oscillation.

ACKNOWLEDGMENTS

We would like to express our gratitude to Istanbul Ticaret University and its Board of Trustees for their financial support to present this study at the NEM 2025 Conference.

REFERENCES

[1] Jately, V. et al, Experimental Analysis of hill-climbing MPPT algorithms under low irradiance levels, Renewable and Sustainable Energy Reviews, vol. 150, 111467, 2021.

[2] Ismail, A. et al., Improved P&O MPPT algorithm with efficient open-circuit voltage estimation for two-stage grid-integrated PV system under realistic solar radiation, International Journal of Electrical Power & Energy Systems, vol. 137, 107805, 2022.

[3] Hebchi, M., Kouzou, A. and Choucha, A., Improved incremental conductance algorithm for MPPT in photovoltaic system, 18th International Multi-Conference on Systems, Signals & Devices, Monastir, Tunisia, 1271-1278, 2021.

[4] Hassan, A., Bass, O. and Masoum, M., An improved genetic algorithm based fractional open circuit voltage MPPT for solar PV systems, Energy Reports, vol. 9, 1535-1548, 2023.

[5] Águila-León, J. et al., Optimizing photovoltaic systems: A meta-optimization approach with GWO-Enhanced PSO algorithm for improving MPPT controllers, Renewable Energy, vol. 230, 120892, 2024.

[6] Alaas, Z. et al, Analysis and enhancement of MPPT technique to increase accuracy and speed in photovoltaic systems under different conditions, Optik, vol. 289, 171208, 2023.

[7] Alshareef, M. J., An enhanced fractional open circuit voltage MPPT method for rapid and precise MPP tracking in standalone photovoltaic systems, in IEEE Access, vol. 13, 34115-34131, 2025.

[8] Saberi, A. et al., An improved P&O based MPPT for PV systems with reduced steady-state oscillation, International Journal of Energy Research, vol. 2023, Issue 1, 4694583, 2023.

[9] Manna, S. et al, Design and implementation of a new adaptive MPPT controller for solar PV systems, Energy Reports, vol. 9, 1818-1829, 2023.

[10] Harrison, A. et al., An enhanced P&O MPPT algorithm for PV systems with fast dynamic and steady-state response under real irradiance and temperature conditions, International Journal of Photoenergy, vol. 2022, Issue 1, 6009632, 2022.

HIDDEN HAZARDS: IMPURITIES IN TEXTILE DYES AND AUXILIARIES, THEIR IMPACT ON HUMAN AND ENVIRONMENTAL HEALTH

A Screening-Based Risk Assessment Approach for Safer Chemical Management in the Textile Industry

B. Meltem, Y. Taner

Department of Environmental Engineering, Faculty of Engineering, Bursa Uludağ University, Bursa, TÜRKİYE

E-mail: 512104006@ogr.uludag.edu.tr

The presence of unintentional impurities in textile chemicals and dyes originating from raw materials or synthesis pathways poses significant risks for both human and environmental health, resulting challenges for sustainable product stewardship. This study focuses on commonly overlooked trace-level impurities found in dyes, auxiliaries and finishing agents used in textile production. Analytical methods such as GC-MS and HPLC were employed to identify trace-level contaminants across representative samples from industry sources.

In addition to evaluating potential health effects through toxicological and ecotoxicological approaches, the presentation highlights how these findings align with expectations under frameworks such as ZDHC (Zero Discharge of Hazardous Chemicals), AFIRM RSL (Apparel and Footwear International RSL Management) and other brand or regulatory requirements. By combining scientific evidence with field experience, this study aims to promote proactive risk management, encourage safer formulation strategies and advocate traceability within chemical supply chains to be able to support human health, environmental protection and sustainable chemical use in the textile industry.

Keywords: Textile chemicals, dye impurities, human health, environmental risk, safer chemicals

1. INTRODUCTION

Behind the vibrant colors and functional finishes of textiles lies a complex chemical reality — one that often goes unnoticed. Impurities in textile dyes and auxiliaries, such as heavy metals, formaldehyde derivatives, aromatic amines and other unintended by-products, pose significant risks to both human health and the environment. While reactive dyes, in particular, are preferred due to their ease of dyeing and stability, dye groups that vary depending on the fiber type are also widely used. These dyes can cause both toxicological effects upon skin contact with the fiber and serious environmental problems when wastewater containing these dyes is discharged into the environment.

This study aims to uncover these hidden hazards, tracing their origins, pathways of exposure and long-term consequences. We will examine how these substances persist in supply chains, challenge regulatory frameworks and demand more transparent, sustainable solutions.

2. MATERIAL AND METHODS

Dyes Used in Textile Industry

Dyes are generally small molecules composed of two main components: a chromophore, which imparts color and a functional group, which binds the dye to the fibre. The adsorption of the dye onto the fibre varies depending on the fibre and the type of dye. Literature contains hundreds of types of dyes classified by their chemical structure or the type of fiber to which they are applied. Classifications based on their chemical structure include azo dyes, anthraquinone dyes, indigoid dyes, metal complex dyes, polymethine dyes, sulfur dyes, arylcarbonium dyes, phthalocyanine dyes and nitro dyes. Classifications based on dyeing properties include reactive, disperse, direct, vat, acidic (anionic), basic (cationic) dyes and optical brighteners [2].

Consequently, this chemical diversity poses numerous risks to both human and environmental health. It also has significant negative impacts on wastewater treatment systems.

Hazardous Risk Parameters in Dyes and Their Toxicity

Table 1. Possible hazardous risk parameters in dyes [2]

Dyes	Fiber	Risk Parameters					
		Arylamines	Chlorinated Phenols	Chlorinated Benzenes & Toluenes	Polycyclic Aromatic Hydrocarbons (PAHs)	Heavy Metals	Alkyl Phenols (AP/APEO)
Reactive	Cotton	X				X	
Disperse	Polyester	X	X	X	X		X
Pigment	Cotton/Pes	X	X		X	X	X
Acid	Polyamide	X	X	X		X	
Basic	Acrylic	X					

Azo dyes contain one or more nitrogen-nitrogen double bonds called azo groups in their chemical structure. Under reductive conditions using sodium dithionite these azo groups can be cleaved to form 2 amines, which are usually arylamines [8]. Azo dye removal, which occurs through the cleavage of azo bonds in dyes, leads to the formation of aromatic amines and some aromatic amines are known to be mutagenic or carcinogenic. In mammals, the metabolic activity (removal) of azo dyes occurs primarily through bacterial activity in the anaerobic portion of the digestive tract. Various other organs, particularly the liver and kidneys, are capable of removing azo dyes [2].

Aromatic amines (arylamines) released after azo dye removal in the intestinal tract are adsorbed by the intestines and excreted in the urine. The toxic danger of aromatic amines is cancer, particularly bladder cancer. The carcinogenic mechanism of azo dyes stems from the formation of acyloxy through N-hydroxylation and N-acetylation of aromatic amines formed by O-acyloxy. These acyloxy amines can transform into nitremium and carbonium, which bind to DNA and RNA structures and can lead to mutation and tumor formation [2].

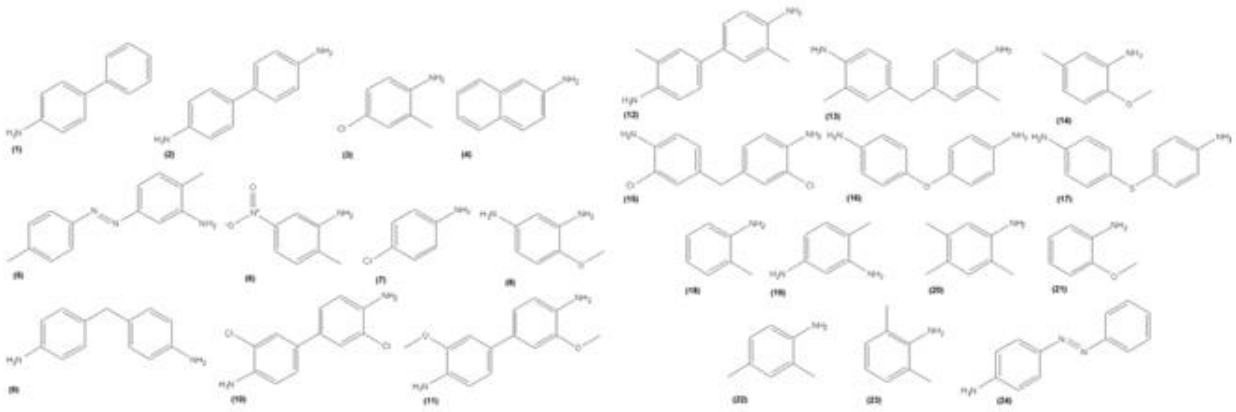

Figure 1. 24 different types of arylamines that can be found in dyes in traces amounts as impurity [5].

Prolonged exposure to **chlorinated phenols** above certain levels can cause cancer. Above certain exposure levels, they are very toxic through inhalation or skin contact. Chlorinated phenols are known to be harmful toxic substances because they readily penetrate skin and epithelium, causing damage and necrosis. Furthermore, workers involved in the production of phenoxy herbicides and chlorinated phenols are known to frequently suffer from heart disease, asthma, lymphoma, lung cancer, and sarcoma [3]. One of the greatest concerns regarding environmental exposure to chlorinated phenols is their potential to contaminate aquatic ecosystems (groundwater and surface water), posing a significant risk to humans and other organisms associated with the aquatic ecosystem's food chain. This situation may be exacerbated by the fact that

chlorinated phenols can maintain high toxicity levels (unchanged) in the environment for extended periods of time, becoming pollutants [6].

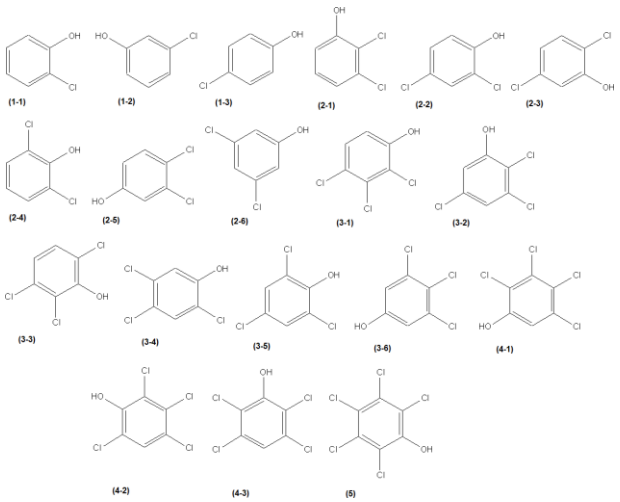

Figure 2. Chemical structures of several kinds of Chlorinated Phenols [5]

Chlorobenzenes and toluenes can affect the liver, thyroid, and CNS. The hazardous properties depend on the type of chlorobenzene or chlorotoluenes. Exposure to chlorobenzenes may cause the development of different types of cancer. Hexachlorobenzene (HCB), the most toxic and persistent chemical of this group, is also a hormone disruptor. The International Agency for Research on Cancer (IARC) classified hexachlorobenzene as "possibly carcinogenic to humans" (Group 2B). Chlorobenzenes potentially cause anesthetic effects and liver, kidney and central nervous system damage. Some chlorobenzenes are toxic by inhalation or skin contact. Chlorobenzenes are persistent and bioaccumulative in the environment. Some chlorobenzenes and chlorotoluenes can be very toxic to aquatic organisms and may cause long-term adverse effects in the aquatic environment. Chlorobenzenes are volatile organic compounds (VOC) [4].

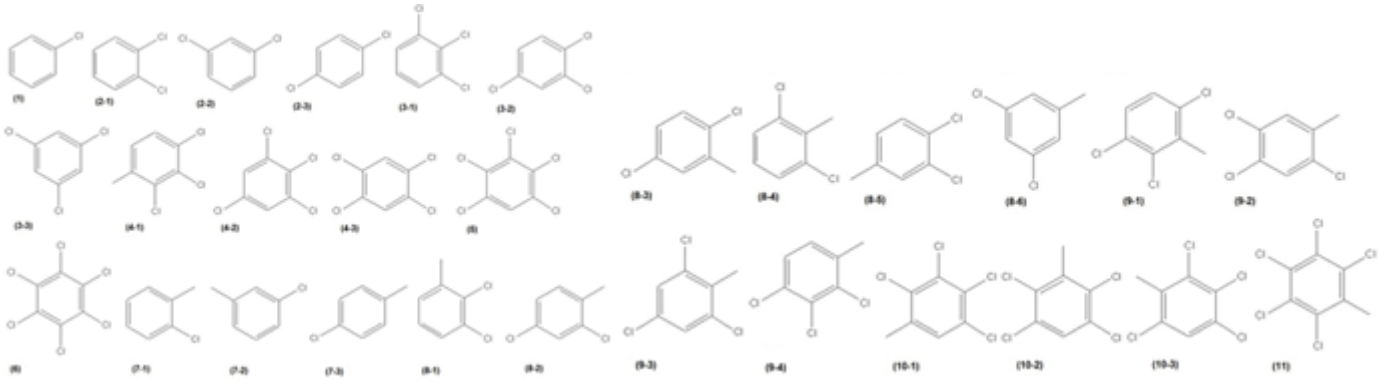

Figure 3. Chemical structures of several kinds of Chlorinated Benzenes and Toluenes [5]

Many **PAHs** have toxic, mutagenic and/or carcinogenic properties. PAHs are highly lipid soluble and thus readily absorbed from the gastrointestinal tract of mammals. They are rapidly distributed in a wide variety of tissues with a marked tendency for localisation in body fat. PAHs have toxic effects on organisms through various actions. 17 PAHs have been identified as being of greatest concern regarding potential exposure and adverse health effects on humans. The International Agency for Research on Cancer classifies some PAHs as known, possible or carcinogenic to humans. Among those PAHs, the substance benzo(a)pyrene is definitely a known carcinogenic for humans. Some PAHs can be very toxic to aquatic organisms and, above certain exposure levels, may cause long-term adverse effects in the aquatic environment [7].

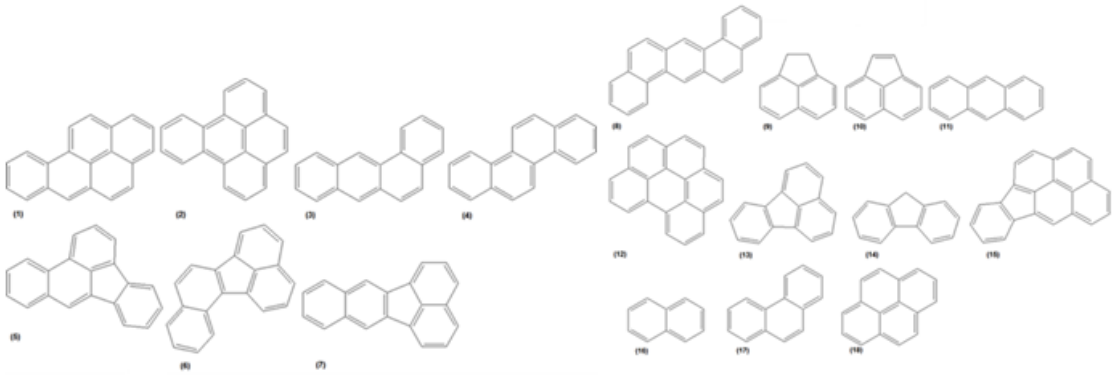

Figure 4. Chemical structures of several kinds of PAHs [5]

Heavy metals can produce side effects on soil, on water, on air, but also on plants, animals and humans. In soil, high levels of heavy metals can produce alteration of soil quality through modification of pH, color, porosity and natural composition, but also low crop production, loss of many types of normal flora and habitat. Their accumulation into the water imposes serious problems on humans and ecosystems, due to decreasing drinking water quality and purity, decreasing water supplies for all living organisms. In plants, they can produce damage of roots or leaves, interfere in important biochemical processes, such as photosynthesis, alteration of minerals absorption, damage of chlorophyll, reduce the growth and development of the roots, which leading to reduction pf overall growth of the plant. Heavy metals become toxic when they are not metabolized by the body and accumulate in organs and soft tissues. They reach the human body by ingesting contaminated water or food, inhalation of absorption through the skin. Among the pathways, ingestion in the common route that helps the heavy metals to enter the animal bodies. The effect of these metals can be inhibitory, stimulatory and toxic for some biochemical processes, being able to produce various health problems on nervous system (Alzheimer, Parkinsoma, depression, dementia), on bone system (bone mineralization) and on reproductive system. Also, can produce DNA damage, RNA affection, or cancer of lungs, skin, bladder. Their toxicity depends on the dose of exposure, time of exposure, pollutant concentration,

organism which are exposed to it, nature and oxidation state of the metal. The toxicity of heavy metals in animals is manifested through decreased body weight, kidney damage, liver affections, shortened life span, increased oxidative stress, modifications of cells composition, DNA damage. In humans they can produce kidney damage, liver affections, pulmonary effects and several types of cancer [9].

Studies have indicated that **APEO** metabolites are more toxic than their parent substances and have the ability to mimic natural hormones by interacting with the estrogen receptor. Levels of these metabolites in the media may exceed the threshold required to induce endocrine disruption in natural metabolism. These findings have raised public concern about their impact on the environment and human health [11].

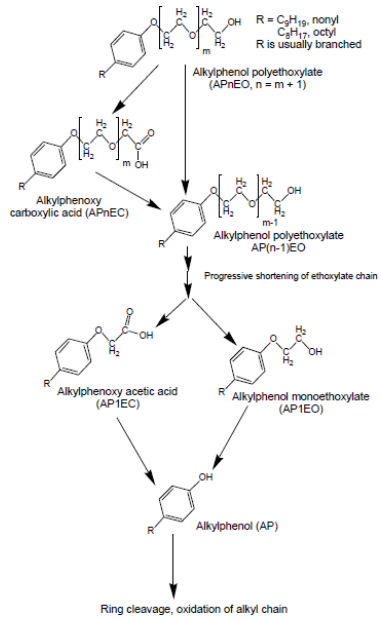

Figure 5. Microbial metabolism of Alkyl Phenol Ethoxylates [10]

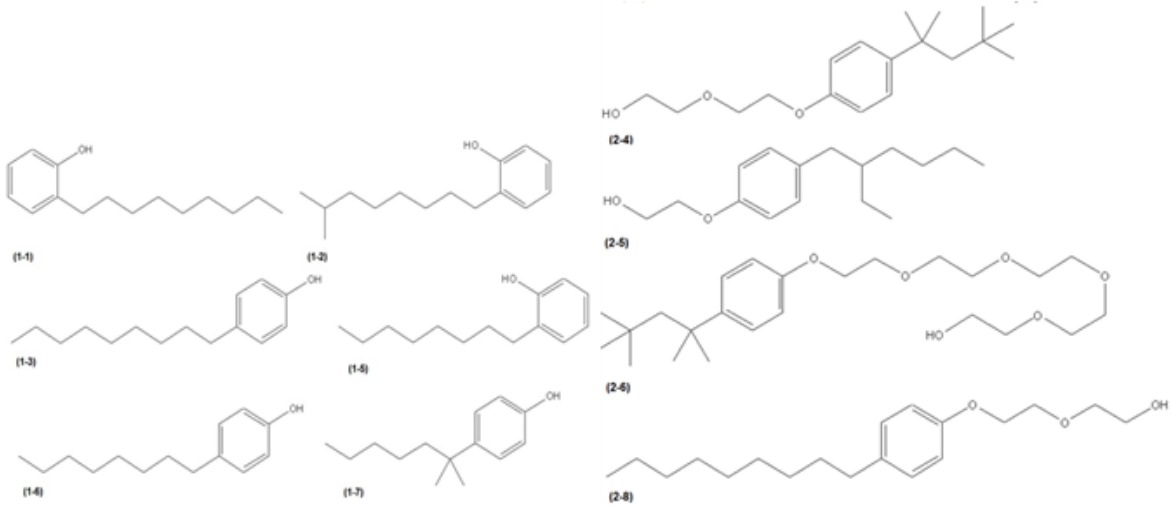

Figure 6. Chemical structures of alkylphenols (APs) and alkylphenol ethoxylates (APEOs) [5].

Zero Discharge of Hazardous Chemicals (ZDHC)

The Zero Discharge of Hazardous Chemicals (ZDHC) Program is a collaboration of brands, value chain affiliates and subsidiaries dedicated to eliminating hazardous chemicals from the textile and footwear value chain. The program aims to reduce and eliminate the use of hazardous chemicals used in the textile, footwear, and leather industries that pose a threat to the environment and human health. This program is managed by member companies that have signed the ZDHC compliance commitment [12].

In 2011, six textile brands established the ZDHC, acting as catalysts to prevent the generation of hazardous chemical waste throughout the product lifecycle of textile and footwear products and to foster positive change. Numerous chemicals are used in the textile and footwear industry. Some chemicals can be harmful to the environment, aquatic life and reproduction. For this reason, chemical limits have long been set by legal regulations or industry standards. However, chemical contamination and residues persist. Therefore, the ZDHC is guiding the industry toward zero hazardous waste with a timeline of goals. There is a need to improve and consolidate chemical management systems across the supply chain [12].

Chemicals Restricted Under ZDHC

1. Alkylphenol (AP) and Alkylphenol Ethoxylates (APEO), all isomers
2. Chlorinated benzenes and toluenes
3. Chlorinated phenols
4. Dyestuffs
   4.1 Azo dyes (with restricted amine release) /Arylamines
   4.2 Navy Blue Colorant
   4.3 Carcinogenic dyes or dyes of equivalent risk
   4.4 Sensitizing disperse dyes
5. Flame retardants
6. Glycols
7. Halogenated solvents
8. Organotin compounds
9. Perfluorinated and polyfluorinated chemicals (PFCs)
10. Phthalates (including ortho esters of phthalic acid and ortho esters of phthalic acid)
11. Polycyclic aromatic hydrocarbons (PAHs)
12. Volatile organic compounds (VOCs)
13. Heavy Metals
14. Antimicrobials and biocides
15. Chlorinated paraffins
16. UV absorbers
17. Other/miscellaneous chemicals

Table 2. Restricted limits of hazardous parameters [1,12,13]

Parameter	**Formulation Limit of ZDHC [1]**	**Wastewater Limit of ZDHC [12]**	**AFIRM RSL (Consumer limits) [13]**
Arylamines	150 ppm (each substance)	0,1 µg/l	20 mg/kg (each substance)
Chlorinated Phenols	MonoCPs sum: 50 mg/kg DiCPs sum: 50 mg/kg TriCPs sum: 50 mg/kg TeCPs sum: 15 mg/kg PCP: 5 mg/kg	0,5 µg/l	TriCPs sum: 0,5 mg/kg TeCPs sum: 0,5 mg/kg PCP: 0,5 mg/kg (each substance)
Chlorinated Benzenes & Toluenes	1,2-Dichlorobenzene: 500 mg/kg Other isomers of mono-, di-, tri-, tetra-, penta- and hexa-Chlorobenzene and mono-, di-, tri-, tetra and Pentachlorotoluene Sum: 200 mg/kg Tetrachlorotoluene and Trichlorotoluene 10 mg/kg each	0,2 µg/l	1,2-Diklorobenzen: 10 ppm Sum of all others: 1 mg/kg
PAHs	Benzo[a]pyrene (BaP): 20 mg/kg Other PAHs sum: 200 mg/kg	1 µg/l	1 mg/kg (each substance) Sum: 10 mg/kg
Heavy metals	Antimony (Sb): 50 mg/kg; Arsenic (As): 50 mg/kg; Barium (Ba): 100 mg/kg; Cadmium (Cd): 20 mg/kg; Chromium (Cr): 100 mg/kg; Chromium (VI): 10 mg/kg; Cobalt (Co): 500 mg/kg; Copper (Cu): 250 mg/kg; Lead (Pb): 100 mg/kg; Mercury (Hg): 4 mg/kg; Nickel (Ni): 250 mg/kg; Selenium (Se): 20 mg/kg; Silver (Ag): 100 mg/kg; Tin (Sn): 250 mg/kg	Antimony (Sb): 0,1 mg/l; Chromium (VI): 0,05 mg/l; Arsenic: 0,05 mg/l; Chromium, total: 0,2 mg/l; Cobalt: 0,05 mg/l; Cadmium: 0,1 mg/l; Copper: 1 mg/l; Lead: 0,1 mg/l; Nickel: 0,2 mg/l; Silver: 0,1 mg/l; Zinc: 5mg/l; Mercury: 0,01 mg/l	Antimony (Sb): 30 mg/kg; Arsenic (As): 0,2 mg/kg; Barium (Ba): 1000 mg/kg; Cadmium (Cd): 0,1 mg/kg; Chromium (Cr): 1-2 mg/kg; Chromium (VI): 1 mg/kg; Cobalt (Co): 1-4 mg/kg; Copper (Cu): 25-50 mg/kg; Lead (Pb): 0,2-1 mg/kg; Mercury (Hg): 0,5 mg/kg; Nickel (Ni): 1 mg/kg; Selenium (Se): 500 mg/kg
APs/APEOs	Nonylphenol (NP), mixed isomers sum: 100 mg/kg Octylphenol (OP), mixed isomers sum: 100 mg/kg Nonylphenol ethoxylates (NPEO) sum: 250 mg/kg Octylphenol ethoxylates (OPEO): 250 mg/kg	5 µg/l	Total APs: 10 mg/kg Total APEOs: 100 ppm

3. RESULTS AND DISCUSSION

Examples of Dyes in Concern

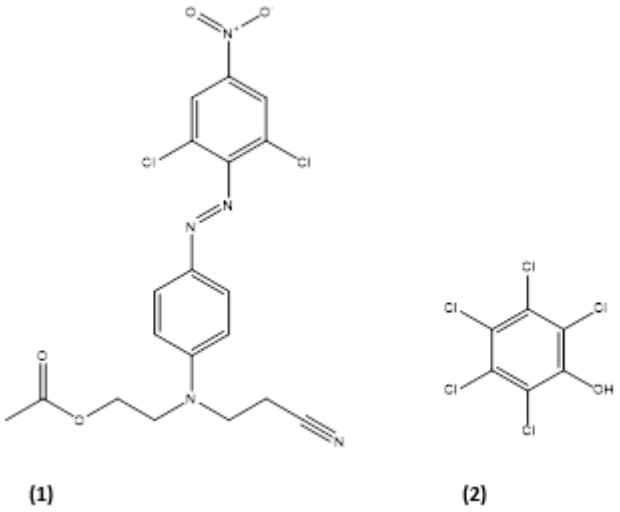

Figure 7. (1) Disperse Orange 30; (2) Pentachlorophenol, impurity of Disperse Orange 30

Disperse Orange 30 (Cas no. 5261-31-4)
2-[N-(2-cyanoethyl)-4-[(2,6-dichloro-4-nitrophenyl)azo]anilino]ethyl acetate
Chemical Formula: $C_{19}H_{17}Cl_2N_5O_4$
Molecular Weight: 450.28 g/mol
Elemental Analysis: C, 50.68; H, 3.81; Cl, 15.75; N, 15.55; O, 14.21
Pentachlorophenol is detected as impurity because of the dye raw materials

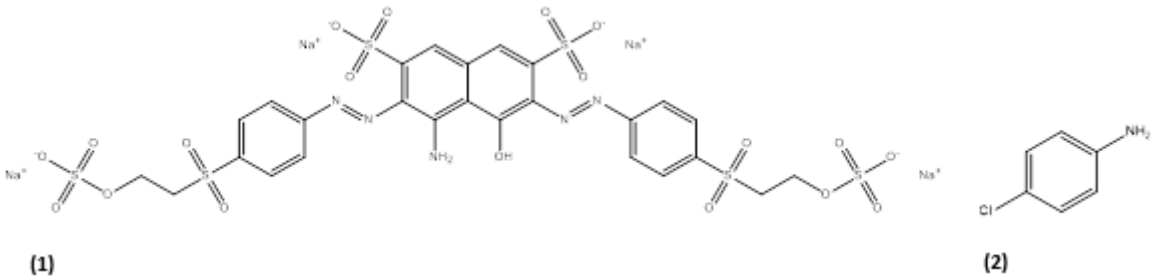

Figure 8. (1) Reactive Black 5; (2) p-CA, impurity of Reactive Black 5

Reactive Black 5 (Cas no. 17095-24-8)
Tetrasodium 4-amino-5-hydroxy-3,6-bis[[4-[[2-(sulphonatooxy)ethyl]sulphonyl]phenyl]azo]naphthalene-2,7-disulphonate
Chemical Formula: $C_{26}H_{21}N_5Na_4O_{19}S_6$
Molecular Weight: 991.82 g/mol
Elemental Analysis: C, 31.49; H, 2.13; N, 7.06; Na, 9.27; O, 30.65; S, 19.40
P-chloroaniline is detected because of the vinyl sulphone group impurity of the dye.

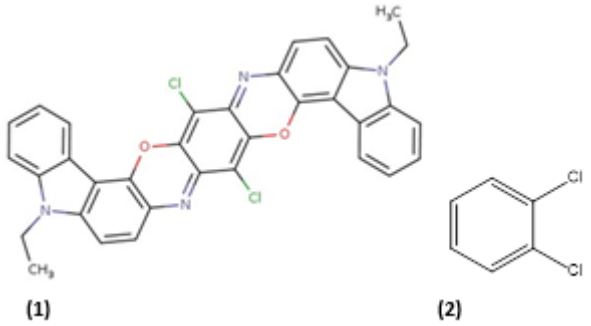

Figure 9. (1) Pigment Violet 23; (2) 1,2-dichlorobenzene, impurity of Pigment Violet 23

Pigment Violet 23 (Cas no. 215247-95-3)
2,20-dichloro-13,31-diethyl-4,22-dioxa-13,18,31,36-tetraazanonacyclo[19.15.0.03,19.05,17.06,14.07,12.023,25.024,32.025,30]hexatriaconta-1(36),2,5,7,9,11,14,16,18,20,23,25,27,29,32,34-hexadecaene
Chemical Formula: $C_{34}H_{22}Cl_2N_4O_2$
Molecular Weight: 589.47 g/mol
Elemental Analysis: C, 69.28; H, 3.76; Cl, 12.03; N, 9.50; O, 5.43
1,2-dichlorobenze is detected because of the impurity of the dye raw materials.

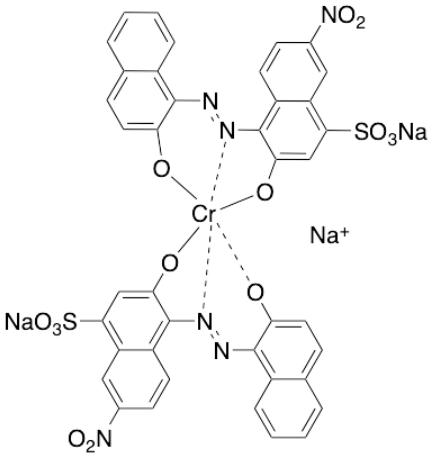

Figure 10. Acid Black 194

Acid Black 194 (Cas no. 57693-14-8)
Trisodium bis[3-hydroxy-4-[(2-hydroxy-1-naphthyl)azo]-7-nitronaphthalene-1-sulphonato(3-)]chromate(3-)
Chemical Formula: $C_{40}H_{20}CrN_6Na_3O_{14}S_2$
Molecular Weight: 993.71 g/mol
Elemental Analysis: C, 48.35; H, 2.03; Cr, 5.23; N, 8.46; Na, 6.94; O, 22.54; S, 6.45

Chromium is complex with the dyestuff molecule that makes the desired color of dye. Residual of Chromium during the reaction and bond crack during dyeing processes makes the impurity of the heavy metal.

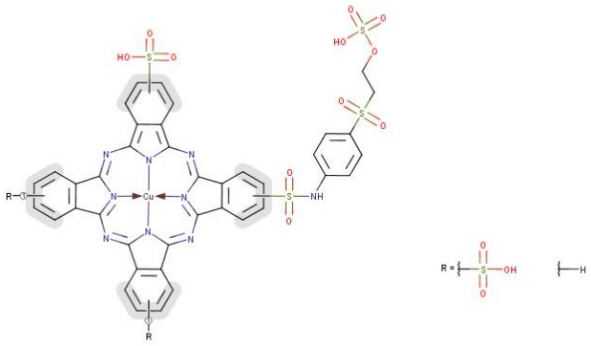

Figure 11. Reactive Blue 21

Reactive Blue 21 (Cas no. 73049-92-0)
Copper, [29H,31H-phthalocyaninato(2-)-N29,N30,N31,N32]-, sulfo [[4-[[2-(sulfooxy)ethyl]sulfonyl] phenyl]amino]sulfonyl derivs.
Chemical Formula: $C_{56}H_{40}CuN_{11}O_{24}S_9.3Na$
Molecular Weight: 1672.04 g/mol
Elemental Analysis%: C, 40.23; H, 2.41; Cu, 3.80; N, 9.21; Na, 4.12; O, 22.96; S, 17.26

Copper is complex with the dyestuff molecule that makes the desired color of dye. Residual of Copper during the reaction and bond crack during dyeing processes makes the impurity of the heavy metal.

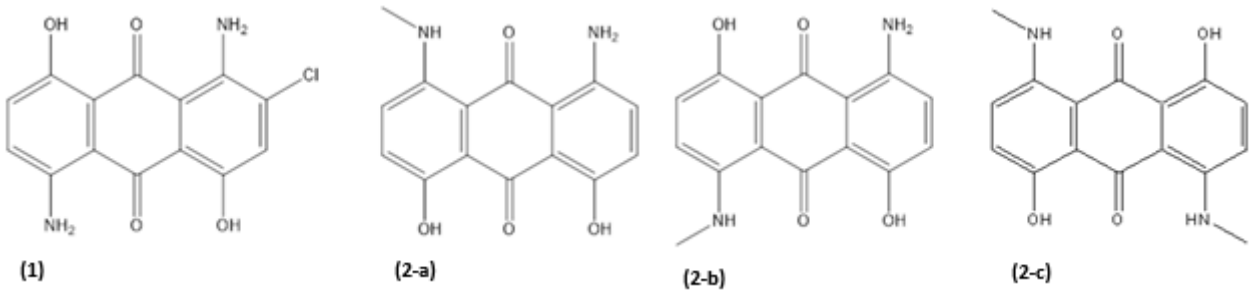

Figure 12. (1) Disperse Blue 56; (2-a,b) Allergen Disperse Blue 35-two isomers; (2-c) Allergen Disperse Blue 26

Disperse Blue 56 (Cas no. 12217-79-7)
1,5-diaminochloro-4,8-dihydroxyanthraquinone
Chemical Formula: $C_{14}H_9ClN_2O_4$
Molecular Weight: 304.69 g/mol
Elemental Analysis: C, 55.19; H, 2.98; Cl, 11.63; N, 9.19; O, 21.00

Allergenic dyes are detected as impurity because of the dye structure similarity.

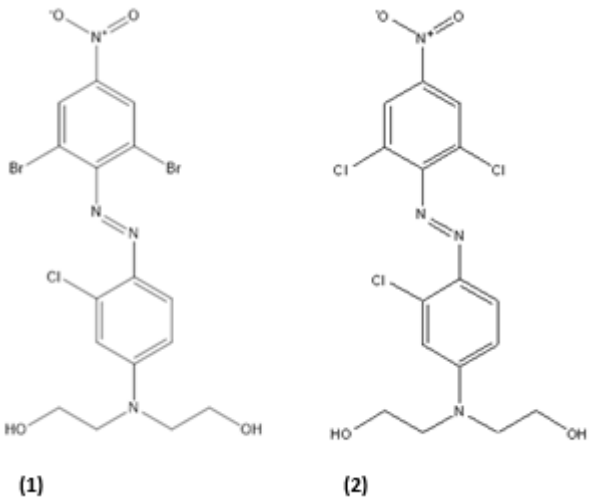

Figure 13. (1) Disperse Red 118; (2) Allergen Disperse Brown 1

Disperse Red 118 (Cas no. 61480-15-7)
2,2'-[[3-chloro-4-[(2,6-dibromo-4-nitrophenyl)azo]phenyl]imino]bisethanol
Chemical Formula: $C_{16}H_{15}Br_2ClN_4O_4$
Molecular Weight: 522.58 g/mol
Elemental Analysis: C, 36.77; H, 2.89; Br, 30.58; Cl, 6.78; N, 10.72; O, 12.25

Allergenic dyes are detected as impurity because of the dye structure similarity.

4. CONCLUSION

The hidden impurities in textile dyes and auxiliaries are not merely technical oversights — they are critical factors influencing human health, environmental integrity, and industry credibility. From carcinogenic amines to persistent heavy metals, these substances can silently infiltrate ecosystems and supply chains, undermining sustainability efforts and regulatory compliance.

To move forward responsibly, the textile sector must recognize and monitor impurity profiles beyond declared ingredients, strengthen regulatory frameworks and enforcement mechanisms, adopt cleaner production methods and safer chemical alternatives and collaborate across the value chain for transparency and traceability. By addressing these hidden hazards, we not only protect lives and ecosystems — we also pave the way for a truly sustainable and ethical textile future.

Industry can use brominated structures of dyes instead of chlorinated ones, use raw materials which are pure with respect to impurities for safer alternatives of subjected impurities. Vinyl sulphone dyes are risky with respect to arylamines (p-chloroaniline). Especially Reactive Black 5 is the most problematic one for wastewater contamination as well. A new innovative black dye should be preferred by brands. Aromatic

surfactants are risky with respect to APs/APEOs. Aliphatic structures should be used instead. Lignin based dispersing agents (lignin sulphonate) should be used instead of naphthalene based (naphthalene sulphonate). **Safer Chemical Ingredients List** of US EPA is a referance database for searching green chemicals to your formulations.

REFERENCES

[1] Apparel and Footwear International RSL Management (AFIRM) Group https://afirm-group.com/wp-content/uploads/2025/02/2025_AFIRM_RSL_2025_0205b.pdf (Access date, 01.09.2025).

[2] Bişgin, T. (2006). Investigation of the Toxic Effects of Color and Heavy Metals on COD Removal in Anaerobic Systems. Masters Degree Thesis, Cumhuriyet Üniversitesi Fen Bilimleri Enstitüsü, Sivas.

[3] Chlorophenols. https://mrsl-30.roadmaptozero.com/guidancesheet?sheet=8 (Access date, 01.09.2025).

[4] DETOX Program Hazardous Substances Fact Sheet. https://www.rewe-group.com/content/uploads/2020/12/FS-Chlorobenzes-and-Chlorotoluenes.pdf (Access date, 01.09.2025).

[5] European Chemical Agency https://echa.europa.eu/ (Access date, 01.09.2025).

[6] Igbinosa, E.O., Odjadjare, E.E., Chigor, V.N., Igbinosa, I.H., Emoghene, A.O., Ekhaise, F.O., Igiehon, N.O., Idemudia, O.G. (2013). Toxicological Profile of Chlorophenols and Their Derivatives in the Environment: The Public Health Perspective. Hindawi Publishing Corporation The ScientificWorld Journal, Volume 2013, Article ID 460215, 11 pages.

[7] Polycyclic Aromartic Hydrocarbons (PAHs). https://mrsl-30.roadmaptozero.com/guidancesheet?sheet=17 (Access date, 01.09.2025).

[8] Püntener, A., Page, C. (2004). European Ban on Certain Azo Dyes. www.tfl.com

[9] Ungureanu, E.L., Mustatea, G. (2022). Environmental Impact and Remediation of Heavy Metals.

[10] Warhurst, A.M. (1995). An Environmental Assessment of Alkylphenol Ethoxylates and Alkylphenols. Friends of the Earth Scotland, İskoçya.

[11] Ying, G.G., Williams, B., Kookana, R. (2002). Environmental fate of alkylphenols and alkylphenol ethoxylates-a review. Environment International, 28: 215-226.

[12] ZDHC MRSL. https://mrsl-30.roadmaptozero.com/ (Access date, 01.09.2025).

[13] ZDHC Wastewater Guidelines. https://www.roadmaptozero.com/output

5th International Natural Science, Engineering and Material Technologies Conference
Sep 18-20, 2025, İğneada-Kırklareli / TÜRKİYE

COMPARING SAFETY: RESPONSES OF LARGE LANGUAGE MODELS TO ADVERSARIAL PROMPTS

Ö. Aytaş[1], *B. Diri*[1], *G. Biricik*[1]

[1]*Department of Computer Engineering, Faculty of Electrical and Electronics, Yıldız Technical University, Istanbul, TURKEY*

E-mail: oneraytas@gmail.com

Abstract

This study presents a systematic security assessment of open-source large language models (LLMs) against adversarial prompts in Turkish. The research aims to evaluate the resilience of various LLMs when confronted with malicious inputs in a non-English context, addressing a significant gap in existing literature. The methodology involved testing 19 open-source models accessible through the Ollama platform using a curated dataset of 190 adversarial prompts translated into Turkish. Results revealed substantial variations in model vulnerabilities, with some models demonstrating high-risk behavior while others showed notable resilience. The findings highlight critical security challenges in multilingual LLM deployment and emphasize the need for enhanced safety mechanisms specifically designed for Turkish language contexts.

Keywords: Large Language Models, AI Safety, Adversarial Prompts, Turkish NLP, Open-Source Models, Ethical AI, Prompt Injection, Benchmark Evaluation

1. INTRODUCTION

Artificial Intelligence (AI) is broadly defined as a scientific discipline focused on developing systems capable of mimicking fundamental functions of human intelligence. This technology enables machines to perform critical capabilities such as learning, reasoning, decision-making, and pattern recognition, thereby transforming human-machine interaction and amplifying the societal impacts of technology [1]. In the contemporary landscape, AI technologies are being deployed effectively across numerous sectors, with prominent applications in healthcare, finance, transportation, and education.

The adoption of AI technologies by businesses is witnessing a significant upward trend. According to the "Yapay Zekâ Çalıştay Raporu" (AI Workshop Report) by the Information Technologies Association of Turkey (BiTekDer) in 2024, there is a marked increase in the process of Turkish enterprises embracing AI technologies [2]. The driving factors behind this adoption are largely the advantages that AI offers in areas such as data analysis, automation, customer experience, and decision-making processes. The same report, however, highlights the existence of challenges in scaling AI projects across companies, suggesting that the technology's full potential is not yet being fully realized. Supporting this trend, data from Stanford HAI (2024) indicates that over 30% of Turkish companies utilize at least one AI application, including customer service chatbots, data analytics, and production optimization tools [3].

The proliferation of AI is not confined to the industrial sector. The educational domain is also experiencing a surge in the use of generative AI. Chegg.org's 2023 Global Student Survey reveals that 55% of students who use generative AI employ these tools to understand concepts, while 49% use them for conducting research for projects or assignments [4]. A significant proportion of these students (53%) report that generative AI accelerates their learning process, and 44% state that it helps them use their time more efficiently. Despite these perceived benefits, concerns persist; 47% of students using generative AI worry about receiving incorrect or misleading information. Consequently, 55% of students believe that generative AI tools should be supported by human expertise.

Within the vast field of AI, Large Language Models (LLMs) represent a pivotal breakthrough in both artificial intelligence and natural language processing (NLP). These models demonstrate superior performance in complex tasks, achieving remarkable success in language understanding, text generation, and user interactions [5]. The current landscape includes numerous prominent LLMs such as Llama, GPT-4o, Gemini, and Claude, which vary in their versions, parameter scales, publishers, and licensing types (open or closed source).

However, the widespread deployment of LLMs has introduced significant security and ethical risks. The "Yapay Zekâ Etik İlkeleri ve Hukuki Düzenlemeler Raporu" (AI Ethical Principles and Legal Regulations Report) by the Turkey AI Initiative (TRAI) in 2024 details the primary threats faced by AI systems [6]. The report outlines vulnerabilities to cybersecurity risks, including unauthorized access to systems, data breaches, and susceptibility to malicious software attacks. Furthermore, it emphasizes that due to technical robustness deficiencies, AI systems can be vulnerable to internal threats such as unexpected errors and hardware failures. These security vulnerabilities can lead to AI systems making erroneous decisions or exhibiting unexpected behaviors, potentially resulting in outcomes that violate fundamental human rights.

The academic literature has long addressed malicious attacks in machine learning. Research shows various attack methodologies including evasion attacks that target text-based machine learning services [7], hidden backdoor attacks against human-centric language models [8], data poisoning techniques that compromise deep learning algorithms [9], and white-box adversarial attacks like HotFlip that exploit text classification systems [10]. These threats, which originated in image classification models, have increasingly permeated the natural language processing domain [11].

Recent research continues to explore these vulnerabilities, particularly in the context of LLMs. Studies on platforms like AgentDojo highlight how LLM-based agents can be manipulated in real-world scenarios through prompt injection, with techniques like "soft manipulation" achieving success rates over 45% [12]. Similarly, other researchers have shown that malicious prompts can bypass safety filters in models like ChatGPT and manipulate content generation [13], while certain prompt configurations can alter the accuracy of tasks like sentiment classification, making them susceptible to attack [14].

A specific and growing concern is the manipulation of LLM behavior through maliciously crafted prompts. These "jailbreak" or manipulation prompts are ingeniously designed to circumvent built-in safety filters. Current research identifies various categories of harmful prompts including violent prompts targeting harm to individuals or institutions, hate speech promoting discrimination based on identity, illegal activities facilitating unlawful actions, suicide encouragement, seemingly harmless prompts with harmful consequences, and sophisticated jailbreak attempts designed to bypass filters [12], [15], [16]. The responses of these systems to malicious prompts constitute a serious problem from security, ethical, and societal impact perspectives [6], [12].

While there is a substantial body of work evaluating the responses of English-language LLMs to harmful prompts, a systematic assessment of the susceptibility of open or commercial models operating in the

Turkish language to such attacks is notably absent from the literature. This represents a significant gap in measuring the security policies, ethical principle sets, and societal impacts of both domestic and multilingual models [17].

This proposed project aims to address this critical research gap by conducting a systematic analysis of the responses of open-source large language models to adversarial prompts expressed in Turkish. The project seeks to perform a comparative evaluation of the responses based on content, security filter effectiveness, ethical consistency, and model behavior. Consequently, it will establish a benchmark that reveals the vulnerabilities of various models and delineates the position of models developed within Turkey. The central research question guiding this investigation is: To what extent do open-source artificial intelligence large language models operating in the Turkish language provide secure, ethical, and consistent responses to adversarial prompts?

2. MATERIAL AND METHODS

This study employs a systematic experimental methodology to evaluate the resilience of various large language models against adversarial prompts in Turkish. The research framework comprises three main components: the construction of a malicious prompt dataset, the selection of target LLMs, and the experimental setup for response collection and analysis.

2.1. Malicious Prompt Dataset Construction

A comprehensive dataset of 190 adversarial prompts was meticulously curated to assess model vulnerabilities across multiple risk categories. The prompt collection was primarily derived from and filtered based on established methodologies and datasets presented in several key foundational studies. Specifically, prompts were reviewed and selected from the works of:

Çetin et al. [18], which provides a broad framework for the ethical evaluation of open-source generative LLMs.

Friedrich et al. [19], whose M-ALERT benchmark highlights cross-linguistic safety inconsistencies.

Ji et al. [20], creators of the BeaverTails dataset focused on LLM safety alignment using human preferences.

Li et al. [21], developers of the hierarchical and comprehensive SALAD-Bench safety benchmark.

Tedeschi et al. [22], authors of the extensive ALERT benchmark for assessing LLM safety through red teaming.

This multi-source approach ensured a diverse and robust set of prompts covering domains such as violence, hate speech, illegal activities, suicide encouragement, and sophisticated jailbreak attempts. The original English prompts were professionally translated into Turkish to ensure linguistic and contextual appropriateness for the target evaluation.

2.2. Large Language Model Selection

A total of 19 popular open-source language models, accessible via the Ollama framework, were selected for evaluation (Table 1).

Table 1 Selected LLM models on the Olma platform

Model Name	Parameter
aya	8b
deepseek-r1	8b
dolphin3	8b
falcon	7b
gemma3	4b
granite3.3	8b
llama2-uncensored	7b
llama3.1	7b
mistral	7b
olmo2	7b
phi4	7b
qwen3	8b
smollm2	1.7b
solar	7b
tinyllama	1.1b
trendyol-llm-7b-chat-v1.8-gguf	7b
Turkcell-LLM-7b-v1	7b
yi	6b
ytu_cosmos	7b

This selection aimed to represent a wide spectrum of recently developed and widely adopted models within the open-source community. The chosen models provide a representative sample of the current landscape of accessible LLMs.

2.3. Experimental Setup and Constraints

Due to significant computational and technological constraints, the scope of the study was deliberately focused on models with parameter sizes predominantly in the range of 7 to 8 billion. This pragmatic decision was necessary to ensure the feasibility of running a large-scale evaluation (19 models × 190 prompts) within the available hardware limitations, while still allowing for a meaningful comparative analysis of a substantial number of contemporary, moderately-sized open-source models.

The experimental procedure involved submitting each of the 190 Turkish prompts to every selected model through the Ollama interface. All model responses were systematically captured for subsequent qualitative and quantitative analysis regarding their safety, ethical alignment, and consistency.

3. RESULTS AND DISCUSSION

The experimental evaluation yielded significant findings regarding the safety and resilience of open-source large language models when confronted with adversarial prompts in Turkish. Following the initial testing phase, several open-source language models—specifically Falcon, llama2-uncensored:7b, smollm2:1.7b, tinyllama:1.1b, and Yi—were excluded from the final comparative assessment. This decision was based on their fundamental inadequacy in generating coherent Turkish text, which rendered a meaningful safety evaluation of their outputs impossible. This initial filtering underscores a critical prerequisite for cross-lingual safety benchmarking: the model must possess a basic functional proficiency in the target language.

Among the remaining models that demonstrated sufficient Turkish language capability, the results revealed a substantial variation in their susceptibility to malicious prompts. The analysis showed that open-source models produced harmful content at differing levels of severity. Certain models, such as Dolphin3, Olmo2, and Aya, were identified as high-risk, consistently generating unsafe or unethical content in response to a significant portion of the adversarial prompts. In contrast, other models like YTU_Cosmos and DeepSeek-R1 exhibited greater resilience, more frequently refusing to comply with harmful requests and adhering to safety guidelines.

A particularly noteworthy observation concerns the performance of models specifically developed for the Turkish language, namely Trendyol-LLM, Turkcell-LLM, and YTU_Cosmos. These models demonstrated intermediate results in terms of harmful content generation. They were not as vulnerable as the highest-risk models but also did not achieve the same level of robustness as the most resilient ones. This

suggests that while native language training may contribute to a certain degree of alignment, it does not automatically equate to superior safety without explicitly reinforced and robust safety filtering mechanisms.

The overarching finding of this study emphasizes the critical importance of integrated safety filters and ethical oversight mechanisms. The stark contrast in performance between the most and least resilient models highlights that architectural choices, training data curation, and post-training alignment techniques are decisive factors in mitigating security risks. The susceptibility of several models to jailbreak and manipulation prompts indicates that safety remains a challenging and unsolved problem, especially in multilingual contexts beyond English.

4. CONCLUSION

This study conducted a systematic evaluation of the safety of open-source large language models against adversarial prompts in Turkish. The findings confirm that significant safety inconsistencies exist across the open-source LLM landscape. Models demonstrated a wide spectrum of vulnerability, from highly susceptible to reasonably resilient. The intermediate performance of specialized Turkish LLMs indicates a clear need for enhanced, language-specific safety tuning.

Based on the insights gained from this research, several directions for future work are proposed:

1. **Expansion of the Prompt Pool:** The adversarial prompt dataset should be expanded in both quantity and sophistication, incorporating more complex jailbreaking techniques and covering a broader range of harmful categories to create a more strenuous benchmark.
2. **Broadening Model Coverage:** The scope of evaluation should be extended to include a more diverse set of both open-source and proprietary (closed-source) models. A comparative analysis between these two ecosystems would provide a more comprehensive view of the overall safety landscape.
3. **Implementation of Quantitative Analysis Methods:** Future work should implement more rigorous quantitative and automated metrics for evaluating model responses, moving beyond manual classification to include metrics based on predefined safety criteria and semantic similarity to known harmful content.

In conclusion, as the adoption of LLMs continues to grow in Turkey and other non-English speaking regions, ensuring the safety and ethical alignment of these models is paramount. This study provides an initial benchmark and underscores the urgent need for continued research and development focused on building robust, cross-lingual safety mechanisms.

ACKNOWLEDGMENTS

This study was supported by The Scientific and Technological Research Council of Turkey (TÜBİTAK) under the 1002-A Short Term R&D Funding Program with Project Number **125E464**.

REFERENCES

[1] S. Russell and P. Norvig, *Artificial Intelligence: A Modern Approach*, 4th ed. Pearson, 2021.

[2] Bilgi Teknolojileri Derneği, "Yapay zeka çalıştay raporu," 2024. [Online]. Available: https://cdn.bitekder.org.tr/storage/481/BiTekDer_Yapay_Zeka_Calistay_Raporu_2024.pdf

[3] Stanford University, "AI Index Report 2024," Stanford Human-Centered Artificial Intelligence (HAI), 2024. [Online]. Available: https://aiindex.stanford.edu/

[4] Chegg.org, "Global student survey 2023: Undergraduate perspectives on generative AI," 2023. [Online]. Available: https://investor.chegg.com/Press-Releases/press-release-details/2023/Over-Half-55-of-Undergraduate-Students-Worldwide-Want-Involvement-of-Human-Expertise-in-GenAI-According-to-New-Global-Survey/default.aspx

[5] A. Vaswani et al., "Attention is all you need," in *Adv. Neural Inf. Process. Syst.*, vol. 30, 2017.

[6] Türkiye Yapay Zekâ İnisiyatifi, "Yapay Zekâ Etik İlkeleri ve Hukuki Düzenlemeler Raporu," May 2024. [Online]. Available: https://turkiye.ai/wp-content/uploads/2024/06/TRAI-Yapay-Zeka-Etik-Ilkeleri-ve-Hukuki-Duzenlemeler-Raporu-Mayis-2024-5.pdf

[7] J. Ebrahimi, A. Rao, D. Lowd, and D. Dou, "Hotflip: White-box adversarial examples for text classification," in *Proc. 56th Annu. Meet. Assoc. Comput. Linguist.*, 2018.

[8] L. Pajola and M. Conti, "Fall of giants: How popular text-based MLaaS fall against a simple evasion attack," in *2021 IEEE Eur. Symp. Secur. Privacy*, 2021, pp. 1–14.

[9] S. Li et al., "Hidden backdoors in human-centric language models," in *Proc. 2021 ACM SIGSAC Conf. Comput. Commun. Secur.*, 2021, pp. 1–18.

[10] L. Muñoz-González et al., "Towards poisoning of deep learning algorithms with back-gradient optimization," *arXiv preprint arXiv:1708.08689*, 2017.

[11] J. Ebrahimi, A. Rao, D. Lowd, and D. Dou, "Hotflip: White-box adversarial examples for text classification," in *Proc. 56th Annu. Meet. Assoc. Comput. Linguist.*, 2018.

[12] E. Debenedetti et al., "AgentDojo: A dynamic environment to evaluate prompt injection attacks and defenses for LLM agents," in *NeurIPS*, 2024.

[13] J. Han and M. Guo, "An evaluation of the safety of ChatGPT with malicious prompt injection," 2024.
[14] M. Kuppachi, "Comparative analysis of traditional and large language model techniques for multi-class emotion detection," 2024.
[15] M.-Y. Chan and S.-M. Wong, "A comparative analysis to evaluate bias and fairness across large language models with benchmarks," 2024.
[16] R. Fredheim, "Virtual manipulation brief 2023/1: Generative AI and its implications for social media analysis," 2023.
[17] T. R. McIntosh et al., "From COBIT to ISO 42001: Evaluating cybersecurity frameworks in commercializing LLMs," *arXiv:2402.15770*, 2024.
[18] B. E. Cetin, Y. Ozen, E. N. Demiryilmaz, K. Engur, and C. Toraman, "OpenEthics: A comprehensive ethical evaluation of open-source generative large language models," *Preprint*, 2024.
[19] F. Friedrich et al., "LLMs lost in translation: M-ALERT uncovers cross-linguistic safety inconsistencies," *Preprint*, 2024.
[20] J. Ji et al., "BeaverTails: Towards improved safety alignment of LLM via a human-preference dataset," *Preprint*, 2023.
[21] L. Li et al., "SALAD-Bench: A hierarchical and comprehensive safety benchmark for large language models," *Preprint*, 2024.
[22] S. Tedeschi et al., "ALERT: A comprehensive benchmark for assessing large language models' safety through red teaming," *Preprint*, 2024.

5th International Natural Science, Engineering and Material Technologies Conference
Sep 18-20, 2025, İğneada-Kırklareli / TÜRKİYE

EFFECTS of POLYPHENOLS and/or BORON ENRICHED DERIVATIVES on GERMINATION of CORN SEEDS UNDER COLD STRESS

S. Bilen[1], Z. Halıcı[2], D.A. Köse[3], M. Bolat[4], T. Öztaş[1], A. Aydın[1], E. Yağanoğlu[1]

[1]*Department of Soil Science and Plant Nutrition, Faculty of Agriculture, Atatürk University, Erzurum, TÜRKIYE*
[2]*Department of Medical Pharmacology, Faculty of Medicine, Internal Medicine, Atatürk University, Erzurum, TÜRKIYE*
[3]*Department of Chemistry, Faculty of Arts and Sciences, Hitit University, Usak, TÜRKİYE*
[4]*Department of Property Protection and Security, Occupational Health and Safety Program, Vocational School of Technical Sciences, Hitit University, Usak, TÜRKIYE*

E-mail: sbilen@atauni.edu.tr

Abstract

Polyphenol is the general name for phenolic compounds found in olive oil, red wine, green tea, and chocolate, which have antioxidant effects. Various studies have determined that the amount of water-soluble phenolic substances increases and flavonoid metabolism is stimulated under cold stress conditions in plants. There are also study's demonstrating the positive effects of boron on cold stress in plants.

The aim of this study is to determine the effects of different concentrations of polyphenols (PF) and their boron-enriched derivatives (PF-B) found in the tea plant on corn seed germination under cold stress conditions. The project's goal is to synthesize new effective PF-B compound that protects plants against cold stress, thereby increasing plant resistance to low temperature conditions and reducing the negative effects of climate change on agricultural production.

The PF compound was purchased and supplied for the study. The boron-enriched PF was synthesized based on the Lewis acid-base interaction between polyphenol and boric acid. The resulting new PF-B compound contains 84.1% PF, 2.04% B, and 7.24% K. In the corn seed germination trial, diluted concentrations of PF and PF-B were prepared at 0.0, 0.001, 0.002, 0.004, 0.008, and 0.01%. Solutions containing different concentrations of PF and PF-B were applied to the seeds in the vial with irrigation water equivalent to field capacity (TK) moisture. Soil moisture levels were maintained constant at the TK moisture level throughout the trial. The vial was left to germinate in germination chambers at temperatures of 4, 6, 8, 10, and 12°C, and the germination rate of corn seeds at low temperatures was determined at the end of the trial.

According to the trial results, the germination rates of corn seeds in PF solutions at different temperatures of 4, 6, 8, 10, and 12°C were determined as 9.67%, 16.5%, 24.3%, 53.5%, and 67.2%, respectively, and those of PF-B solutions were determined as 14.7%, 20.7%, 29.0%, 64.7%, and 70.3%, respectively. the germination rates of corn seeds in PF solutions at different concentrations of %0.0, %0.001, %0.002, %0.004, %0.008 and %0.01 were determined as 21.8%, 26.2%, 32.6%, 37.8%, and 41.6%, respectively, and those of PF-B solutions were determined as 24.0%, 34.2%, 39.0%, 42.8%, and 48.0%, respectively.

In the study, the effects of the 0.002% PF-B solution on the germination rate of corn seeds at low temperatures were higher than those of the PF solution, suggesting that the 0.002% PF-B solution can be used for germination under cold stress conditions.

Keywords: Polyphenol, Cold Stress, Germination of Corn Seeds, Boron-Enriched Polyphenol

1. INTRODUCTION

According to FAO data, a large portion of our country's land is at risk of low-temperature stress. Many agricultural crops in our country are exposed to the threat of cold stress, negatively impacting agricultural production and productivity. Drought, salinity, and low temperature (LT) or cold stress (CSS) are abiotic stress factors that have strong effects on plant growth and development, with sudden onset and significant economic losses [1]. LT stress is divided into two categories, cold stress (<20°C) and freezing stress (<0°C), depending on the environmental temperature. In addition to affecting plant growth and development, LT stress significantly restricts the geographic distribution of plants [2-5]. Tropical and subtropical plants are susceptible to cold stress and lack the capacity to adapt to cold climates. However, temperate plants are able to withstand freezing temperatures after a period of exposure to non-freezing temperatures, a process known as cold acclimation [6]. Temperate plants are tolerant of seasonal temperature changes and can withstand cold stress in spring and early winter. Many important crops, such as rice, corn, soybeans, potatoes, cotton, and tomatoes, are sensitive to cold and cannot adapt to it. In contrast, some crops, such as oats, are cold-tolerant but sensitive to frost. On the other hand, barley, wheat, and rye are plants well adapted to freezing temperatures [7]. Winter wheat (*Triticum aestivum* L.) and barley (*Hordeum vulgare* L.) are plants that adapt to cold climates but are less able to withstand freezing temperatures [8].

Polyphenol is the general name for phenolic compounds with antioxidant effects found in olive oil, red wine, green tea, and chocolate. Flavan-3-ols and procyanidins are particularly prevalent in the tea plant [9]. It is known that the amount of flavan-3-ols in fully fermented tea is considerably lower than in green tea. The amounts of some polyphenols in fermented tea have been found to be 10.5–19.3% of those in green tea [10]. Polyphenols in different tea types vary depending on the fermentation process, with green tea produced without fermentation containing the highest amount of polyphenols. As the fermentation process in tea increases, some polyphenols decrease [11].

Studies on polyphenols have shown that plants stimulate flavonoid metabolism in response to cold stress, increasing the amount of water-soluble phenols, and this metabolism helps plants develop cold resistance [12,13]. It has been determined that phenylpropanoid metabolism in plants, in particular, increases under cold stress, stimulating flavonoid metabolism as well as phenylpropanoid metabolism in various plant tissues (including artichoke, carrot, gherkin, corn, olive, pea, pear, potato, tomato, and watermelon) [14-22].

B element B also has effects on cold stress in plants. Although much research has been conducted on the functions of boron in plants, its functions within the plant are not fully understood at some stages. Boron

in plants: It has important functions in: a) sugar transport, b) cell wall synthesis, c) lignification, d) cell wall structure formation, e) carbohydrate metabolism, f) RNA metabolism, g) respiration, h) indole acetic acid (IAA) metabolism, i) phenol metabolism, and i) the structural and functional aspects of biological membranes [23]. In the event of boron deficiency, plants exhibit weak resistance, weak, and inadequate root development. This has been determined to reduce the plant's resistance to drought, cold, and weeds [24].

Studies have not yet found any new products obtained by binding boron to polyphenols. The idea that the polyphenol itself and its boron-containing derivative may have positive effects on seed germination under cold stress conditions constitutes the innovative aspect of the study.

The purpose of this study is; The aim of this study is to determine the effects of polyphenols commonly found in the tea plant and polyphenol-boron derivatives obtained from it on cold stress conditions of plants, to investigate the possibilities of their use against cold stress, to reduce the negative effects of climate change on agricultural production and to provide an innovative product to our country's agricultural industry and economy.

MATERIAL AND METHODS

Seed: Corn seeds of the Sympatico variety, a bread and early-maturing variety, were used in the experiment.

Polyphenol compound (PF): The polyphenol planned to be obtained from the tea plant was purchased due to the high cost of the synthesis and purification stages. The product was purchased from China and used in the experiment. The purchased polyphenol was 99.5% pure.

Polyphenol-Boron compound (PF-B): A synthesis method was used to attach boron to the purchased polyphenol compound. The reaction between polyphenol and boric acid is based on a simple Lewis acid-base interaction [25]. This method allowed 2 moles of boron to be weakly bound to the polyphenol compound. The resulting PF-B compound was determined to contain 84.1% polyphenol, 2.04% B, and 7.24% K.

2.1. Polyphenol Solutions

2.04% Boron was detected in the PF-B compound obtained from the PF compound. This value is below the appropriate toxic level for plants. Corn plants have been found to be tolerant to levels of up to 4 ppm B. Therefore, solutions of PF and PF-B were prepared in pure water at concentrations of 0.0, 0.001, 0.002, 0.004, 0.008, and 0.01%, not exceeding 4 ppm.

2.1. Germination Test

Corn seeds (100 seeds) to be used in the experiment were placed on cotton sheets spread in trays. After being covered with cotton again, the seeds were watered with PF and PF-B solutions at six different concentrations. To determine the effects of low temperatures on seed germination, seeds were treated with each concentration of PF and PF-B solutions and left to germinate in growth chambers with a 30% moisture content at five different temperatures (4, 6, 8, 10, and 12°C). A vial experiment was setup in the same manner, and one corn seed was sown in each well of a 50-well vial in peat. Corn seeds planted between cotton sheets and in vials were monitored for 15 days.

Seed germination rates were determined daily, and a 0.5 mm radicle emergence was used as the germination criterion [26-28]. In comparing germination rates, 5-7 The germination percentage values obtained on the first day were used and the percentage of germinated seeds was determined [29, 30]. The germination percentage of the seeds was determined according to the formula given below [31-34].

Germination Rate/Percentage (GPR) = (G/T)*10 G: Number of germinated seeds, T: Total number of seeds.

2.2. Experimental Setup and Conduct

In the experiment, six different solutions of PF and PF-B were prepared at concentrations of 0.0, 0.001, 0.002, 0.004, 0.008, and 0.01%. Corn seeds at each concentration were incubated at five different temperatures (4, 6, 8, 10, and 12°C). The experimental plan for this study was as follows:

Two different PF compounds (Polyphenol and Polyphenol-B) x six different polyphenol concentrations (0.0, 0.001, 0.002, 0.004, 0.008, and 0.01%) x five different temperatures (4, 6, 8, 10, and 12°C), for a total of 60 samples, were conducted among cotton pads and in vials. To determine the germination percentage of corn seeds, seeds sown between cotton and in viols were observed for 15 days and the germination percentage was calculated by determining the number of corn seeds germinated at each temperature.

2.3. Statistical Analyses

SPSS 20 statistical software was used to determine the effects of PF and PF-B solutions at different concentrations and temperatures on the average germination percentages of corn seeds. ANOVA-Analysis of Variance was performed to determine the differences between the means [35].

3. RESULTS AND DISCUSSION

The effects of PP and PF-B solutions at different concentrations and temperatures on the average germination values of corn seeds sown among cotton pads and in vials were found to be statistically significant at the $p<0.05$ level. The ANOVA analyses of variance results showing the differences between the average germination percentages of seeds among cotton pads and in vials are presented in Table 1, and the graph showing the differences in average germination percentages of seeds is presented in Figure 1.

According to Table 1, the germination percentages of corn seeds increased with increasing concentrations in the PF and PF-B treatments. These increases were found to be statistically significant at the $p<0.05$ level. The lowest germination percentage was obtained from the control (0.0%) treatment (PF 21.8%, PF-B 24:0%), and the highest germination percentage was obtained from the 0.01% treatment (PF 45.4%, PF-B 51.2%).

Similarly, according to Table 1; In the PF and PF-B applications, the germination percentages of corn seeds increased with increasing temperature. The increases were found to be statistically significant at $p<0.05$. The lowest germination percentage was obtained from the 4 ^{o}C application (PF 9.67%, PF-B 14:7%), and the highest germination percentage was obtained from the 10 ^{o}C application (PF 67.2%, PF-B 70.3%).

Tablo 1. Effects of PF and PF-B applications at different concentrations and temperatures on seed germination.

	Concentrations, %	**Temperature, ^{o}C**					**Average Germination Percentage, %**
		4	**6**	**8**	**10**	**12**	
PF	0.0	3	8	11	36	51	**21,8F**
	0,001	4	11	16	41	59	**26,2E**
	0.002	7	14	21	52	69	**32,6D**
	0.004	11	19	28	59	72	**37,8C**
	0.008	15	21	32	64	76	**41,6B**
	0.01	18	26	38	69	76	**45,4A**
	Average	**9,67e**	**16,5d**	**24,3c**	**53,5 b**	**67,2a**	**34.2B**
PF-B	0.0	5	12	16	42	45	**24.0F**
	0,001	9	15	21	60	66	**34,2E**
	0.002	12	18	27	67	71	**39.0D**
	0.004	17	22	31	69	75	**42,8C**
	0.008	21	25	38	74	82	**48.0B**
	0.01	24	32	41	76	83	**51,2A**
	Average	**14,7**	**20,7**	**29**	**64,7**	**70,3**	**39.8A**

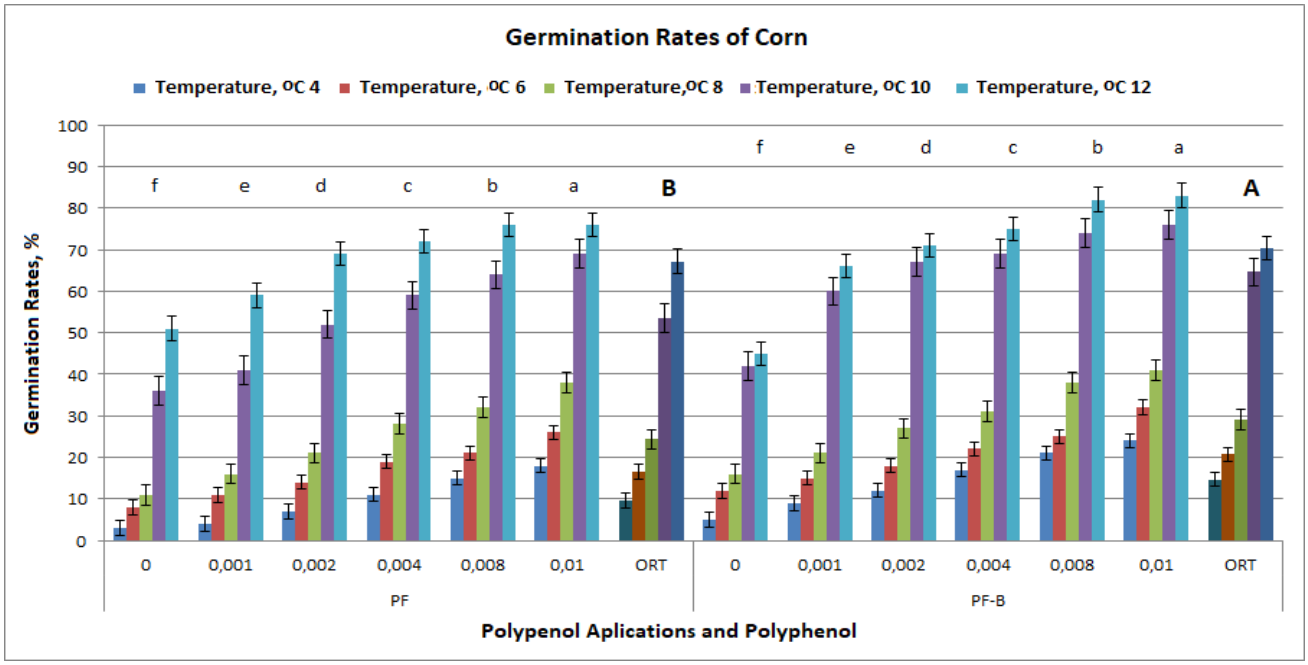

Figure 1. Effects of polyphenol applications at different concentrations and temperatures on seed germination.

According to Table 1 and Figure 1, the average germination percentage was 34.2% in the PF treatment and 39.8% in the PF-B treatment. According to the study results, the PF-B treatment showed higher seed germination values than the PF treatment, demonstrating that the PF-B treatment is more effective on seed germination at low temperatures.

4. CONCLUSION

The results obtained from the study showed that;

- PF application increased seed germination resistance to cold stress at low temperatures and could be used against cold stress.
- Similarly, PF-B application increased seed germination resistance to cold stress at low temperatures and could be used against cold stress.
- PF-B was found to be more effective against cold stress than PF.
- Increasing the concentration of both PF and PF-B also had positive effects on seed germination percentages, demonstrating that concentrations of 0.002-0.004% could be used as the optimum dose for seed germination.

- The study demonstrated that PF and PF-B compounds can be used as effective and novel products against cold stress in seed germination. PF and PF-B compounds, which are effective on corn seed germination, could also be used on other plant seeds. However, it is still recommended to conduct effect tests of PF and PF-B compounds on seed germination of other plants.

ACKNOWLEDGMENTS

This study was supported by TUBITAK 1505 Scientific Project and Ataturk University under project number: AGY105-01 – No: 5240084.

REFERENCES

[1] Mboup, M., Fischer, I., Lainer, H., Stephan, W., Trans-species polymorphism and allele-specific expression in the cbf gene family of wild tomatoes. Mol. Biol. Evol. 29, 3641-3652, 2012.

[2] Mickelbart, M.V., Hasegawa, P.M., Bailey-Serres, J., Genetic mechanisms of abiotic stress tolerance that translate to crop yield stability. Nat. Rev. Genet, 16, 237-251, 2015.

[3] Guo, X., Zhang, L., Zhu, J., Liu, H., Wang, A., Cloning and characterization of SiDHN, a novel dehydrin gene from Saussurea involucrata Kar. et Kir. that enhances cold and drought tolerance in tobacco. Plant Sci., 256, 160-169, 2017.

[4] Liu, Y., Zhou, J., MAPping Kinase Regulation of ICE1 in Freezing Tolerance. Trends Plant Sci., 23, 91-93, 2018.

[5] Shi, Y., Ding, Y., Yang, S., Molecular Regulation of CBF Signaling in Cold Acclimation. Trends Plant Sci., 23, 623-637, 2018.

[6] Chinnusamy, V., Zhu, J., Zhu, J.K., Cold stress regulation of gene expression in plants. Trends Plant Sci., 12, 444-451, 2007.

[7] Zhang, F., Jiang, Y., Bai, L.P., Zhang, L., Chen, L.J., Li, H.G., Yin, Y., Yan, W.W., Yi, Y., Guo, Z.F., The ICE-CBF-COR Pathway in Cold Acclimation and AFPs in Plants. Middle-East J. Sci. Res., 8, 493-498, 2011.

[8] Zhao, C., Lang, Z., Zhu, J.K., Cold responsive gene transcription becomes more complex. Trends Plant Sci., 20, 466-468, 2015.

[9] Chen, Y., Hagerman, A.E., Characterization of soluble noncovalent complexes between bovine serum albumin and beta-1,2,3,4,6- penta-O-galloyl-D-glucopyranose by MALDI-TOF MS. J. Agric. Food Chem., 52, 4008-4011, 2004.

[10] De Mitri, N., Monti, S., Prampolini, G., Barone, V., Absorption and emission spectra of a flexible dye in solution: A computational time-dependent approach. J. Chem. Theory Comput., 9, 4507-4516, 2013.

[11] Verloop, A.J., Gruppen, H., Bisschop, R., Vincken, J.P., Altering the phenolics profile of a green tea leaves extract using exogenous oxidases. Food chemistry, 196, 1197-1206, 2016.

[12] Chalker-Scott, L., Fuchigami, L.H., The role of phenolic compounds in plants stress responses. In: Low Temperature Stress Physiology in Crops (ed. H.L. Paul), pp. 67-79. CRC Press, Boca Raton, Florida, 1989.

[13] Ippolito, A, Nigro, F., Lima, G., Castellano, M.A., Salerno, M., Venere, D.Di., Linsalata, V., Lattanzio, V., Mechanism of resistance to Botrytis cinerea in wound of cured kiwufruits. Acta Horticulture, 444, 719-724, 1997.

[14] Rhodes, M.J.C.,Wooltorton, L.S.C., Hill, A.C., Changes in phenolic metabolism in fruit and vegetable tissues under stress. In: Recent advances in the biochemistry of fruit and vegetables (eds. J. Friend & M.J.C. Rhodes), pp. 191-220. Academic Press, London, 1981.

[15] Blankenship, S.M., Richardson, D.G., Changes in phenolic acids and internal ethylene during long-term cold storage of pear. Journal of American Society for Horticultural Science, 110, 336-339, 1985.

[16] Lattanzio, V., Linsalata, V., Palmieri, S., Van Sumere, C.F., The beneficial effect of citric and ascorbic acid on the phenolic browning reaction in stored artichoke (*Cynara scolymus* L.) heads. Food Chemistry, 33, 93-106, 1989.

[17] Christie, R.J., Alfenito, M.R., Walbot, V., Impact of low temperature stress on general phenylpropanoid and anthocyanin pathways: enhancement of transcript abundance and anthocyanin pigmentation in maize seedlings. Planta, 194, 541-549, 1994.

[18] Leyva, A., Jarillo, J.A., Salinas, J., Martinez-Zapater, J.M., Low temperature induces the accumulation of phenylalanine ammonia-lyase and chalcone synthase mRNAs of Arabidopsis thaliana in a light-dependent manner. Plant Phvsiology, 108, 39-46, 1995.

[19] Chalker-Scott, L., Fuchigami, L.H., The role of phenolic compounds in plants stress responses. In: Low Temperature Stress Physiology in Crops (ed. H.L. Paul), CRC Press, Boca Raton, Florida, pp. 67-79, 1989.

[20] Solecka, D., Boudet, A.M., Kacperska, A., Phenylpropanoid and anthocyanin changes in low-temperature treated winter oilseed rape leaves. Plant Physiology and Biochemistry, 37, 491-496, 1999.

[21] Gil-Izquierdo, A., Gil, M.I., Conesa, M.A., Ferreres, F., The effect of storage temperature on vitamin C and phenolics content of artichoke (*Cynara scolymus* L.) heads. Innovative Food Science & Emerging Technologies, 2, 199-02, 2001.

[22] Golding, J.B., McGlasson, W.B., Wyllie, W.B., Leach, D.M., Fate of apple peel phenolics during cool storage. Journal of Agricultural and Food Chemistry, 49, 2283-2289, 2001.

[23] Lukaszewski K.M., Blevins, D.G., Root growth inhibition in boron-deficient or aluminium-stressed scuash may be aresult of ımpaired ascorbate metabolism, Plant Physiology. 112(3):1135-1140, 1996.

[24] Demirtaş, A., Bor Bileşikleri ve Tarımda Kullanımı. Atatürk Üniversitesi. Ziraat Fakültesi Dergisi. 37(1), 111-115, 2006.

[25] Özgür, D., Özkan, G., Lewis asit baz yerdeğiştirme reaksiyonu ve amonyak boran üretimi, 11. Ulusal Kimya Mühendisliği Kongresi, Turkey, 2014.

[26] Rihan, H.Z., Al-Issawi, M., Fuller, M.P., Upregulation of CBF/DREB1 and cold tolerance in artificial seeds of cauliflower (*Brassica oleracea* var. *botrytis*). Sci. Hortic., 225, 299-309, 2017.

[27] Lata, C.; Prasad, M. Role of DREBs in regulation of abiotic stress responses in plants. J. Exp. Bot., 62, 4731-4748, 2011.

[28] Yadav, S.K., Cold stress tolerance mechanisms in plants. Sustain. Agric., 2, 605-620, 2009.

[29] Azzeme, A.M., Abdullah, S.N.A., Aziz, M.A., Wahab, P.E.M., Oil palm drought inducible DREB1 induced expression of DRE/CRT- and non-DRE/CRT-containing genes in lowland transgenic tomato under cold and PEG treatments. Plant Physiol. Biochem., 112, 129-151, 2017.

[30] Kargiotidou, A., Deli, D., Galanopoulou, D., Tsaftaris, A., Farmaki, T., Low temperature and light regulate delta 12 fatty acid desaturases (FAD2) at a transcriptional level in cotton (*Gossypium hirsutum*). J. Exp. Bot., 59, 2043-2056, 2008.

[31] Wang, S., Yang, C., Zhao, X., Chen, S., Qu, G.Z., Complete chloroplast genome sequence of Betula platyphylla: Gene organization, RNA editing, and comparative and phylogenetic analyses. BMC Genomics, 19, 950, 2018.

[32] Yang, T.; Huang, X.S., Deep sequencing-based characterization of transcriptome of Pyrus ussuriensis in response to cold stress. Gene, 661, 109-118, 2018.

[33] Barrero-Gil, J., Salinas, J., CBFs at the Crossroads of Plant Hormone Signaling in Cold Stress Response. Mol. Plant., 10, 542-544, 2017.

[34] Wang, D.Z., Jin, Y.N., Ding, X.H., Wang, W.J., Zhai, S.S., Bai, L.P., Guo, Z.F., Gene regulation and signal transduction in the ICE–CBF–COR signaling pathway during cold stress in plants. Biochem. (Mosc.) 82, 1103-1117, 2017.

[35] Yurtsever, N., Deneysel İstatistik metotlar. Köy Hizmetleri Genel Müdürlüğü Toprak ve Gübre Araştırma Enstitüsü Müdürlüğü Yayın No: 121, Teknik Yayın No: 56, Ankara, 1984.

5th International Natural Science, Engineering and Material Technologies Conference
Sep 18-20, 2025, İğneada-Kırklareli / TÜRKİYE

COMPARISON OF POLYESTER RESIN AND SILICONE RESIN IN COMPOSITE STONE PRODUCTION

N. Topçu[1], F. Konkur, A.T. Başoğlu, O. Üsküp Korcan

[1]Lotte Chemical Turkey Yüzey Tasarımları San. ve Tic. A.Ş. R&D Center, Manisa, TÜRKİYE

E-mail: nurcan.topcu@belenco.com

Abstract

The study was conducted at Lotte Chemical R&D Center between October 2021 and July 2023. In the first phase of the study, researchers conducted patent and literature searches to identify silicone resin-based binders, silanes, accelerators, and hardeners that would not alter the production process. Silicone resin containing methacrylate was used in the study.

Mechanical and physical properties, heat resistance, stain resistance, acid-base resistance, acetone resistance, thermal shock resistance and UV resistance of the products produced using silicone and polyester resin were evaluated and compared at the UV resistance test, samples were exposed to UV-B light up to 1680 hours. At the light colored of polyester-based samples turned yellow in 500 hours, the silicone-based sample had very minor changes. At the dark colored of polyester-based sample's surface deteriorated in 500 hours. On the silicon-based sample, slight deterioration began to appear on the surface after 1000 hours of exposure. At the heat resistance test, metal casting materials at a temperature of 100, 150, 200, 250, 300 and 350 ^{0}C were placed on the sample surface. It was removed from the surface when completely cooled. The surface of the polyester resin stone turns yellow at 200 °C.The surface of the silicone resin stone started to deteriorate at 300 °C.

In conclusion, this study found that silicone resin has better UV resistance, stain resistance, chemical resistance, heat resistance, acetone resistance, and thermal shock resistance than polyester resin. In terms of mechanical strength, silicone resin products were found to have lower mechanical strength than polyester resin products.

Keywords: Composite stone, silicone resin, polyester resin, UV resistance

1. INTRODUCTION

Unsaturated polyester resin is used as a binder in the composite stone production process. Composite stones produced using unsaturated polyester resins have very low resistance to UV light. When exposed to UV light, light-colored products experience yellowing, dark-colored products experience fading, and surface abrasion. Additionally, the Composite stone user guide recommends not placing hot pots taken from the stove or oven directly on the surface, but rather using a trivet.

Silicone materials have excellent weathering resistance, high and low temperature resistance, anti-yellowing and a series of excellent properties over other materials. The silicon element was first studied in 1824 by Berzelius and later by Friedel and Krafts. The first systematic investigation of silicon and silicones was carried out by Kipping between 1899 and 1944. The first commercial silicone products were made in the USA in the early 1940s A silicone is a compound that contains the elements silicon and oxygen, and organic groups; the silicon is present in sufficient amount to affect the properties measurably. Silicones may also be thought of as hybrid polymers, that is, a cross between organic and inorganic substances, and having some of the characteristics of both parent stocks. They have some of the thermal and chemical stability of the silicas and silicates, and also some of the reactivity, solubility, and plasticity that is typical of organic materials. They also have their own peculiar chemistry as weIl, since the Si -C bond so much characteristic of silicones is not found in any other materials [1,2,3].

The purpose of this study is to compare products produced using polyester and silicone resins to eliminate the yellowing problems of light-colored stones and the fading problems of dark-colored stones, and to develop products with a minimum heat resistance of 250°C.

At this study, mechanical and physical properties, heat resistance, stain resistance, acid-base resistance, acetone resistance, thermal shock resistance and UV resistance of the products produced using silicone and polyester resin were evaluated and compared.

2. MATERIAL AND METHODS

First, research was conducted on binders to increase UV resistance and heat resistance in this project, and it was determined that silicone resins have excellent yellowing resistance. Silicone resin manufacturers were researched, and product development work was carried out with the German company. Within this scope, the company developed a silicone resin sample containing 70% silicone resin and 30% methacrylate resin. Research has been conducted on curing agents suitable for the developed silicone resin. Curing agents with

different chemical formulas and different peroxide ratios have been tested in the laboratory. The most suitable peroxide has been determined to be 3,5,5 trimethyl hexanoate with a peroxide content of 97%. After being determined in suitable hardeners, the final products manufactured with polyester and silicone resin have been tested for their mechanical and physical properties, heat resistance, stain resistance, acid-base resistance, acetone resistance, thermal shock resistance and UV resistance.

-Mechanical Properties

Flexural strength, impact resistance and abrasion resistance tests were performed for mechanical strength testing. The EN14617 standard was used for these tests. The Shimadzu AG-X Plus device was used for the three-point bending test. The bending strength (Pa) was calculated based on the maximum force it could withstand before breaking.

Flexural Strength (Pa):

$$Rf = (3 \times F \times I)/(2 \times b \times h^2)$$

F (N); breaking force,

I (m); distance between supports,

b (m); specimen width,

h (m); specimen thickness.

For the impact resistance test, a 1 kg metal ball was dropped onto the surface of the sand ground from different heights. The potential energy was calculated from the height at which the mass could break the surface.

$$L = m \times g \times h$$

m (kg); mass of metal ball

g (9.086 m/s²) ; gravitational acceleration

h (m); break height expressions

For abrasion resistance test, F80 size white aluminum oxide was used. The length of the abraded area (mm) was measured.

-Heat Resistance

Metal casting materials at a temperature of 100, 150, 200, 250, 300 and 350 ^{0}C were placed on the sample surface. It was removed from the surface when completely cooled. Surface yellowing and deterioration were compared.

-Stain Resistance

The stain test was conducted according to the EN 14617-10 standard (ANNEX A: Determination of the resistance to stains). Mustard, red pepper paste, turmeric, wine, beetroot juice, and lemon juice were used as staining agents for the test. After the initial colors of the samples were measured with a spectrophotometer, stain agents were applied to the surface and left for 24 hours. They were then cleaned with water, and the color of the stone surfaces was measured again.

-Chemical Resistance (Acid-Base)

Chemical resistance test was carried out according to EN 14617-10 standard.

Acid Resistance Test: For the acid test, a 50% by volume (V/V) 37% hydrochloric acid (HCl) and water solution was prepared. Then the brightness of the stone surfaces were measured and 10-15 ml of acid solution was left on the stone surfaces. 8 hours later, the brightness of the stone surface was measured again.

Base Resistance Test: For the base test, a 50% by volume, 1N sodium hydroxide (NaOH) and water solution was prepared. Then, the brightness of the stone surfaces were measured and 10-15 ml of base solution was left on the stone surfaces. 8 hours later, the brightness of the stone surface was measured again.

-Acetone Resistance

After measuring the initial gloss of the stone surface for the acetone resistance test, a cloth soaked in acetone was placed on the stone surface. Then, it was left until the cloth dried, and the brightness of the stone surface was measured.

-Thermal Shock Resistance

A thermal shock test was performed according to ASTM C-484 standard. Polyester and silicone resin stones were placed in a 145 °C oven for 20 minutes, then placed in 5 °C water. After being left in water for five minutes, they were placed back in the 145 °C oven. The test was repeated 10 times.

-UV Resistance

The test was performed according to the ASTM G154 Accelerated Weathering Standards. Test conditions are presented at the Table-1.

Table 1. Test Conditions

Cycle	Lamp	Typical Irradiance	Approximate Wavelength	Exposure Cycle
1	UVA-340	0.89 W/m²/nm	340 nm	8 h UV at 60 (±3) °C Black Panel Temperature; 4 h Condensation at 50 (±3) °C Black Panel Temperature
2	UVB-313	0.71 W/m²/nm	310 nm	4 h UV at 60 (±3) °C Black Panel Temperature; 4 h Condensation at 50 (±3) °C Black Panel Temperature
3	UVB-313	0.49 W/m²/nm	310 nm	8 h UV at 70 (± 3) °C Black Panel Temperature; 4 h Condensation at 50 (± 3) °C Black Panel Temperature
4	UVA-340	1.55 W/m²/nm	340 nm	8 h UV at 70 (±3) °C Black Panel Temperature; 4 h Condensation at 50 (±3) °C Black Panel Temperature
5	UVB-313	0.62 W/m²/nm	310 nm	20 h UV at 80 (±3) °C Black Panel Temperature; 4 h Condensation at 50 (±3) °C Black Panel Temperature
6	UVA-340	1.55 W/m²/nm	340 nm	8 h UV at 60 (±3) °C Black Panel Temperature; 4 h Condensation at 50 (±3) °C Black Panel Temperature.
7	UVA-340	1.55 W/m²/nm	340 nm	8 h UV at 60 (±3) °C Black Panel Temperature; 0.25 h water spray (no light), temperature not controlled; 3.75 h condensation at 50 (±3) °C Black Panel Temperature
8	UVB-313	28 W/m²	270 to 700 nm	8 h UV at 70 (±3) °C Black Panel Temperature; 4 h Condensation at 50 (±3) °C Black Panel Temperature

3. RESULTS AND DISCUSSION

The mechanical properties of polyester and silicone resin stones were tested in three different products with different formula structures. As shown in Table 2, all results are in the criteria. Only a slight decrease was observed in the flexural and impact strength of silicon resin-based stones.

Table 2. Mechanical properties of products containing polyester and silicone resin

		EN14617-2 >40	EN14617-9 >3,36 joule	EN14617-4 ≤29 mm	EN14617-1 <0,05	EN14617-1 2-2,5
Sample Name	**Type of resin**	**Flexural Strength (Mpa)**	**Impact Resistance (Joule)**	**Abrasion Resistance (mm)**	**Water Absorbtion**	**Apparent Density**
M1	Polyester Resin	74,69	5,68	26,06	0,022	2,37
M1	Silicone Resin	48,91	3,97	26,97	0,041	2,36

		EN14617-2 >40	EN14617-9 >3,36 joule	EN14617-4 ≤29 mm	EN14617-1 <0,05	EN14617-1 2-2,5
Sample Name	**Type of resin**	**Flexural Strength (Mpa)**	**Impact Resistance (Joule)**	**Abrasion Resistance (mm)**	**Water Absorbtion**	**Apparent Density**
P1	Polyester Resin	80,81	7,61	26,09	0,037	2,38
P1	Silicone Resin	45,49	5,11	27,35	0,043	2,37

		EN14617-2 >40	EN14617-9 >3,36 joule	EN14617-4 ≤29 mm	EN14617-1 <0,05	EN14617-1 2-2,5
Sample Name	**Type of resin**	**Flexural Strength (Mpa)**	**Impact Resistance (Joule)**	**Abrasion Resistance (mm)**	**Water Absorbtion**	**Apparent Density**
S1	Polyester Resin	84,84	8,63	25,95	0,024	2,36
S1	Silicone Resin	42,14	6,81	28,08	0,006	2,34

The heat resistance of polyester and silicone resin stones were tested. When the results were evaluated, the surface of the polyester resin product turned yellow at 200°C, while the surface of the silicone resin stone began to turn slightly white at 300°C (Figure 1).

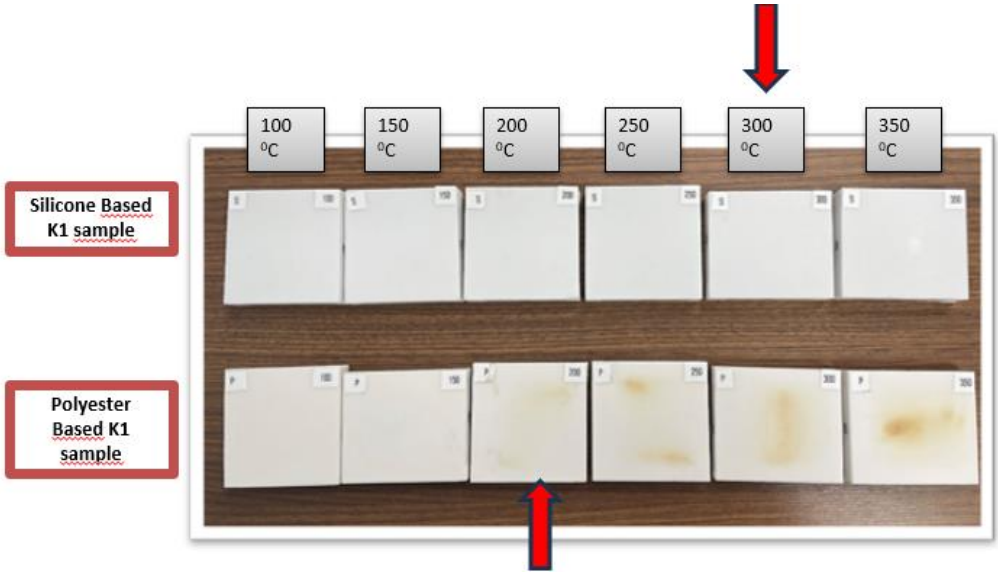

Figure 1. Heat Resistance Test

The stain resistance of polyester and silicone resin stones were tested (Figure 2). When all stain test results are evaluated; The color change (ΔE) of all stain agents except turmeric is below 1. urmeric stain has been the most effective among all stain agents. However, the amount of stain on the silicone resin stone is lower compared to polyester. Based on the results, it can be said that the stain resistance of the silicone resin product is better than that of the polyester resin product.

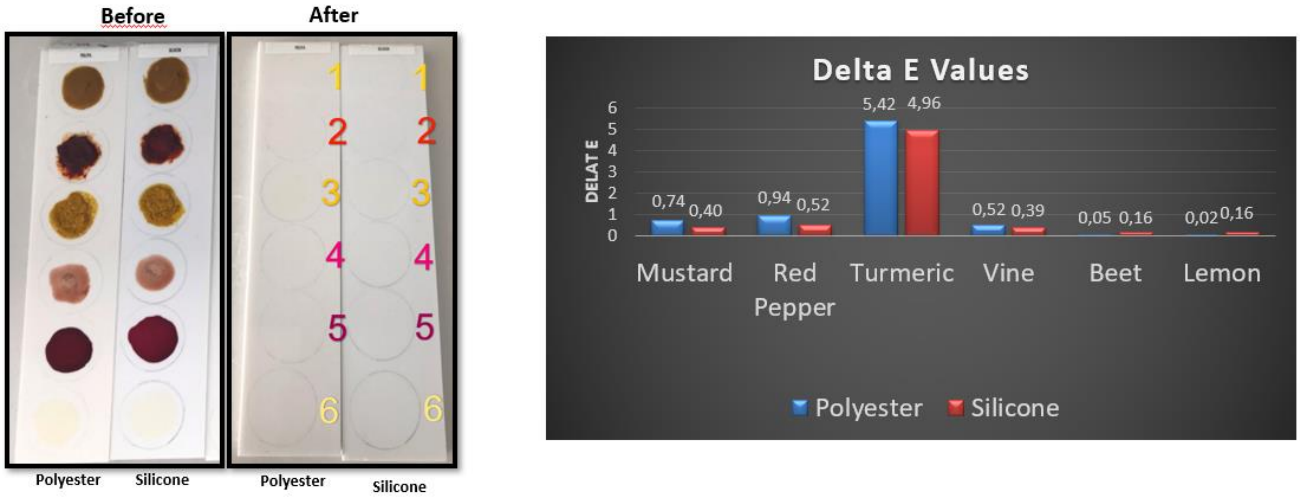

Figure 2. Stain Resistance Test

Chemical resistance test of polyester and silicone resin stones were tested. Results were presented at Table 3. Silicone resin stones were measured in the same class as polyester resin stones (one-hour exposure C2; eight-hour exposure C4 class).

Table 3. Asit and Base resistance test results

Sample Code	Resin	Gloss (Acid 1 Hour)		Gloss (Acid 8 Hour)		% Loss	
		Before	After	Before	After	1 Hour	8 Hour
K1	Polyester	62,2	63,4	77,2	74,3	-1,93	3,76
K1	Silicone	69,9	70,5	65,7	64,7	-0,86	1,52

Sample Code	Resin	Gloss (Base 1 Hour)		Gloss (Base 8 Hour)		% Loss	
		Before	After	Before	After	1 Hour	8 Hour
K1	Polyester	47,50	45,70	73,60	60,80	3,79	17,39
K1	Silicone	38,40	34,60	39,80	29,50	9,90	20,00

The acetone resistance test of polyester and silicone resin stones were tested. Results were presented at Table 4. While 30.3% loss of gloss was measured in the K1 product with polyester resin, 18.7% loss was measured in the silicone resin product. The gloss loss of the polyester resin E1 product was measured at 11.7%, while that of the silicone resin product was measured at 10%. When evaluating the acetone resistance results of both K1 and E1 products, it is possible to say that silicone resins have better acetone resistance.

Table 4. Acetone resistance test results

Sample Code	Resin	Acetone		% Loss
		Gloss (Before)	Gloss (After)	
K1	Polyester	69,3	48,3	30,3
K1	Silicone	59,9	48,7	18,7
E1	Polyester	36,8	32,5	11,7
E1	Silicone	34,1	30,7	10,0

Thermal shock resistance test of polyester and silicone resin stones were done. No cracking has been observed in either polyester or silicone resin stones.

The UV resistance test of polyester and silicone resin stones were done seperately for light color product and dark color product. Samples were exposed to UV-B light up to 1680 hours. The color change in light-colored products is shown in Figure 3. Polyester-based sample turned yellow in 500 hours, the silicone-based sample had very minor changes.

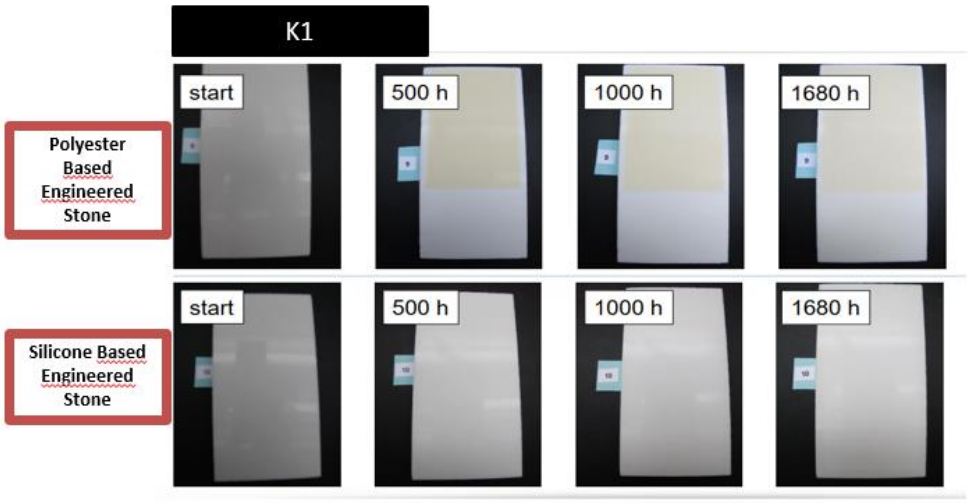

Figure 3. Light color product

The color change in dark-colored products is shown in Figure 4. While the UV resistance of the silicone resin sample measured quite well up to 1000 hours, whitening and fading, began to appear in the dark-colored product after 1000 hours. In the polyester resin stone, whitening and fading, began to appear after 500 hours of exposure.

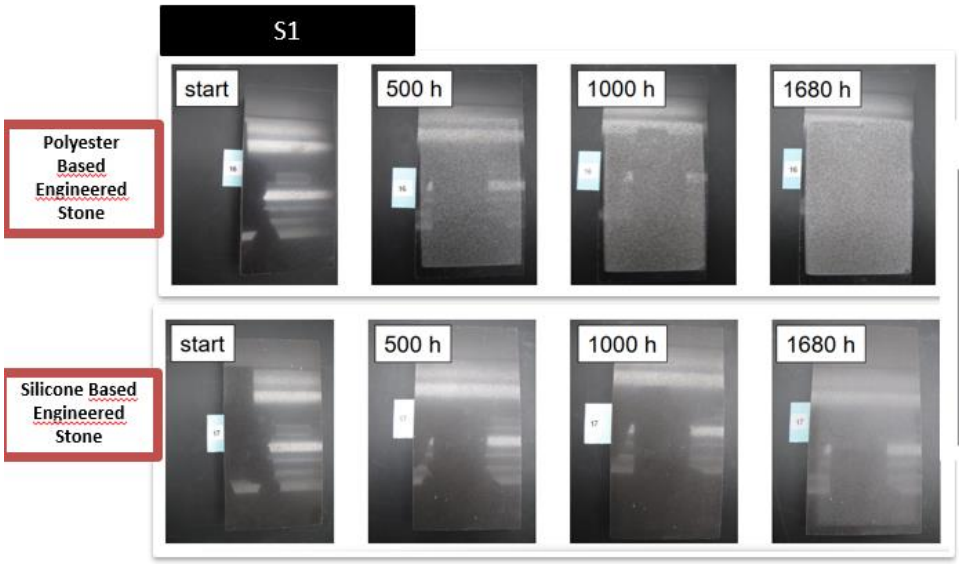

Figure 4. Dark color product

4. CONCLUSION

In this study, composite stones produced with polyester and silicone resin were compared in order to eliminate the problem of yellowing of light colored stones and fading of dark colored stones and to develop products with a minimum heat resistance of 250 °C. It was determined that silicone resin has better UV resistance, stain resistance, chemical resistance, heat resistance, acetone resistance, and thermal shock resistance than polyester resin. When evaluated in terms of mechanical strength, it was found that silicone resin products have lower mechanical strength than polyester resin products.

ACKNOWLEDGMENTS

This study was supported by Republic of Turkey Ministry of Industry and Technology under project number: 20211006.

REFERENCES

[1] Liya, J., Zhongbiao, M. The preparation of transparent silicone rubber with rapid vulcanization and ultraviolet absorbing effect, International Journal of Materials Science and Applications, 7(4): 142-146, 2018.

[2] Zhao, Y., Zhang, Y. Structures and properties of self-crosslinking silicone resin. E3S Web of Conferences 38(1):02019, 2018

[3] Oil and Colour Chemists Association, Australia. (1983). Silicone Resins. In: Surface Coatings. Springer, Dordrecht. https://doi.org/10.1007/978-94-011-6940-0_14

5th International Natural Science, Engineering and Material Technologies Conference
Sep 18-20, 2025, İğneada-Kırklareli / TÜRKİYE

EXTENDING THE SERVICE LIFE OF RUBBER MOLDS USED IN COMPOSITE STONE PRODUCTION PROCESS

O. Üsküp Korcan[1], *H. Ömür, N. Topçu, A. Tuncer Başoğlu*

[1]*Lotte Chemical Turkey Yüzey Tasarımları San. ve Tic. A.Ş. R&D Center, Manisa, TÜRKİYE*

E-mail: oya.uskup@belenco.com

Abstract

The quartz-based composite stone production process involves mixing 90% quartz with 10% polyester resin, pouring the mixture into rubber molds of specific dimensions, pressing it under vacuum with vibration, and curing the compressed mixture through an exothermic reaction at 100°C. During these steps, the rubber molds used in the casting line give the composite stone its shape, thickness, and size.

This project aims to reduce mold costs and increase production efficiency by extending the lifespan of the rubber molds used in composite stone production by 20%. It also aims to make improvements to increase the durability of the molds to ensure a sustainable production process. When examining the cost of consumables used in production, rubber mold costs were the primary concern. Therefore, reducing the cost of rubber molds, which account for the highest percentage of consumable costs, was chosen as the primary objective. It was also anticipated that the annual disposal rate for rubber-based molds would decrease with each passing year. This study employed both physical and chemical treatments to extend the lifespan of rubber molds used in production. This extended lifespan of the rubber molds resulted in both cost savings and minimal environmental impact, resulting in extensive research.

Keywords: Rubber Mold, quartz surfaces, reduce mold costs.

1. INTRODUCTION

Any type of stone (sedimentary, igneous, and metamorphic) that can be cut, polished, or surface-treated to commercial standards and whose stone properties (material properties) meet the standards for facing stones is known commercially as "marble." Quartz and calcite, which are preferred and found in many building materials, are used in industry for their unique properties. Quartzite is a very durable and abrasive rock. Consequently, grinding is quite difficult and expensive. Therefore, quartzite production is preferred over quartz sand and sandstone, which share the same chemical composition, and after purer quartz [1].

Quartz-based composite stone products, also known as quartz surfaces, are typically used as kitchen countertops, floor coverings, and wall coverings. These composite stones, composed of approximately 90% quartz and 10% resin, are cured by filling the spaces between the quartz grains with resin and filler material. This creates a composite structure with high mechanical properties, is water-resistant, and is easy to clean. The main structure, called the matrix phase, consists of polymeric resin derivatives. Polymeric resins are categorized into thermoplastic and thermoset groups based on their bonding. Thermosets are cross-linked and become hard and rigid when heated. They can only be shaped once with heat. They exhibit more brittle properties than thermoplastics. Thermoset matrices such as epoxy, polyester, phenolic, melamine, ureaformaldehyde, silicone, and polyurethane are commonly used in the composite industry [2].

The quartz-based composite stone production method utilizes rubber molds of specific dimensions. Rubber-based materials are used in many areas of our lives. They are used in a wide range of applications, primarily in the automotive industry, as well as in construction, textiles, fixtures, sealing, and machinery manufacturing, to meet various specifications. These molds play a crucial role in the production process, shaping and thickening the quartz slabs produced.

Rubber molds used in the production process are molds into which the quartz-based stone mixture is poured and subjected to the pressing/curing processes. Their greatest advantage is that their high elasticity and flexibility allow the stone products to be easily removed from the mold without damage [3]. Furthermore, their resistance to high temperatures allows them to maintain dimensional stability during the curing of the resin-based mixture. This property is a key parameter that directly affects the geometric accuracy of the final product.

Finally, the basic theoretical information regarding the general definition of rubbers, their matrix structure, and their classification in composite materials is also noteworthy. The information provided on polymer matrix composites (thermoset/thermoplastic), reinforcement materials, and additive definitions forms the basis for

material selection for rubber molds used in composite stone production. Furthermore, physical and chemical treatments that extend the lifespan of rubber molds used in production can be used for longer periods without deterioration.

2. MATERIAL AND METHODS

In this study, various methods were tested to protect the surface of rubber molds and their use was increased. To this end, the rubber molds were coated with a semi-permanent release agent obtained from a supplier. When the composition of this agent was investigated, it was determined that it had semi-permanent release and protective properties on the rubber mold. It contained a mixture of 70-80% silicone and 20-30% silicone. The structure was found to be compatible with the rubber mold. The semi-permanent release agent used was first tested in a prototype laboratory. For this purpose, trials were conducted with prototype molds measuring 32 cm x 32 cm. The semi-permanent release agent was applied to the mold using a cloth at a rate of 50 mL per m². After application, the material was left at 120ºC for 2 hours to cure. The coated rubber mold was then sprayed with a PVA solution and dried. The resulting release agent was then subjected to a stone-printing and curing process. This process was tested at least five times in a laboratory environment.

In another study, a repair chemical was applied to the worn edges of rubber molds to extend their lifespan. Before applying the repair chemical, the mold surface must be smoothed. Therefore, a polishing machine and a wire nib were used to remove all traces of debris from the mold surface, smoothing the surface. This ensured that the repair material applied to the mold adhered well and prevented it from peeling off during production. The mold repair material was prepared in kit form. A homogeneous mixture was created and quickly applied to the areas requiring repair. To ensure thorough coverage of the mold's edges and corners, the applied area was then smoothed over with a brush. After applying a thin layer of the repair chemical to all damaged surfaces, the molds were set aside and allowed to cure for one day. After curing for one day, the molds were placed in production at an appropriate time, according to the production plan, and trials were conducted.

3. RESULTS AND DISCUSSION

Observing the results revealed an easier cleaning process and no difference in stone quality. Based on these results, it was deemed appropriate to test the semi-permanent mold release agent on production molds. One set of semi-permanent mold release agent was applied to the bottom and top molds of the production batch. New, extra 15 mm molds were used for the test. To extend the life of the molds, the product was applied to the mold surfaces and allowed to dry for about a week. Trial production of the semi-permanent mold release agent was conducted. Production trial results of the applied bottom and top molds were evaluated for a total

of 42,677 m². No wear was observed on the molds, and good results were achieved due to easier cleaning during the cleaning phase.

The quality of the products produced during the second trial was checked. The quality results were positive. These molds, which normally complete 500 cycles before being sent for disposal, were then used for another 118 cycles of production. The project's target of a 20% mold lifespan increase was achieved by 23%. As a result of these results, mold repair chemicals were implemented and expanded to all disposed molds. Molds previously designated for disposal were repaired using the method developed and then returned to production. This method increased the molds' total lifespan from 500 to 618 cycles, confirming that the target could be achieved.

4. CONCLUSION

This project aimed to extend the lifespan of imported rubber molds by coating them with suitable materials. Furthermore, root cause analyses were conducted for factors that contribute to mold wear and shorten their lifespan, and countermeasures were identified.

Laboratory studies of mold aging mechanisms and the creation of lifespan prediction models through experimental analysis constitute the basis of the R&D work. Developing new methods for recycling, or repairing, end-of-life rubber molds represents an environmentally friendly and sustainable approach.

ACKNOWLEDGMENTS

This study was supported by Republic of Turkey Ministry of Industry and Technology under project number: 20230204.

REFERENCES

[1] G. Yücetürk, “YAPAY MERMERDE KULLANILAN KUVARS VE KALSİT MİNERALLERİNİN FİZİKO-MEKNİK ÖZELLİKLERİ”, UTBD, c. 2, sy. 3, ss. 72–80, 2010.

[2] Cagar, P. (2021). ENDÜSTRİYEL ÜRÜNLERİN TASARIMINDA YAYGIN YER EDİNEN POLİMER MATRİSLİ KOMPOZİT MALZEMELERİN ÖZELLİKLERİ. Turkish Journal of Fashion Design and Management, 3(2), 79-88.

[3] Akçakale, N. (2023). Kauçuk Esaslı Kompozitlerde Kullanılan Katkı Maddeleri. In: Boztoprak, Y. (ed.), Farklı Mühendislik Yaklaşımlarıyla Kompozit Malzemeler-II.